DISSERTATION

submitted

to the

Combined Faculties of the Natural Sciences and Mathematics

of the

Ruperto-Carola University of Heidelberg, Germany

for the degree of

Doctor of Natural Sciences

Put forward by

Tiancheng Zhong

born in: Sichuan, China

Oral Examination: 2023.07.13

Irradiation Studies for the Mu3e Tile Detector

Referees: Prof. Dr. Hans-Christian Schultz-Coulon

Prof. Dr. Peter Fischer

Abstract

The Mu3e experiment aims to search for the highly suppressed charged Lepton Flavor Violation (cLFV) decay process $\mu^+ \rightarrow e^+e^+e^-$ with a sensitivity of 10^{-16}, which is four orders of magnitude better than the current exclusion limit. The Tile Detector, composed of scintillation tiles and Silicon Photomultipliers (SiPMs), is designed to provide the most accurate timing measurement with a resolution of <100 ps and an efficiency close to 100 %, playing a crucial role in accidental background suppression.

This thesis covers the study of the radiation damage impacts on the Tile Detector, focusing primarily on the most radiation-damage-sensitive component, the SiPM. The radiation environment in the Mu3e experiment has been estimated using a GEANT4 simulation, and a radiation damage test of the Tile Detector Matrices has been conducted at the same beamline as the actual Mu3e experiment, reaching 70 % of the maximum dose. A comprehensive laboratory characterization has been carried out to assess the impact on the SiPMs, particularly the noise of radiated SiPMs. The performance characterization in the beam-test campaign reveals that a timing resolution better than 60 ps and efficiency close to 100 % can be achieved with suitable signal readout electronics. Based on the radiation study results, modifications have been suggested for the current Tile Detector support system and readout electronics to maintain optimal performance in the presence of radiation damage.

Zusammenfassung

Das Mu3e-Experiment zielt darauf ab, den hochgradig unterdrückten geladenen Lepton Flavor Violation (cLFV) Zerfallsprozess $\mu^+ \rightarrow e^+e^+e^-$ mit einer Empfindlichkeit von 10^{-16} zu suchen, die vier Größenordnungen besser ist als die aktuelle Ausschlussgrenze. Der Tile Detector, bestehend aus Szintillationstiles und Silizium-Photomultipliern (SiPMs), ist darauf ausgelegt, die genauesten Zeitmessungen mit einer Auflösung von <100 ps und einer Effizienz nahe 100 % zu liefern, welches eine entscheidende Rolle bei der Unterdrückung zufälliger Hintergründe spielt.

Diese Dissertation befasst sich mit der Untersuchung der Auswirkungen von Strahlenschäden auf den Tile Detector, wobei der Schwerpunkt auf der strahlungsempfindlichsten Komponente, dem SiPM, liegt. Die Strahlungsumgebung im Mu3e-Experiment wurde mithilfe der GEANT4-Simulation abgeschätzt und ein Strahlenschädigungstest der Tile Detector Matrizen wurde unter Verwendung derselben Strahllinie wie im eigentlichen Mu3e-Experiment durchgeführt und erreichte 70 % der maximalen Dosis. Eine umfassende Charakterisierung im Labor wurde durchgeführt, um die Auswirkungen auf SiPMs zu bewerten, insbesondere das Rauschen der bestrahlten SiPMs, das im Frequenzbereich analysiert wurde. Die Leistungscharakterisierung im Strahlentest zeigt, dass eine Zeitauflösung von besser als 60 ps und eine Effizienz nahe 100 % mit geeigneter Signalausleseelektronik erreicht werden kann. Basierend auf den Ergebnissen der Strahlenstudie wurden Änderungen für das derzeitige Tile Detector-Stützsystem und die Signalausleseelektronik vorgeschlagen, um die optimale Leistung trotz Strahlenschäden aufrechtzuerhalten.

Contents

Chapter 1

Introduction

What makes up the universe? is a question that has captivated humanity throughout its long history. Incredibly, over 2000 years ago, ancient Chinese and Greek philosophers independently conceived strikingly similar ideas: the world is made of fundamental elements. In ancient China, the *five elements* (metal (金), wood (木), water (水), fire (火), and earth (土)) were believed to be the essential building blocks of the world, first mentioned in the book "Spring and Autumn Annals" (《左传》) [1]. In parallel, ancient Greece saw the emergence of the four *roots* (fire, air, water, and earth) as established by Empedocles, which were thought to form the entirety of the world's structure [2]. To date, no one has provided a definitive answer to this question. Nevertheless, the most comprehensive response that contemporary particle physicists have put forth is the *Standard Model* (SM), owing to its immense success in describing elementary particles and their interactions scientifically.

Despite its strengths, the SM has limitations in explaining certain phenomena, and evidence to expand it remains limited. Given the recent discovery of *Lepton Flavor Violation* (LFV) in neutral leptons, LFV in charged leptons appears to be a promising candidate for new physics beyond the SM. The *Mu3e* experiment is designed to search for a potential *charged Lepton Flavor Violation* (cLFV) decay, $\mu^+ \to e^+e^+e^-$, with a sensitivity of $O(10^{-16})$. Detecting this decay would constitute a clear indication of new physics, while failing to do so would exclude the branching ratio above 10^{-16}.

The *Mu3e Tile Detector* is a sub-detector in the Mu3e experiment, designed to deliver the most accurate timing information of muon decays with a timing resolution better than 100 ps and an efficiency close to 100 %. To attain this performance, fast plastic scintillator tiles and Silicon Photomultipliers (SiPMs) are utilized as front-end sensors. The technical prototype's beam-test results indicate that the requirements have been met. This thesis focuses on the irradiation study of the Mu3e Tile Detector to verify whether its performance remains within the specified requirements after exposure to radiation.

This thesis is organized into four parts:

- Background (Chapter 2, 3, 4):
  This section provides an overview of particle physics and radiation damage, as well as the current status and radiation challenges of the Mu3e Tile Detector.
- Irradiation damage study and SiPM characterization (Chapter 5, 6):
  This section focuses on the radiation damage beam-test and a comprehensive characterization of irradiated SiPMs.
- Irradiation effects on the Mu3e Tile Detector (Chapter 7, 8):
  This section presents the performance measurement and analysis of the irradiation effects on

the Mu3e Tile Detector, primarily concentrating on timing and efficiency effects. Based on the study results, suggestions for the Mu3e Tile Detector support system and readout electronics are proposed.

- Summary Chapter (Chapter 9):
  This part will summarize the thesis.

Contributions from author

Within a collaborative project, contributions often reach beyond the scope of a doctoral thesis. The author's input encompasses two primary aspects: the radiation study of the Tile Detector, which will be detailed presented in this thesis, and other development contributions that will not be extensively addressed within the thesis.

The author has led the radiation study of the Tile Detector, including topic proposal, experiment design, dose estimation simulation, SiPM response simulation, performance characterizations, and results analysis. The dose estimation was developed based on the general Mu3e simulation software derived from GEANT4 [3], where the author implemented a new SiPM structure and dose calculation algorithm. The SiPM response simulation was based on GosSiP [4], with all parameter measurements conducted by the author.

The Tile Detector technical prototype development is a joint effort among the Mu3e Tile Detector group, in which the author was also involved. The author's contributions include GEANT4 simulation for both overall Mu3e simulation and detailed Tile simulation. Moreover, the author participated in the design and test of the Tile Detector Printed Circuit Boards (PCBs), such as the Tile Module Board and Tile Matrix board. Additionally, the author played a key role in the prototype characterization and results analysis. The author also developed the Quality Control (QC) system for Tile Detector production and contributed to the Mu3e Data Acquisition (DAQ) development, primarily focusing on the front-end software development for the Tile Detector.

Chapter 2

Charged Lepton Flavor Violation

The cLFV is a process in which the *lepton family number* is not conserved in the transition among leptons (e, μ and τ). On the one hand, cLFV is forbidden in the Minimal SM at the tree level and still strongly suppressed to an undetectable level even with taking neutrino mixing into account. On the other hand, many new theories predicte that the branching ratio of the cLFV process could be reached with modern experiments after decades of development. Thus, any observation of the cLFV process would be a clear signal for New Physics beyond the SM.

This chapter will first introduce the great success of the SM in describing and predicting experimental data. Indeed, the limits of the current SM will be discussed as well. And then, a review of cLFV from theory to experimental history will be presented.

2.1 The Standard Model of Particle Physics

The SM is a Quantum Field Theory (QFT) developed from both theoretical ideas and experimental data to describe fundamental particles and their interactions. It was first-time named with the current name by Pais and Treiman in 1975 [5] and became a tremendously successful theory established in the past decades due to its remarkable achievement in the prediction of experimental data [6, 7].

The prediction of the existence of W and Z bosons, gluon, top quark, and bottom quark was confirmed by experimental data [8]. With the discovery of the Higgs boson in 2012 at the Large Hardon Collider (LHC) [9, 10], this theory's last missing puzzle of experimental validation is in place. Mathematically, the SM has a group structure SU(3)×SU(2)×U(1) to describe both electroweak and strong interactions, where the SU(3) group is for the strong interaction and the SU(2)×U(1) group is for the electroweak interaction.

2.1.1 Fundamental particles

The fundamental particles in the SM are cataloged into fermions and bosons based on their weak isospin. Fermions, following the Fermi-Dirac statistics, have half-integer spin, and all the discovered fermions in elementary particles have spin 1/2. In contrast, bosons, obeying the Bose-Einstein statistics, have integer spin. Figure 2.1 shows all the fundamental particles discovered until 2022.

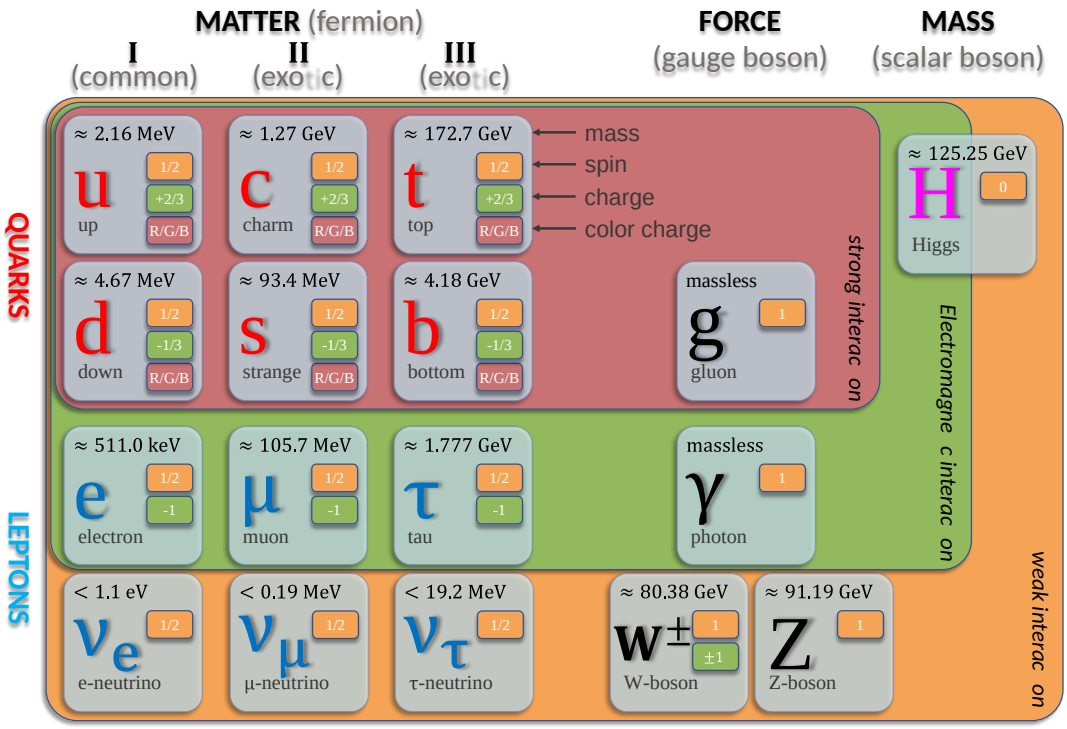

Figure 2.1: Fundamental particles of the Standard Model, where data is from *review of particle physics* published by Particle Data Group in 2022 [7].

Fermions

Fermions in the SM are the basic bricks that build the matter of the Universe. Twelve different fermions are found as elementary particles, and each has its particle and antiparticle. From here on, the word particle stands for the same type of particle and antiparticle if not specifically explained. Different quantum numbers further classify fermions.

All the fermions can be separated into quarks and leptons according to whether they carry the color charge $r/g/b$. Quarks are particles with color charge, enabling them to interact via the strong force. Due to the color confinement phenomenon, quarks combine and form hadrons and can never be found in isolation. In contrast, leptons cannot interact via strong force and can be found freely. Another difference between quarks and leptons is that leptons have integer electric charge values (∓ 1 or 0) while quarks have fractional electric charge values ($\mp 1/3$ or $\pm 2/3$). However, hadrons always have an integer charge or no charge.

All the fermions can also be classified into three generations, sometimes named families, due to their flavor quantum number and mass. Each generation includes two quarks and two leptons. Each fermion in the higher generation is heavier than the corresponding fermion in the lower generation with the same electric charge, color charge and isospin. The only possible exception to this mass hierarchy might happen among neutral leptons for which the masses have not yet been measured accurately enough. Particles in the first generation have the lowest mass, which means that the particles in other generations can decay to the first generation, but the inverse processes need extra energy in order to take place. It explains why all the common matter around us is made of elementary particles from the first generation,

like the proton (uud combination) and electron, and particles from the higher generation can only be observed in extremely high-energy environments, like the LHC [11] or γ-ray bursts [12].

Gauge bosons

The gauge bosons in the SM are the elementary particles employed as force carriers, which reflect the understanding of the interaction between elementary particles — interaction is the exchange of a force-mediating gauge boson. Cataloged by interaction types, three types of gauge bosons are included in the SM corresponding to three of the four fundamental interactions — photon (γ) for electromagnetic (EM) interaction, $W^{\pm}$ and Z boson for the weak interaction, and gluons for the strong interaction.

Photon (γ): Quantum electrodynamics (QED), the theory to describe the EM interaction, is the gauge theory with the symmetry group U(1). Thus, there is only one massless gauge boson — photon (γ). The EM interaction between two electrically charged particles equals the process that one particle emits a virtual photon which is absorbed by the other particle.

Weak bosons ($W^{\pm}$, Z bosons): The three weak bosons correspond to the three generators of the group SU(2) in electroweak theory (EWT), and all are massive due to the Higgs mechanism. Furthermore, the weak bosons are the particles which mediate the weak interaction between particles. $W^{\pm}$ bosons only act with left-handed (LH) particles and right-handed (RH) antiparticles because of the Parity violation in the weak charged-current interaction. Due to their electric charge, the $W^{\pm}$ bosons can also act with other electrically charged particles via virtual photon exchange. In contrast, Z boson involve the weak interaction (neutral-current interaction). All three weak bosons are short-lived, with a lifetime of $O(10^{-25})$ s.

Gluons: In quantum chromodynamics (QCD), the strong interaction between color-charged particles is mediated by eight gluons, corresponding to the eight generators in the gauge group SU(3). Because the color states can be mixed, many sets of independent eight-color states ("color octet") can be used to present the color states of gluons, and here is the commonly used set:

$$\begin{aligned}
&(r\bar{b} + b\bar{r})/\sqrt{2} && -i(r\bar{b} - b\bar{r})/\sqrt{2} \\
&(r\bar{g} + g\bar{r})/\sqrt{2} && -i(r\bar{g} - g\bar{r})/\sqrt{2} \\
&(b\bar{g} + g\bar{b})/\sqrt{2} && -i(b\bar{g} - g\bar{b})/\sqrt{2} \\
&(r\bar{r} - b\bar{b})/\sqrt{2} && (r\bar{r} + b\bar{b} - 2g\bar{g})/\sqrt{6}
\end{aligned}$$

, which are linearly independent. Unlike photons carrying no electrical charge, gluons participate in the strong interaction while mediating it, making the QCD theory significantly harder.

If the color group would be U(3) instead of SU(3), there would be another color singlet $(r\bar{r} + g\bar{g} + b\bar{b})/\sqrt{3}$ besides the octet discussed. And this colorless (or "white") gluon would behave like a "second photon" with no pure charge and would not participate in the strong interaction directly.

Higgs boson

The Higgs boson is a massive elementary scalar boson with spin 0. It is the quantum excitation of the Higgs field, whose existence breaks the electroweak symmetry. The Higgs boson can interact with any particle with non-zero mass, including itself. Its mass was measured in the ATLAS and CMS experiments at the LHC with the value of 125.25 GeV, which completed the fundamental particle spectrum of the SM.

2.1.2 Fundamental interactions in nature

Conventionally, there are four fundamental force interactions in nature: strong interaction, EM interaction, weak interaction, and gravity. In the SM, three fundamental interactions are explained by treating the interaction processes as the exchange processes of force-carrier bosons — γ for EM, gluon for strong interaction, and W and Z bosons for weak interaction.

In quantum mechanics, the transition rate Γ_{fi} of interactions between two fermions $\mathrm{f}_1 + \mathrm{f}_3 \rightarrow \mathrm{f}_2 + \mathrm{f}_4$ (see Feynman diagram in Figure 2.2(a)) is given by Fermi's golden rule:

$$\Gamma_{fi} = 2\pi |T_{fi}|^2 \rho(E_f), \tag{2.1}$$

where i is the initial state $(\mathrm{f}_1 + \mathrm{f}_3)$, f is the final state $(\mathrm{f}_2 + \mathrm{f}_4)$, $\rho(E_f)$ is the phase space distribution of the final state, and T_{fi} is the transition matrix element, given by the time-ordered perturbation theory (second-order):

$$T_{fi} = \frac{M_{fi}}{(16E_1E_2E_3E_4)^{\frac{1}{2}}}, \tag{2.2}$$

where the E_i $(i = 1, 2, 3, 4)$ is the energy of the fermions and the M_{fi} is the Lorentz invariant matrix element:

$$M_{fi} = \frac{g_1 g_2}{q^2 - m_{\mathrm{X}}^2}, \tag{2.3}$$

where g_1 and g_2 are the coupling strengths corresponding to the interaction vertices in Figure 2.2(b) and (c), q^2 is the four-vector scalar product with $q^2 = (p_1 - p_2)^2 = (p_4 - p_3)^2$ and the m_{X} is the mass of the exchanged boson coming from the uncertainty principle:

$$m_{\mathrm{X}} \cdot \Delta t \geqslant \frac{\hbar}{2}, \tag{2.4}$$

where Δt is the corresponding propagation time.

In Equation 2.3, the term $1/(q^2 - m_{\mathrm{X}}^2)$ is referred to as the propagator. The coupling strength g_i is often replaced by the associated dimensionless constant, $\alpha \propto g^2$, for convenience. The dimensionless coupling strengths for strong, EM, and weak interactions are 1, 1/137, and 1/30, respectively.

Interactions between two fermions can be divided into two SM interaction vertices, each of which is the coupling of the gauge boson to the fermions. The SM vertex is the basic unit when analyzing the interaction, and different interaction vertices correspond to the coupling between different fermions and gauge bosons. The fermions couple to a force carrier only if it carries the corresponding charge of the interaction. Figure 2.3 shows some SM vertex examples for fermions interacting with four types of

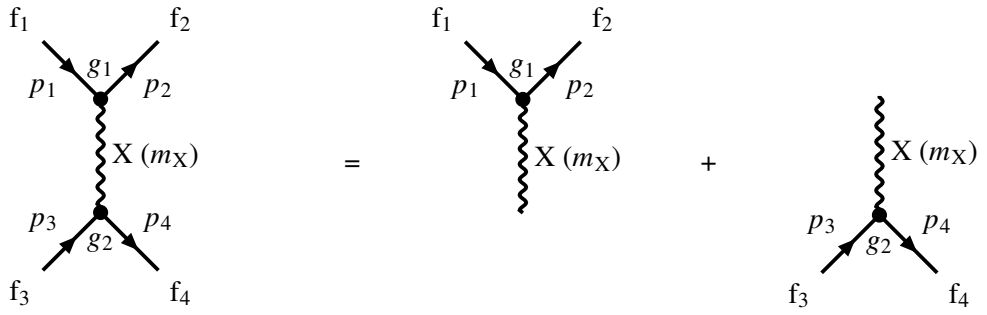

(a) interaction between fermions (b) boson emission (c) boson absorption

Figure 2.2: Interaction between fermions is equivalent to the emission/absorption process of gauge bosons: (a) = (b) + (c).

gauged bosons.

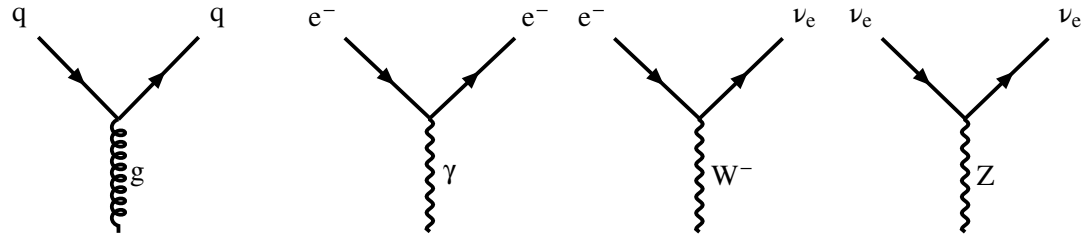

(a) Strong ($\alpha_S \sim 1$) (b) EM ($\alpha = 1/137$) (c) Weak interaction ($\alpha_{W/Z} \sim 1/30$)

Figure 2.3: The vertices for the SM fundamental forces interactions.

Among all the fundamental force interactions in nature, the only unexplained interaction is gravity which is not part of the SM. The hypothesis of graviton exchange for its interaction was proposed, but no evidence has been directly found. Table 2.1 summarizes the feature of the fundamental forces found in nature.

Beyond the fundamental interaction of forces, the Higgs mechanism, conventionally not counted among the fundamental forces, is also included in the SM which explains the mass of particles.

Strong interaction

The strong interaction is the strongest force found in the proton-scale distance ($O(\mathrm{fm})$). In the SM, the strong interaction is treated as the strong-force-carrier gluon interacts with the color-charged particles. The quarks are the only fermions carrying color charge; thus, they are the only fermions that can couple with gluons. Beyond quarks, the gluons can also couple to themselves because they carry the color charge. Figure 2.4 shows the mathematical forms of different strong interactions by Feynman diagrams.

In QCD, the three color states (r, g, b) can be represented by the color wavefunctions:

$$r = \begin{pmatrix} 1 \\ 0 \\ 0 \end{pmatrix}, \; g = \begin{pmatrix} 0 \\ 1 \\ 0 \end{pmatrix}, \; b = \begin{pmatrix} 0 \\ 0 \\ 1 \end{pmatrix}. \tag{2.5}$$

Table 2.1: The four fundamental forces known in nature.

Type	Strong	EM	Weak	Gravity
Current theory	QCD	QED	EWT	General relativity (GR)
Mediators	Gluons (g)	Photons (γ)	$W^{\pm}$/Z bosons	Graviton (hypothesis)
Spin	1	1	1	2
Act on	Electrical charge	Color charge	Weak isospin/charge	–
Relative strength (@10^{-15} m)	1	10^{-3}	10^{-8}	10^{-37}
Long-distance behavior	$\sim r$	$\sim 1/r$	$\frac{1}{r}e^{-r\cdot m_{W,Z}}$	$\frac{1}{r}$
Range	10^{-15}	∞	10^{-18}	∞

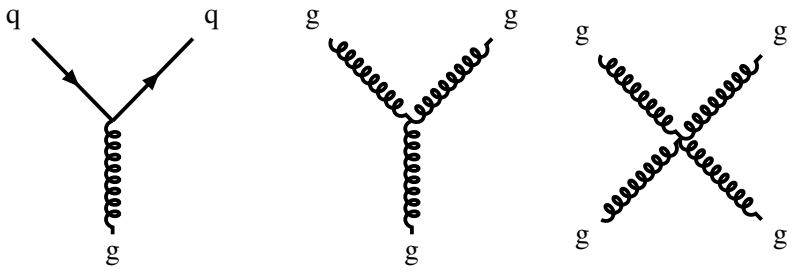

Figure 2.4: Feynman vertices for the SM strong interactions (q stands for quarks here).

However, due to the *color confinement* hypothesis, only colorless ("white") bounded states of quarks, hadrons, can exist as free particles. For example, in the $e^+e^- \rightarrow q\bar{q}$ process, the produced quark/anti-quark cannot travel back-to-back freely; thus, only colorless particles can be measured in the experiments. This process of high-energy quark (and gluons) producing jets is known as hadronization. Motivated by QCD, a model with five steps is commonly used as a qualitative description (Figure 2.5):

- 1). quark/anti-quark production: high-energy quark and anti-quark produced and fly back-to-back;
- 2). kinetic energy to color field energy transformation: the high energy of the color field is restricted in a tube between $q\bar{q}$ pair ($\sim 10^{-15}$ m);
- 3). new $q\bar{q}$ pair production: with further separation, new $q\bar{q}$ pair can be produced when the color field energy is high enough;
- 4). continuation of step 3: more $q\bar{q}$ pairs production;
- 5). end of process: the energy of all the quarks and anti-quarks is too low for new pair production.

This process results in two colorless jets following the original particle directions (quark and anti-quark).

As discussed above, hadrons, like protons and neutrons, are the bound states of quarks due to strong interaction. Moreover, it was found that a hadron is significantly heavier than the sum mass of quarks composing it, which is due to the strong field energy in the hadron. For instance, the sum mass of

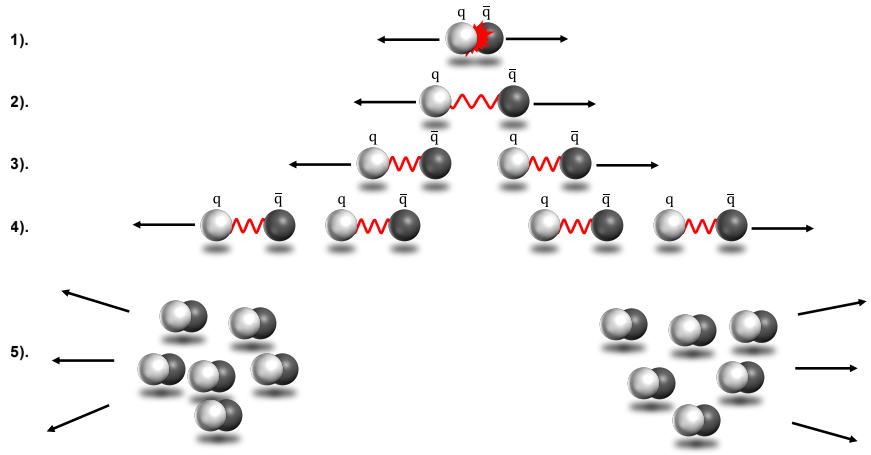

Figure 2.5: Hadronisation process model based on QCD.

individual quarks for a proton is about 8.99 MeV, about 1 % of the proton mass of 938.27 MeV. About 99 % of the proton mass comes from the strong interaction inside the proton.

EM interaction

The EM interaction is the only long-distance force in the SM. Based on the SM, the EM interaction can be treated as the exchange process of the massless EM-force carrier (γ) between electrically-charged particles. Because the EM interaction only acts on the electric charge, the neutrinos are the only exceptions in the fermions, which cannot couple to the EM force. Moreover, the EM force can also interact with the charged $W^{\pm}$ boson. Unlike the gluon carrying color charge, the photon carries no charge; thus, it cannot couple to itself. One of the bounded states of the EM interaction is the atom structure, which is bounded by the EM interaction between one positively-charged nucleus and one or multiple negatively-charged electrons.

Weak interaction

In the SM, the weak interaction is the only fundamental force coupling to all the fermions. Differing from the massless carrier for strong and EM interaction, the force carriers for this interaction are massive $W^{\pm}$ and Z bosons. The weak interaction is naturally divided into weak charged-current and weak neutral-current interactions due to the electric charge of $W^{\pm}$ and Z. Furthermore, the $W^{\pm}$ bosons act on isospin. In contrast, the Z boson acts on the weak charge. Moreover, the $W^{\pm}$ bosons only interact with left-handed fermions and right-handed antifermions, while the Z boson can interact with all fermions and antifermions. The weak interaction is the only interaction that breaks both parity (P) and charge-parity (CP) symmetry.

Similarly to the strong interaction, the weak interaction is also a short-distance force, although the short range of weak interaction comes from the significant mass of mediators. The heavy force mediators with a mass of $O(90\,\text{GeV})$ result in an interaction range of $O(10^{-18}\,\text{m})$ based on Equation 2.4. The weak interaction is the weakest interaction at relatively low-energy scales at fm^{-1} even the intrinsic strength of the weak interaction, with $\alpha_W \sim 1/30$, is stronger than that of the EM interaction. In a relatively

high-energy environment, the weak and EM interaction are united into the electroweak interaction described by the Glashow, Salam and Weinberg (GSW) model developed in the 1960s [13–15].

2.2 Limits of the Standard Model

Currently, the SM is a model with a large number of free parameters, in total 26 parameters if the strong CP phase θ_{CP} counted [16], to describe the observations instead of developing from a higher theoretical principle. Undoubtedly, the SM is one of physics's great triumphs due to its success to predict many experimental results. Despite this, many questions remain unanswered, and many hints imply new physics beyond the SM. A few of the outstanding issues and efforts for solutions will be discussed in this section.

What is dark matter? Based on observation and cosmological models, only 4 % of the Universe is made of ordinary matter, and 23 % of the Universe is Dark Matter (DM) which is believed to play a crucial role in holding the Universe together via gravity [17]. It was named "dark" because it does not interact with the EM field, which makes it hard to be detected. One method to detect DM is measuring the nuclear-recoiling energy to identify the energy deposited by DM via elastic scattering with nuclei: $\chi + A \rightarrow \chi + A$. It is the direct-detection method which is the idea of experiments like CDMS[18], CRESST[19], LZ[20], and XENON[21]. Another method, called the indirect-detection method, detects the SM particles instead of the DM itself. Experiments like IceCube [22] are searching for neutrinos with super high energy, which would be indirect proof for DM.

Does supersymmetry exist? The Minimal Supersymmetric Standard Model (MSSM) [23] is one of the most popular theories to extend the SM, in which each SM particle has a supersymmetric partner "sparticle" with a 1/2 spin difference, as shown in Figure 2.6. However, no sparticle has ever been discovered. At the LHC, searching for sparticles is one of the main focuses for new physics searches [24–26].

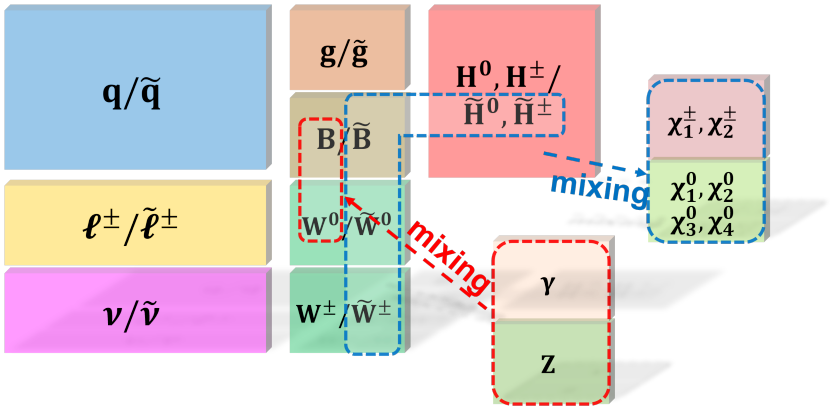

Figure 2.6: Particles and corresponding sparticles in MSSM. (red) The particle B boson and neutral W boson are mixtures of gamma and Z boson. (blue) The 2 charginos ($\chi_1^{\pm}$, $\chi_2^{\pm}$) are the mixtures of charged Winos $W^{\pm}$ and charged Higgsinos $H^{\pm}$. Moreover, the 4 neutralinos χ_i^0 with $i = 1, 2, 3, 4$ are the mixtures of Bino $\tilde{B}$, neutral Wino $\tilde{W}^0$ and neutral Higgsinos $\tilde{H}^0$.

What is the nature of the Higgs boson? Within the SM, the Higgs mechanism assumes a doublet of complex scalar fields because it is the most straightforward choice instead of the unique one. For example, supersymmetry (SUSY) model chooses (at least) two doublets of complex fields to extend the SM and further experiments [27], like measuring the 125 GeV Higgs boson's branch rate, may provide new proofs for new physics. The Higgs-factory accelerator was proposed to produce the Higgs boson at a very high rate, enabling more detailed measurement. A potential candidate for a linear-accelerator [28] is the International Linear Collider (ILC) [29] proposed in Japan. Additionally, the Compact Linear Collider (CLIC) [30] at CERN is another option. While the circular-accelerator Higgs factory is the Future Circular Collider (FCC-ee) [31] at CERN and the Circular Electron Positron Collider (CEPC) in China [32].

What is the origin of flavour and CP violation? There are still many open questions about the flavor sector of the SM. The SM does not explain why there are only three generations of fermions. Furthermore, the observation of neutrino oscillations [33–37] gives a compelling reason to extend the SM. The transition from one type of neutrino to another even violates the lepton flavor of the individual particle type.

So, it is for sure that the current SM is not the end of the story, and there are still many loose ends. This work is on the experiment aiming to search for the cLFV process, which would also be a clear signal for the new physics. More theoretical details about the cLFV will be discussed in the next section.

2.3 Charged Lepton Flavor Violation

In the SM, fermions include six quark flavors and six lepton flavors. The flavor of fermions can only transfer to another flavor by charged-current weak interaction with exchanging a $W^{\pm}$ boson. For leptons, the *lepton number conservation law* is proposed to describe the reaction with lepton participating like $\mu^+ \to e^+ \bar{\nu}_\mu \nu_e$.

2.3.1 Lepton number and conservation laws

The *net lepton number* L is defined as:

$$L = n_\ell - n_{\bar{\ell}}, \tag{2.6}$$

where n_ℓ is the number of leptons and $n_{\bar{\ell}}$ is the number of antileptons. Beyond the lepton number, the *lepton family numbers* (L_e, L_μ, L_τ) are also defined for all three generations of leptons, as listed in Table 2.2. In the SM, it is believed that L is conserved in the Universe, known as the lepton number conservation law. Moreover, the individual lepton family numbers are also conserved, commonly known as lepton flavor conservation. Consequently, the change of both lepton number ΔL and lepton family number (ΔL_e, ΔL_μ and ΔL_τ) in any interaction process is expected to be zero.

Table 2.2: Lepton family number

leptons	L_e	L_μ	L_τ
e^-, ν_e	1	0	0
μ^-, ν_μ	0	1	0
τ^-, ν_τ	0	0	1
e^+, $\bar{\nu}_e$	-1	0	0
μ^+, $\bar{\nu}_\mu$	0	-1	0
τ^+, $\bar{\nu}_\tau$	0	0	-1

2.3.2 Lepton flavor violation

The observation of neutrino oscillations violates the lepton flavor conservation [38–40], which means that the lepton family number is not conserved. The non-observation of the LFV in charged leptons sector might be surprising at first glance. However, it matches the SM calculations.

In the SM, the cLFV process is not allowed at tree level. Even with neutrino oscillations and mixing effects included, it is still strongly suppressed at an extremely low rate due to that (a) the charged leptons are significantly heavier than neutral leptons and (b) the W-boson mass is much bigger than the mass difference between neutrinos. For instance, with current knowledge of the Pontecorv-Maki-Nakagawa-Sakata (PMNS) matrix, the branching ratio of $\mu^+ \rightarrow e^+e^+e^-$ reported in Hernádez-Tomé's work [41] is still far below to be detectable with

$$\mathcal{B}(\mu^+ \rightarrow e^+e^+e^-) \approx 7.4 \times 10^{-55}, \tag{2.7}$$

where the contribution of the dominant penguin diagram and box diagram is considered. Figure 2.7 shows an example of the cLFV process $\mu^+ \rightarrow e^+e^+e^-$, where neutrino mixing is involved in a γ-/Z-penguin process.

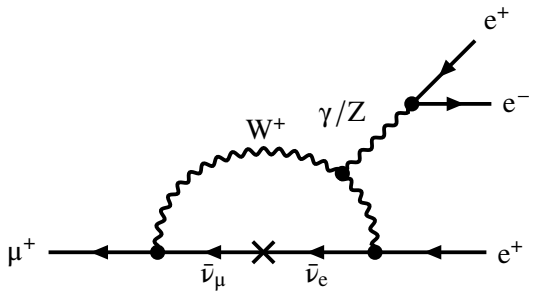

Figure 2.7: Feynman diagram of $\mu^+ \rightarrow e^+e^+e^-$ via neutrino mixing, where the "cross" symbolizes the neutrino oscillation.

However, many potential extensions of the SM, such as the Grand Unified Theory (GUT) model [42–44], SUSY model [45], left-right symmetric models [46], models with an extended Higgs sector [47], predict an experimentally accessible amount of cLFV in a large region of the parameter space. Since the branching ratio of this type of process based on the SM is negligible, any observation of this process

would be clear evidence for New Physics.

A large scale of processes can be used to search for cLFV, such as charged leptons decay($\mu^+ \to e^+\gamma$, $\mu^\pm \to e^\pm e^+ e^-$, $\tau^\pm \to \ell^\pm\gamma$, $\tau \to 3\ell$), rare meson and boson decays ($\pi, J/\psi, B, K, h, Z^0$) , and lepton conversion in the nuclear field ($\mu^- N \to e^- N$, $\mu^- N \to e^+ N'$). Different processes are dominant in different parameter space regions. Table 2.3 summarizes the best limits reached in different processes.

2.3.3 Muon: experimental probe for charged Lepton Flavor Violation searches

The muon is the lightest unstable charged lepton whose properties are listed in Table 2.4, where Feynman diagrams of the listed decay modes are shown in Figure 2.8.

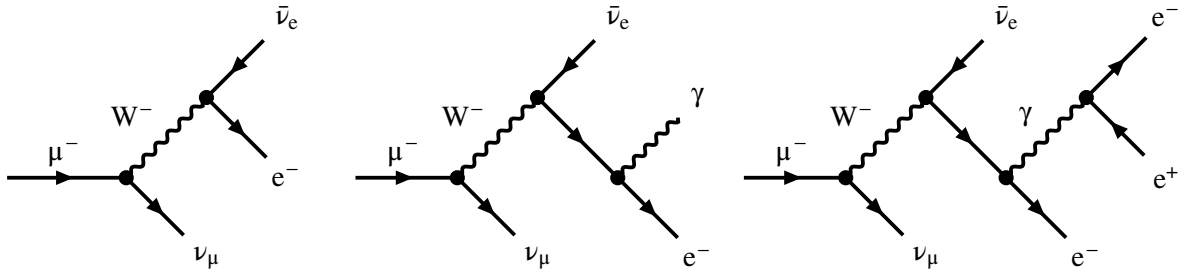

(a) $\mu^- \to e^- \bar{\nu}_e \nu_\mu$ (b) $\mu^- \to e^- \bar{\nu}_e \nu_\mu \gamma$ (c) $\mu^- \to e^- e^- e^+ \bar{\nu}_e \nu_\mu$

Figure 2.8: Most common muon decay modes.

The muon-involved process is a suitable probe for cLFV searching and, so far, has been the most popular one due to the following reasons:

- the high-rate muon beams can be reached at high-energy accelerators or meson factories to obtain enough statistics in a reasonable time;
- the muon has a longer lifetime, $\tau_\mu = 2.2\,\mu$s, compared to all other unstable particles;
- the simple final states of muon-related interactions make it easy to be detected.

The most popular muon-involved cLFV processes are anomalous muon decays, including $\mu^+ \to e^+\gamma$ and $\mu^\pm \to e^\pm e^- e^+$, and muon to electron conversion in a nuclear field $\mu^- N \to e^+ N$.

In the search for muon-decay cLFV processes, only μ^+ is used because of that:

- (a) μ^+ cannot be captured by the nuclei, while μ^- can undergo nuclear capture events and produce protons, neutrons, and photons which bring extra noise as well as extra damage to detectors,
- (b) the muon beam is produced by the decay of pions from proton-target interaction, where more π^+ can be produced, thus, resulting in a higher μ^+ beam.

The sensitivity of the muon-involved cLFV searching improved by 12 orders of magnitude in the past 70 years. Figure 2.9 summarizes all the milestones of the cLFV searches.

The $\mu^+ \to e^+\gamma$ is the very first cLFV channel searched for in experiments. The up-to-date best limit of this decay is from the MEG collaboration at PSI with data collected from 7.5×10^{14} stopped muons from 2009 to 2013. The results pushed the upper limit of branching ratio $\mathcal{B}(\mu^+ \to e^+\gamma)$ to 4.2×10^{-13} with a confidence level (CL) of 90 % [52]. Furthermore, the upgraded MEG-II aims at improving the sensitivity to 6.0×10^{-14} at 90 % CL [75, 76].

Another possible muon decay via the cLFV process is $\mu^+ \to e^+ e^+ e^-$ decay. The upper limit of

Table 2.3: Current experimental limits for various potential cLFV channels.

Type	Process	Experiment	Best Limit	C.L.
Lepton Conversion	$\mu^- N \to e^- N$	SINDRUM-II	$6.1(7.1) \times 10^{-13}$ Ti(Au)[48, 49]	90%
	$\mu^- N \to e^+ N'$	SINDRUM-II	5.7×10^{-13}[50]	90%
Muon Decay	$\mu^+ \to e^+ e^+ e^-$	SINDRUM	1.0×10^{-12}[51]	90%
	$\mu^+ \to e^+ \gamma$	MEG	4.2×10^{-13}[52]	90%
Tau Decay	$\tau^\pm \to e^\pm \gamma$	BaBar	3.3×10^{-8}[53]	90%
	$\tau^\pm \to \mu^\pm \gamma$	BaBar	4.4×10^{-8} [53]	90%
	$\tau \to eee$	Belle	2.7×10^{-8}[54]	90%
	$\tau \to \mu\mu\mu$	Belle	2.1×10^{-8} [54]	90%
	$\tau \to \mu ee$	Belle	1.8×10^{-8}[54]	90%
	$\tau \to \mu\mu e$	Belle	2.7×10^{-8} [54]	90%
Meson Decay	$\tau \to \pi^0 e$	Belle	8.0×10^{-8} [55]	90%
	$\tau \to \pi^0 \mu$	BaBar	1.1×10^{-7} [56]	90%
	$\tau \to \eta e$	Belle	9.2×10^{-8}[55]	90%
	$\tau \to \eta \mu$	Belle	6.5×10^{-8}[55]	90%
	$\tau \to \rho^0 e$	Belle	1.8×10^{-8}[57]	90%
	$\tau \to \rho^0 \mu$	Belle	1.2×10^{-8} [57]	90%
	$\pi^0 \to \mu e$	KTeV	3.6×10^{-10} [58]	90%
	$K_L^0 \to \pi^0 \mu^+ e^-$	KTeV	7.6×10^{-11} [58]	90%
	$K_L^0 \to \mu e$	BNL E871	4.7×10^{-12} [59]	90%
	$K^+ \to \pi^+ \mu^+ e^-$	BNL E865	1.3×10^{-11} [60]	90%
	$J/\psi \to \mu e$	BESIII	1.5×10^{-7} [61]	90%
	$J/\psi \to \tau e$	BESIII	7.5×10^{-8} [62]	90%
	$J/\psi \to \tau \mu$	BESII	2.6×10^{-6} [63]	90%
	$B^0 \to \mu e$	LHCb	2.8×10^{-9} [64]	95%
	$B^0 \to \tau e$	BaBar	2.8×10^{-5} [65]	90%
	$B^0 \to \tau \mu$	LHCb	1.4×10^{-5} [66]	95%
	$B \to K \mu e$	BaBar	3.8×10^{-8} [67]	90%
	$B \to K^* \mu e$	BaBar	5.1×10^{-7} [67]	90%
	$B^+ \to K^+ \tau e$	BaBar	4.8×10^{-5} [68]	90%
	$B^+ \to K^+ \tau \mu$	BaBar	3.0×10^{-5} [68]	90%
	$B_s^0 \to \mu e$	LHCb	1.1×10^{-8} [64]	90%
	$B_s^0 \to \tau \mu$	LHCb	4.2×10^{-5} [66]	95%
	$h \to \mu e$	ATLAS	6.1×10^{-5} [69]	95%
	$h \to \tau e$	CMS	2.2×10^{-3} [70]	95%
	$h \to \tau \mu$	CMS	1.5×10^{-3} [70]	95%
Boson Decay	$Z^0 \to \mu e$	ATLAS	7.5×10^{-7} [71]	95%
	$Z^0 \to \tau e$	OPAL	9.8×10^{-6} [72]	95%
	$Z^0 \to \tau \mu$	DELPHI	1.2×10^{-5} [73]	95%

Table 2.4: Key properties of muon from PDG [7].

Item	**Value**
Mass:	
m_μ [MeV]	$105.6583755 \pm 0.0000023$
Lifetime:	
τ_μ [μs]	2.1969811 ± 0.0000022
Decay mode:	
$\mathcal{B}(\mu^- \to e^- \bar{\nu}_e \nu_\mu)$	$\approx 100\%$
$\mathcal{B}(\mu^- \to e^- \bar{\nu}_e \nu_\mu \gamma)$	$(6.0 \pm 0.5) \times 10^{-8}$
$\mathcal{B}(\mu^- \to e^- e^- e^+ \bar{\nu}_e \nu_\mu)$	$(3.4 \pm 0.4) \times 10^{-5}$

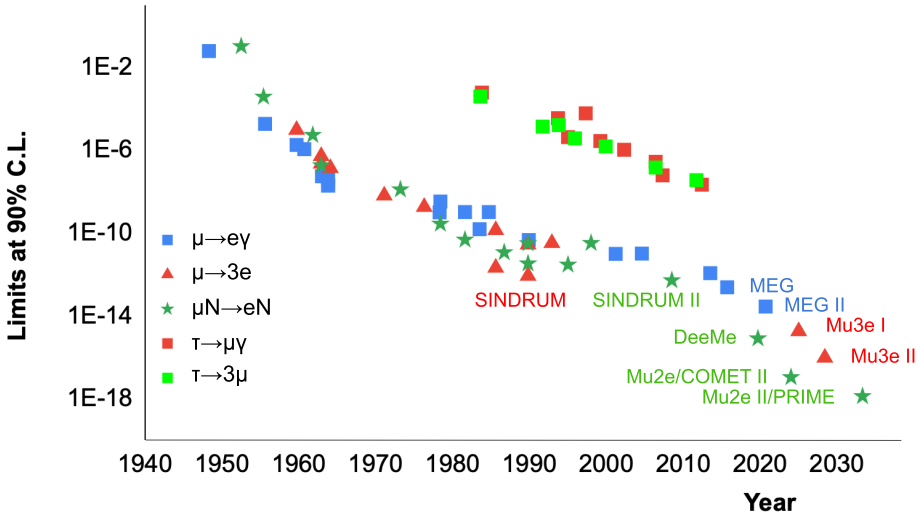

Figure 2.9: Milestones of cLFV searching. Data from [74].

branching ratio $\mathcal{B}(\mu^+ \to e^+e^+e^-)$ is 1.0×10^{-12} at 90 % CL from the SINDRUM experiment [51] at PSI. For the future, the Mu3e experiment at PSI aims to push the sensitivity's upper limit to $O(10^{-16})$ [77].

The muon conversion into the electron ($\mu^- - e^-$) in the nucleus field is another possible probe for the cLFV process. The upper limit of neutrinoless $\mu - e$ conversion to normal muon capture ratio is

$$\frac{\mu^- N \to e^- N}{\text{captured } \mu - N} < 3.3 \times 10^{-13}, \tag{2.8}$$

which is obtained by the gold target set by SINDRUM II at PSI [78]. The Mu2e experiment under construction at Fermilab uses aluminum disks target aiming at reaching a sensitivity of $O(10^{-17})$ [79]. Also, with the aluminum target, the COMET experiment at J-PARC aims for a sensitivity of $O(10^{-15})$ for Phase I and $O(10^{-17})$ for Phase II [80].

The current limits and the future experiments for the muon-related cLFV searches are summarized in Table 2.5.

Table 2.5: Current limits and planned experiments for muon-involved cLFV searches.

μ-cLFV Process	Best Limit	Planned Experiment and Goal
$\mu^+ \to e^+\gamma$	4.2×10^{-13} (MEG)	MEG-II: $\mathcal{O}(6.0 \times 10^{-14})$
$\mu^+ \to e^+e^+e^-$	1.0×10^{-12} (SINDRUM)	Mu3e-II: $\mathcal{O}(1.0 \times 10^{-16})$
$\mu^-N \to e^-N$	3.3×10^{-13} (SINDRUM-II)	Mu2e: $\mathcal{O}(3.0 \times 10^{-17})$ COMET: $\mathcal{O}(2.6 \times 10^{-17})$

Chapter 3

The Mu3e Experiment

The Mu3e experiment [81] is a novel experiment at Paul Scherrer Institut (PSI) aiming to search for the cLFV by searching for the anomalous decay $\mu^+ \to e^+e^+e^-$. As discussed in Chapter 2, the branching ratio of this decay in the SM is undetectable ($\mathcal{B}(\mu^+ \to e^+e^+e^-) < 10^{-54}$). However, many new theories beyond the SM predict enhanced rates for both loop diagrams and tree diagrams. Figure 3.1(a) gives an example of this decay with supersymmetric particles running in a loop of the γ/Z-penguin diagram. Furthermore, Figure 3.1(b) presents a possible decay at the tree level with a new particle as the mediator.

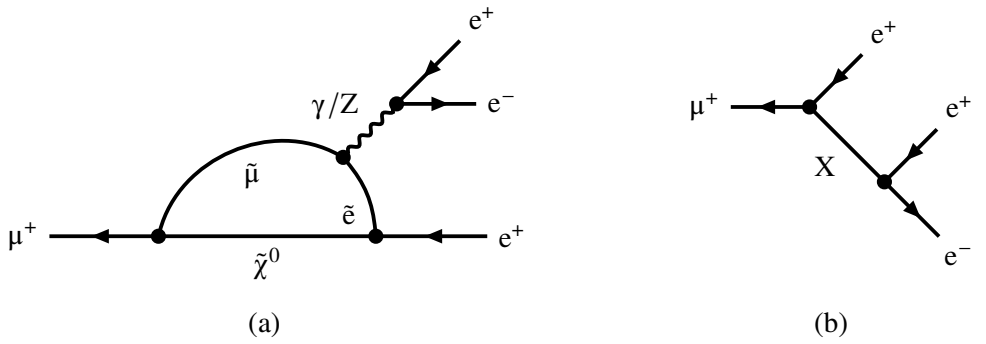

Figure 3.1: Feynman diagram examples of $\mu^+ \to e^+e^+e^-$ via (a) sparticles in the γ/Z-penguin loop and (b) new particle in the tree-level diagram.

Due to its strongly suppressed branching ratio in the SM, any observation of the decay would be a clear signal for the New Physics. And the goal of the Mu3e collaboration is to build an experiment with a sensitivity of 10^{-16} at 90 % CL to search the $\mu^+ \to e^+e^+e^-$ decay, which would improve the up-to-date sensitivity by four orders of magnitude. Thus, the Mu3e would observe this rare decay if its branching ratio is $> 10^{-16}$. Otherwise, the Mu3e would push the upper limit of the branching ratio to $O(10^{-16})$.

This chapter will first introduce the challenges of the $\mu^+ \to e^+e^+e^-$ detection, mainly signal acceptance and background suppression. Secondly, the experimental design will be briefly described. The last section will present a more detailed introduction to the Mu3e Tile Detector which the author is working on.

3.1 Challenges

This section will describe the two main challenges, signal acceptance and background suppression of the experiment, which motivate the experimental design.

3.1.1 Signal acceptance

Although the LFV mechanism in the $\mu^+ \to e^+e^+e^-$ process is unknown, the effects of different decay dynamics can still be studied based on the general parameterized Lagrangian proposed by Kuno and Okada [82]:

$$\begin{aligned} L_{\mu\to eee} = -\frac{4G_F}{\sqrt{2}}[&m_\mu A_R \bar{\mu}_R \sigma^{\mu\nu} e_L F_{\mu\nu} \\ &+m_\mu A_L \bar{\mu}_L \sigma^{\mu\nu} e_R F_{\mu\nu} \\ &+g_1(\bar{\mu}_R e_L)(\bar{e}_R e_L) \\ &+g_2(\bar{\mu}_L e_R)(\bar{e}_L e_R) \\ &+g_3(\bar{\mu}_R \gamma^\mu e_R)(\bar{e}_R \gamma_\mu e_R) \\ &+g_4(\bar{\mu}_L \gamma^\mu e_L)(\bar{e}_L \gamma_\mu e_L) \\ &+g_5(\bar{\mu}_R \gamma^\mu e_R)(\bar{e}_L \gamma_\mu e_L) \\ &+g_6(\bar{\mu}_L \gamma^\mu e_L)(\bar{e}_R \gamma_\mu e_R) \\ &+\text{H.c.}], \end{aligned} \tag{3.1}$$

where the couplings constants $A_{R,L}$ are mainly contributing from the photonic process (γ-penguin diagram in Figure 3.1(a)), while the form factors g_{1-6} describe the general direct four-fermion interactions, where the tree diagram as shown in Figure 3.1(b) contributes at leading order.

Different signal models can be generated by varying LFV couplings strength ($A_{R,L}$, g_{1-6}), which is significant for the signal acceptance study. With various coupling strengths, the energy distribution of the highest-energy decay particles (E_{max}) and the fraction of events where all decay particles have transverse momentum $p_T > p_{T,min}$ are shown in Figure 3.2.

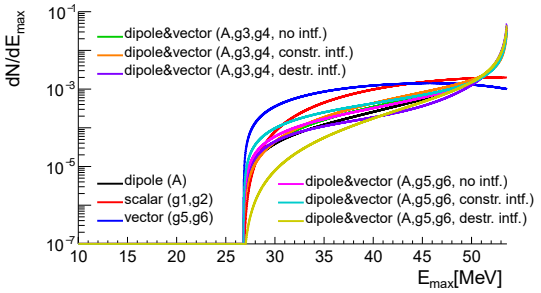

(a) Energy distribution of E_{max}.

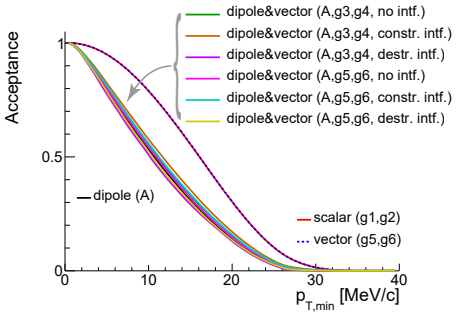

(b) Signal acceptance along $p_{T,min}$.

Figure 3.2: Simulation results of E_{max} and acceptance of Mu3e experiment. (a) Energy distribution of the highest energy particle from $\mu^+ \to e^+e^+e^-$ decays. (b) Signal acceptance along different minimal transverse momentum $p_{T,min}$ for different effective LFV models, where acceptance is defined as the fraction of $\mu^+ \to e^+e^+e^-$ decays where all three decay particles have transverse momentum $p_T > p_{T,min}$. Both figures from [83] based on [82].

One big challenge of the Mu3e experiment is the requirement of high signal acceptance. Because $\mu^+ \to e^+e^+e^-$ is a three-body decay without known kinematics, the signal acceptance has to be as high as possible to cover a large parameter space of New Physics. On the one hand, the highest energy of the decay particles (see Figure 3.2(a)) indicates that the experiment must be able to reconstruct particles

with energy up to half of the muon rest mass. On the other hand, the acceptance with different minimal momentum cuts (see Figure 3.2(b)) tells that high acceptance can only be achieved with low momentum decay particles detectable. Thus, the experiment has to reconstruct tracks of the decay particles with momentum from a few MeV to half of the muon mass. It can be achieved with a large solid angle covered in the experiment, mainly limited by the mandatory room for beam entry and exit points.

3.1.2 Background suppression

The signal decay $\mu^+ \to e^+e^+e^-$ is characterized by the two positrons and one electron from the same vertex simultaneously, as shown in Figure 3.3. As the muons are stopped on the target, the total energy and momentum of the three decay products fulfill:

$$\sum_{i=1}^{3} E_i = m_\mu, \text{and } \sum_{i=1}^{3} \vec{P}_i = 0, \tag{3.2}$$

where i refers to the three products in each decay.

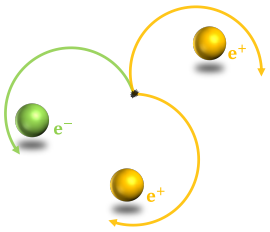

Figure 3.3: Signal of the Mu3e experiment.

The Mu3e experiment has no irreducible background because the branching ratio of $\mu^+ \to e^+e^+e^-$ decay in the SM is far below the detectable level. Thus, the sensitivity of the experiment is purely decided by the capability to distinguish the background events in two categories (shown in Figure 3.4): Internal Conversion (IC) background from $\mu^+ \to e^+e^-e^+\bar{\nu}_\mu\nu_e$ and accidental background from overlays of different processes.

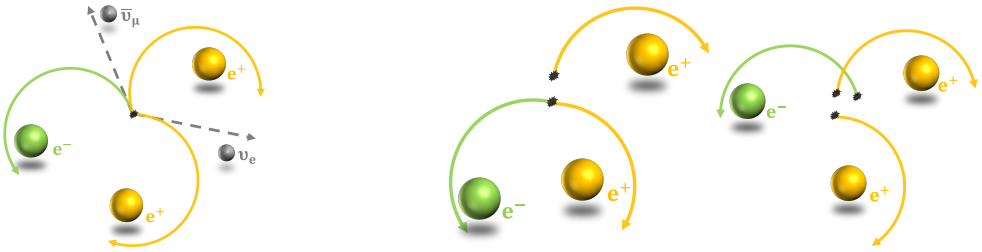

(a) IC background (b) Accidental background

Figure 3.4: Main background sources of the Mu3e experiment. (a) IC background from $\mu^+ \to e^+e^-e^+\bar{\nu}_\mu\nu_e$, where the only difference to the signal decay is the energy and momentum. (b) Accidental background due to overlays of $e^\pm$ from multiple processes, where two cases are shown. The first is the combination of two processes: a pair-production and an additional positron. The second is the combination of three processes. The electrons in the accidental background mainly come from the Bhabha scattering and pair-prodution, while the positrons are mainly from the Michel decays.

IC background Because neutrinos are invisible in the Mu3e detector system, the IC background has the same visible final state as the signal: two positrons and one electron from the same vertex simultaneously. Thus, the vertex and timing measurement cannot suppress this background. The only difference between the IC background event and the signal event is the energy difference which is carried away by the neutrinos (ν_e and $\bar{\nu}_\mu$), leading to:

$$\sum_{i=1}^{3} E_i < m_\mu, \text{and} \sum_{i=1}^{3} \vec{P}_i \neq 0. \tag{3.3}$$

Therefore, the IC background can only be distinguished by momentum measurement. Figure 3.5 gives the background contamination in the signal region, and a momentum resolution of better than 1 MeV/c is required.

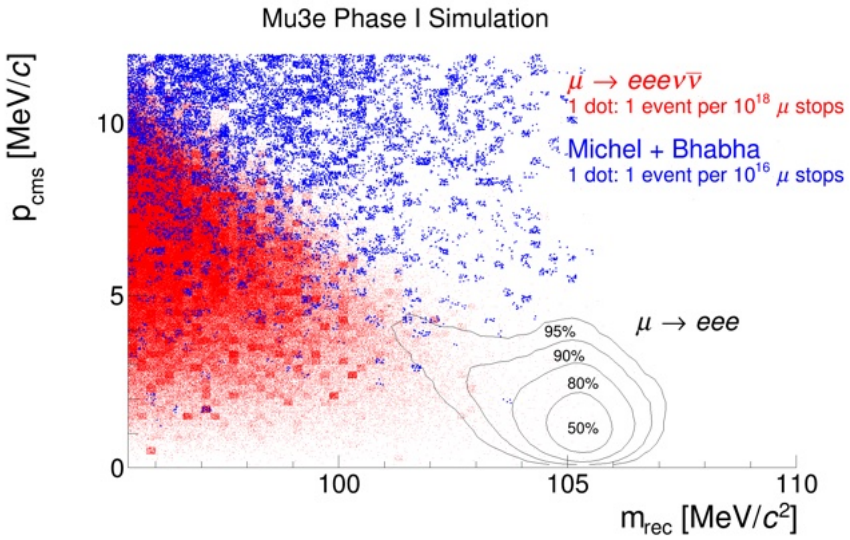

Figure 3.5: Reconstructed center-of-mass momentum versus the invariant mass for signal and background (only IC and accidental background plotted) events. The shape of the signal contour at 90 % and 95 % comes from events where one of the track has an upward fluctuation of the energy loss in the target or the first tracker layers, which leads to a lower reconstructed invariant mass and a larger reconstructed center-of-mass momentum due to the imbalance. Figure from [83].

Accidental background The accidental background mimics two positrons and one electron from multiple processes. The positrons are mainly from the Michel decays ($\mu^+ \to e^+ \bar{\nu}_e \nu_\mu$) with a branching ratio close to 1. Due to low electron production directly from the muon decay, the electrons are mainly produced by Bhabha scattering ($e^+e^- \to e^+e^-$) and pair-production of γ from radiative decays ($\mu^+ \to e^+ \bar{\nu}_e \nu_\mu \gamma$). Unlike the IC background, the sources of the accidental background have no coincidence in space and time. It can be strongly suppressed by the vertexing and timing measurement. Moreover, the momentum measurement can also improve the background suppression because

$$\sum_{i=1}^{3} E_i \neq m_\mu, \text{and} \sum_{i=1}^{3} \vec{P}_i \neq 0. \tag{3.4}$$

The simulation studies suggest that, with a muon stopping rate up to 2×10^9 Hz, the timing resolution dominates the accidental background suppression. In order to reduce the accidental background by at least two orders of magnitude, a time resolution better than 100 ps was required for the Tile Detector to identify non-synchronous muon decays [83].

3.2 Experiment Design

The Mu3e experiment tries to search the $\mu^+ \rightarrow e^+e^+e^-$ decay via detecting decay products of high-intensity muon beam stopped on a double cone target. The experiment will be built in two phases as the required final muon beam with intensity of 2×10^9 μ^+/s is still being developing at PSI. Figure 3.6 illustrates the schematic view of the Mu3e experiment for both phases. Muons from the beamline stop and decay on the target located at the center. All the charged particles from the decays will propagate along a helix in the homogeneous magnetic field if their transverse momentum $|\vec{P}_T| > 0$. Therefore, the momentum can be precisely measured by the particle trajectory reconstruction primarily relying on the Pixel Detector. The Pixel Detector also provides precise decay vertices identification. Moreover, The most precise timing information is provided by the Tile Detector in both recurl stations. Furthermore, the Fiber Detector in the central station is a compromise of timing resolution on the material budget.

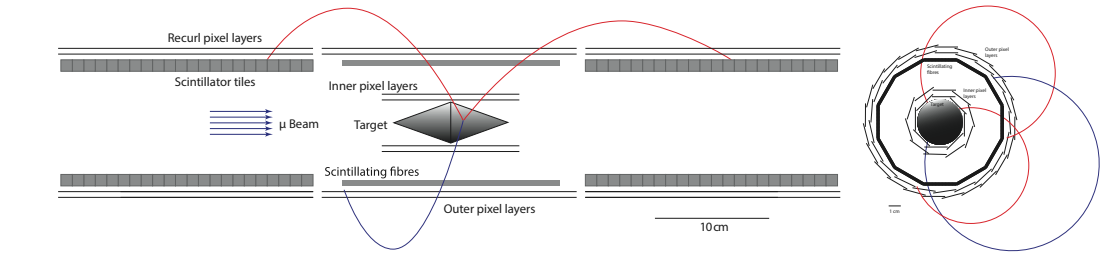

(a)

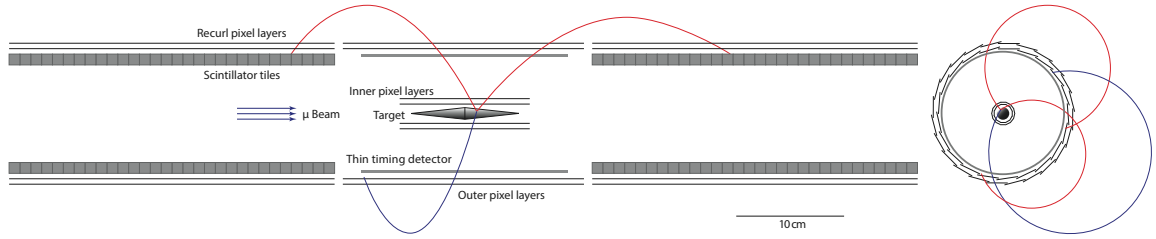

(b)

Figure 3.6: Schematic view of Mu3e experiment. (a) phase I configuration: one center detector station and two recurl detector stations. (b) phase II configuration (possible): longer recurl stations, smaller target and more segmented inner layers to extend the acceptance. Figures from [83].

The goal of the Mu3e phase I is reaching the single event sensitivity of 2×10^{-15} with more than 2.5×10^{15} muons stopped on the target, which requires a 2.5×10^7 s run time with a muon stopping rate of 10^8 μ^+/s.

This section will briefly introduce the overall Mu3e experiment design, including the muon beam, target, magnet, and detector system. In this section, only a general introduction to the Tile Detector

will be included. The section 3.3 is dedicated to the Tile Detector, where more details can be found.

3.2.1 Muon beam

Due to the experiment's high muon beam intensity requirement, the πE5 channel at PSI in Switzerland is the only choice for the Mu3e experiment. Figure 3.7 shows the structure of the πE5 channel. The muons are from the pion decays at the surface of the primary production target E (TgE) and then guided to the muon-stopping target in the Mu3e solenoid by the Compact Muon Beam Line (CMBL).

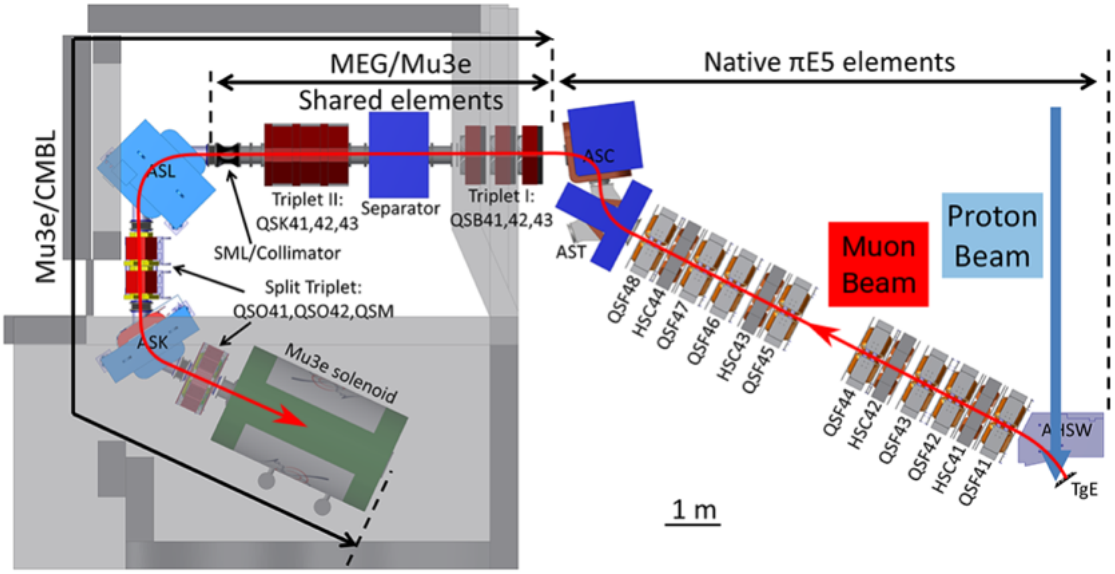

Figure 3.7: Schematic of the πE5 channel, CMBL and Mu3e solenoid at PSI. The Mu3e detector cage will be installed inside the solenoid, where 1 T magnetic field is provided. Figure from [84] based on [83].

The muon beam profile estimated by the GEANT4-based simulation software G4BEAMLINE (G4BL) [85] is given in Figure 3.8, where the Root Mean Square (RMS) of the projection on horizontal (x) and vertical (y) are $\mathrm{RMS_x} = 7.50$ mm and $\mathrm{RMS_y} = 8.74$ mm respectively.

As reported in the Technical Design Report (TDR) published in 2021, the estimated muon rate at the stopping-target position is around $(5-6)\times10^7$ μ^+/s at 2.4 mA proton beam current. Furthermore, an intensity of $(7-8)\times10^7$ μ^+/s at 2.4 mA proton beam current can be reached using the 60-mm production target or the 40-mm long slanted target. Further enhancement to fulfill the Mu3e phase I requirement, 10^8 μ^+/s, is still under study. Moreover, it was reported that the final intensity of 2×10^9 μ^+/s will be reached after 2026 [86].

3.2.2 Stopping target

The biggest challenge of the target design is optimizing the stopping power to stop as many as possible of the muons while minimizing the material added to the experiment, because the low energy of the decay particles makes the measurement very sensitive to the material budget. Many target shapes were studied, and a hollow double-cone design provides the highest stopping probability with the least material.

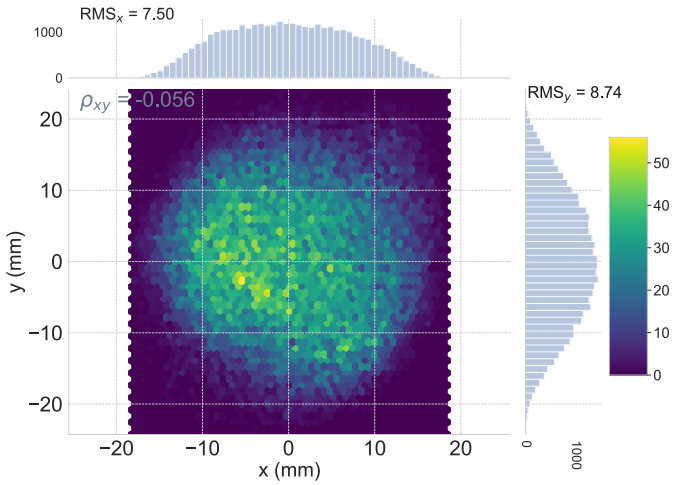

Figure 3.8: Muon beam profile estimated at the target position with G4BL model. Figure from [83].

As shown in Figure 3.9, the diameter of the target is 38 mm to match the expected beam profile shown in Figure 3.8. The total length of the target along the beam direction is designed to be 100 mm to spread the decay vertices to reduce accidental background. The low-Z Mylar foil with the thickness of 70 μm and 80 μm is employed to make the front and back part of the target, giving a total projection thickness in beam direction of 422 μm corresponding to 0.15 % of the radiation length X_0. To avoid charge accumulation from the high rate μ^+ beam, both cones' inner and outer surfaces are aluminum coated and connected to the mounting carbon tube, from which the charge can be released very quickly (Figure 3.9(b)). The studies show that 95.5 % of the muons that reach the target can be stopped [83].

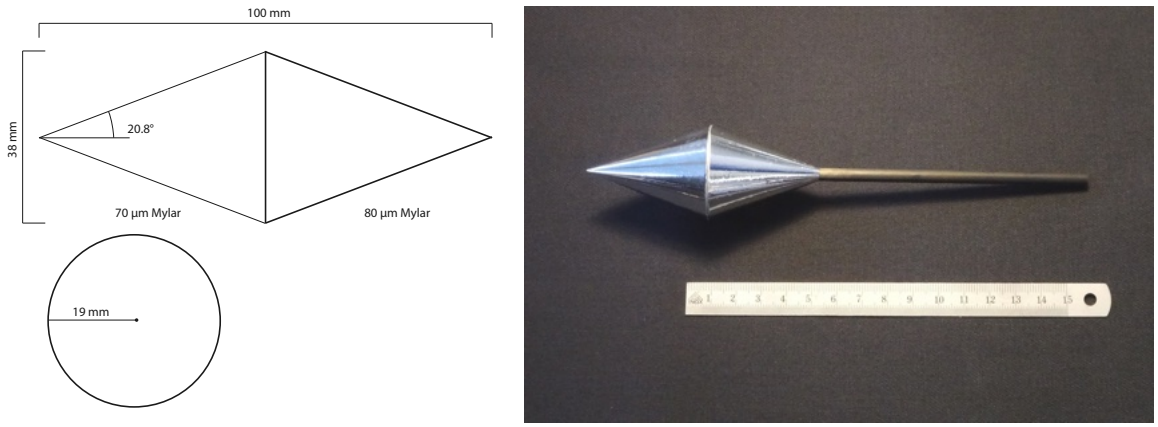

(a) (b)

Figure 3.9: The muon stopping target of the Mu3e experiment. (a) Dimensions of the baseline design and (b) a manufactured target at PSI. Figures from [83].

3.2.3 Magnet

The Mu3e magnet is a superconducting solenoidal magnet with a warm core diameter of 1 m and length of 2.7 m, which is designed and produced by Cryogenic Ltd. in the UK. Figure 3.10 shows the delivery of the magnet at PSI. The magnetic field, provided by the niobium-titanium superconducting coil with a nominal operating temperature of 4 K, is a 1 T homogeneous magnetic field to make the precise momentum measurement possible. To minimize the momentum measurement uncertainty, the magnetic field has an inhomogeneity of $\Delta B \leq 10^{-3}$ within ±60 cm around the center and long-term stability of $\Delta B \leq 10^{-4}$ in 100 days [83]. Furthermore, a rail system was equipped to insert the experimental cage into the magnet.

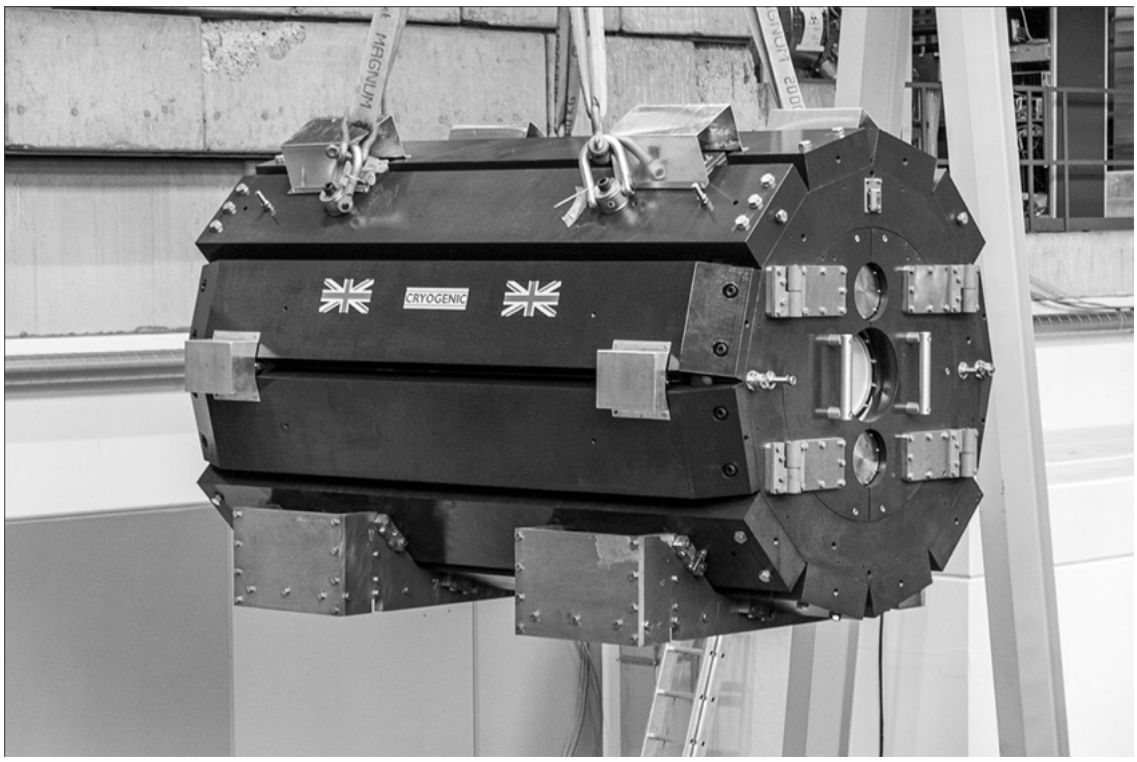

Figure 3.10: Mu3e solenoid magnet delivery at PSI. The whole magnet is shielded by a 27-ton iron coat to reduce the stray field to <5 mT at a distance of 1 m. Figure from [83].

3.2.4 Detector system

The Mu3e phase I detector system is a series of sub-detectors mounted on three stations, one central station surrounding the stopping target and two recurl stations on both sides (see Figure 3.6(a) for schematic view and Figure 3.11 for Computer-Aided Design (CAD) model). All the sub-detectors can be categorized into two systems by their purposes: tracking detector to measure hit information for accurate vertex and momentum measurement and timing detector for precise timing measurement. The detector system's overall requirement is having a momentum resolution of 0.5 MeV/c, a vertexing resolution of 200 μm and a timing resolution of <100 ps.

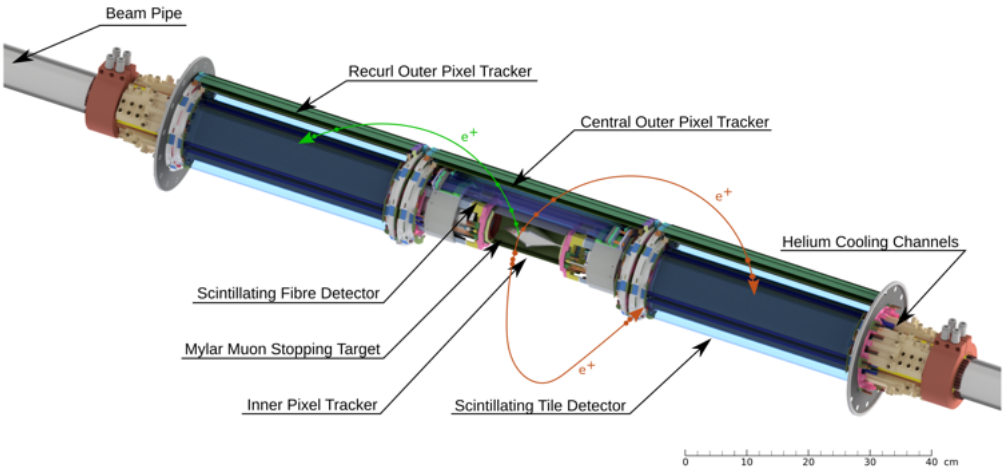

Figure 3.11: The CAD drawing of the Mu3e detector system, involving a central station in the middle and two recurl stations on both sides. Only a part of the components are shown for better view. Figure from [87].

Tracking detector

The tracking detector is divided into the inner Pixel Tracker, the innermost two layers on the central station, and the outer Pixel Tracker, which consists of the outer two layers covering all three stations. Each layer of both the inner and outer Pixel Trackers is a series of MuPix sensors glued on high-density interconnects (HDI). The MuPix sensor is a High-Voltage Monolithic Active Pixel Sensor (HV-MAPS) specifically designed for the Mu3e tracking detector [88], and the HDI is a flex circuit made of aluminum-polyimide laminates [84]. Figure 3.12 illustrates the Pixel Tracker of the central station and Figure 3.13 shows the pictures of the assembled detectors.

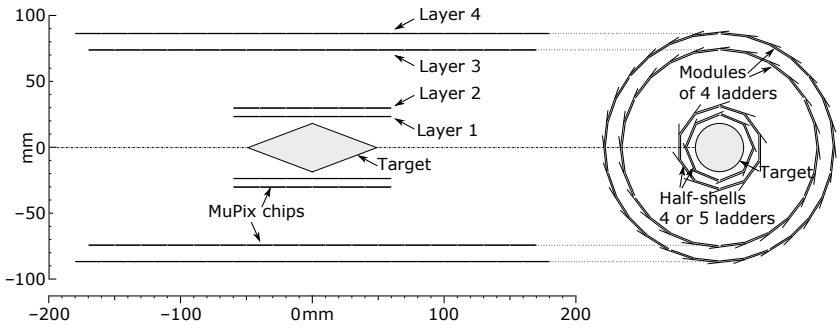

Figure 3.12: The Pixel Tracker geometry on the central station. (left) The small gaps inside each layer is the gap between different MuPix sensors. Figure from [83].

To achieve the precise vertex and momentum measurement, the MuPix sensor has to reach a hit efficiency of ≥99 % and a time resolution of ≤20 ns with minimal sensor thickness and power consumption. The final prototype of large MuPix, MuPix10 [87–89], fulfills the requirement with a hit efficiency of >99.9 % (noise-per-pixel-rate of <2 Hz) and an intrinsic timing resolution of 6(±1) ns. Also, to meet the spatial resolution and material budget requirement, the MuPix10 is designed with a pixel size of $80 \times 80 \mu m^2$ and a thickness of 50 μm.

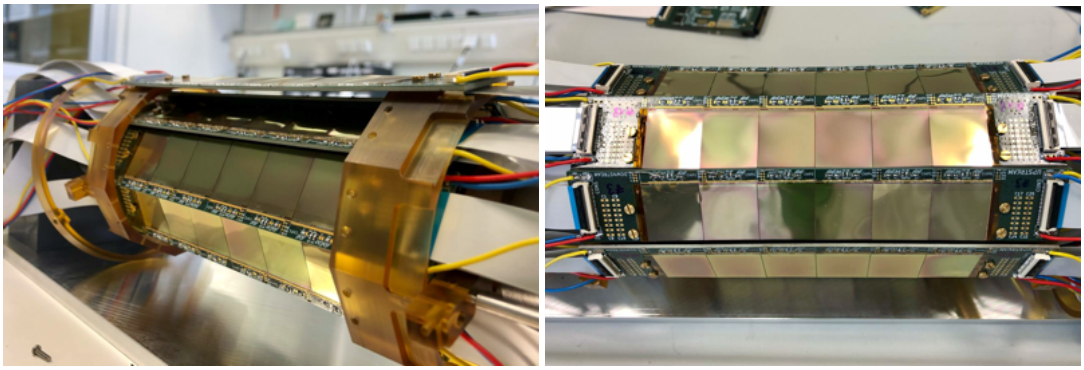

Figure 3.13: Fully assembled (left) layer 1 and (right) layer 2 of the Pixel Detector. Figures from [84].

Timing detector

The timing detector involves two types of subdetectors: the Tile Detector and the Fiber Detector. Due to similar purposes, good timing measurement with high efficiency, they have many of the same features. Both detector designs are based on scintillation material and a photon sensor, in which visible photons are generated by scintillation material and then collected by the photon sensor. Both detectors choose a low-Z plastic scintillator for photon generation, SiPM for photon collection, and the common Application Specific Integrated Circuit (ASIC), MuTRiG (Muon Timing Resolver including Gigabit-link) [90], for signal readout. Of course, the difference in requirements still leads to different characteristics of those two detectors, which will be discussed in the following two paragraphs.

Fiber detector The Fiber Detector comprises 12 scintillation-fiber ribbons with a size of $300(L) \times 32.5(W)\text{mm}^2$ coupled to SiPMs on both sides, see Figure 3.14. Due to the location 5 mm below the outer Pixel Detector in the central station, the Fiber Detector is a compromise of timing resolution and the material budget. It is minimized to X/X_0 ~0.2 % with three layers of round fibers assembled as shown in Figure 3.14(b). Moreover, the 128-channel SiPM array on each side of the fiber ribbon is read out by 4 MuTRiGs, and a timing resolution of about 250 ps was obtained [83].

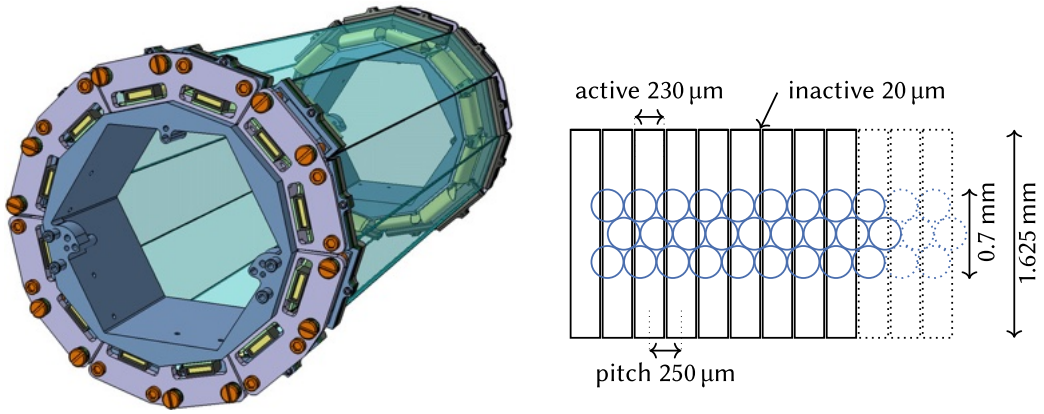

(a) (b)

Figure 3.14: (a) The Fiber Detector CAD drawing and (b) schematic of scintillation fibers mapping on SiPMs, where the rectangles represent SiPMs and the circles represent fibers' cross-section [83].

Tile detector The Tile Detector is mounted on both recurl stations below the outer Pixel Detector layers. The Tile Detector has no material budget limit because it is expected to be the last detector hit by the decay particles. So it is only optimized for superior timing resolution with high efficiency close to 100 %. The Tile Detector has two stations, each with 7 modules, as shown in Figure 3.15. The station is designed with a length of 34.23 cm to fulfill the acceptance requirement and a outer diameter of 6.41 cm limited by the inner diameter of the outer Pixel Tracker. The precise timing measurement is achieved based on the fast physics processes in the scintillation tile and SiPM, as well as the excellent timing performance of the MuTRiG chip for signal readout. As a result, a timing resolution of <50 ps was obtained in the beam test campaign at Deutsches Elektronen-Synchrotron (DESY), Hamburg [91]. More details about the Tile Detector will be discussed in section 3.3.

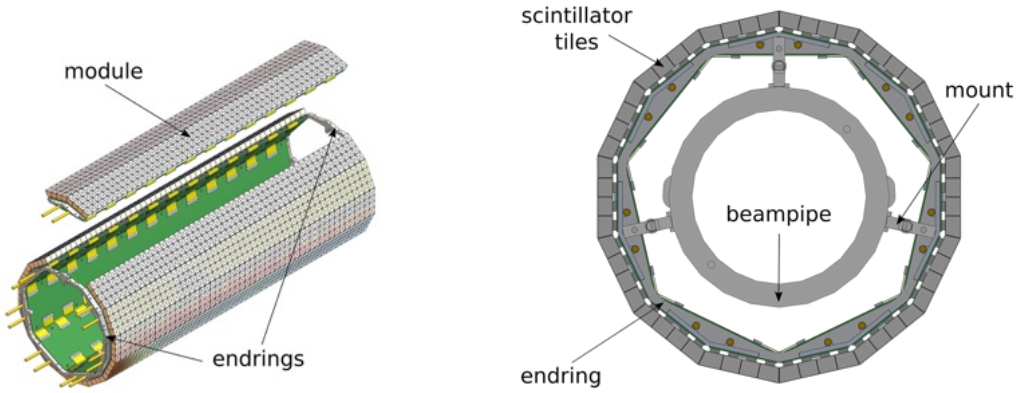

(a) (b)

Figure 3.15: The CAD drawing of one full Mu3e Tile Detector station. (a) exploded view and (b) front view. Each station consists of seven Tile Detector Modules mounted on two endrings. Figures from [83].

3.3 Tile Detector

As mentioned in section 3.2, the Tile Detector is the detector that provides the most precise timing measurement in the Mu3e experiment. This section will present more details about the design to show the approach to meet the requirement: timing resolution below 100 ps at an efficiency close to 100 %.

Particle information detection can be roughly categorized into two sub-processes: (1) the transformation of particle information to the electronic signal, which includes the interaction of the particles and the front-end sensor and the signal transform to electronic form; (2) the obtainment of interesting information via specific algorithms. Following this logic, this section will first discuss the front-end sensor design, which is used to transform particle energy into an electronic signal, and then introduce the timing discrimination algorithm in the design. Moreover, the support system for the Tile Detector, including the power supply and cooling system will also be discussed at the end of this section.

3.3.1 Front-end sensor

The front-end sensor of each Tile Detector channel consists of a scintillation tile, converting deposited particle energy to a large number of visible photons, and a SiPM, collecting photons and transferring to the corresponding electronic signal.

Scintillation tile Two main categories of scintillators commonly used in particle physics detectors are organic and inorganic scintillators. Due to its relatively low price and fast decay time, the organic scintillator is the better option for the Tile Detector in the Mu3e experiment.

Based on previous studies [4], the plastic scintillator EJ228 [92], a typical organic scintillator, was chosen as the baseline scintillation material. EJ228 gives the best timing resolution because of its high light yield and fast decay time. More key properties are shown in Table 3.1. The nominal light yield of EJ228 is 10 200 photons/MeV for electron, and the peak of the emission spectrum locates around 391 nm (Figure 3.16). The rise time and decay time of the scintillator are 0.5 ns and 1.4 ns, respectively. The large number of photons give a small statistic uncertainty leading to better timing resolution. At the same time, the fast response also results in better timing with more concentrated photon distribution in time.

Table 3.1: Key properties of scintillator EJ228. Data from [92].

Property	Value
Light Yield [photons/MeV (e^-)]	10200
Rise Time τ_r [ns]	0.5
Decay Time τ_d [ns]	1.4
FWHM of Pulse Width [ns]	1.2
Density [g/cm^3]	1.023
Refractive Index	1.58
Softening Point [°C]	75
Temperature Range [°C]	-20 to 60

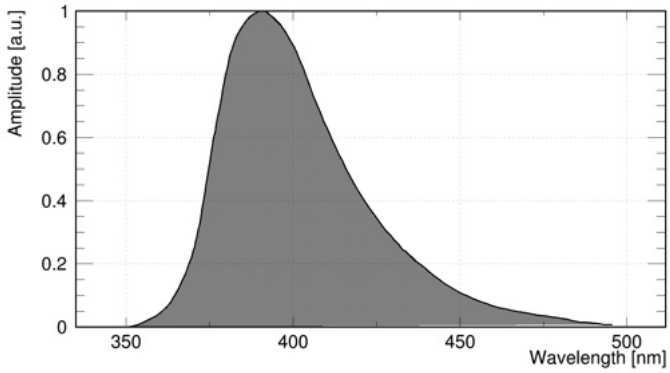

Figure 3.16: Scintillation photon spectrum of EJ228, where the spectrum peak locates at around 391 nm. Data from [92].

The scintillation tile is designed to have a geometry of $6.3 \times 6.2 \times 5.0\,\mathrm{mm}^3$, as shown in Figure 3.17. To cover the full angle of the cylinder (along ϕ), half of the tiles are beveled by 25.7°, which are referred to as *edge tiles* due to their edge position in the Tile Detector Module (see Figure 3.17(b)). The other half of the tiles are named *central tiles*. All the tiles are wrapped with Enhanced Specular Reflector (ESR) foil [93] individually to enhance the photon collection and avoid optical crosstalk between channels. The laser-cut ESR foils for individual tiles are shown in Figure 3.17(c), where the photons are read out via the $3 \times 3\,\mathrm{mm}^2$ window. Two wrapped tiles are shown in Figure 3.17(d), and the window will couple to the SiPM active area via optical grease for better photon collection.

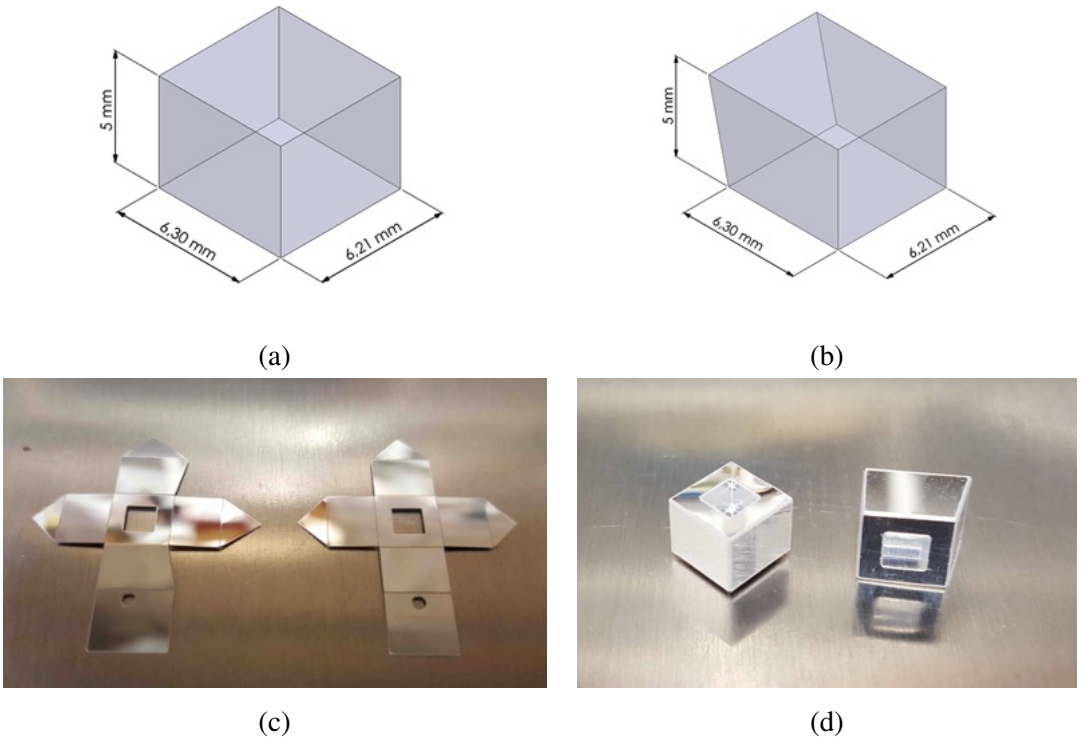

Figure 3.17: Scintillation tiles for the Mu3e Tile Detector : (a) geometry of the central tile, (b) geometry of the edge tile, (c) ESR reflective foils for (left) edge and (right) central tiles, and (d) individually wrapped (left) central and (right) edge tiles.

SiPM SiPM, an array of parallelly connected Single Photon Avalanche Diode (SPAD), is the state-of-the-art type of solid-state photo-sensor.

SiPM has become one of the most favored sensors in scientific applications after development in the past decades. Its success is mainly attributed to its key advantages, such as:

- mechanical and electrical ruggedness due to the well-developed semiconductor packaging technology and no need for an extreme operation environment, like the vacuum for Photomultiplier Tubes (PMTs);
- easy integration due to its compactness;
- insensitivity to magnetic fields due to its strong field and small distance in the avalanche region;
- low operation voltages <100 V;

- uniformity in characteristics among massive fabrication due to the standardized semiconductor production;
- high Quantum Efficiency (QE);
- low price for mass production.

A comparison of a series of SiPMs for the Tile Detector was conducted [4], and the best performance was achieved with the SiPM S13360-3050VE from Hamamatsu [94]. Some key properties are listed in Table 3.2. This SiPM has a pixel size of 50×50 µm^2 in an active area of 3×3 mm^2, which avoids saturation while ensuring a high fill factor and photon detection efficiency (PDE). The PDE distribution along wavelength is plotted in Figure 3.18a, whose peak roughly matches the peak of the photon emission spectrum of EJ228, leading to a high overall energy-to-detected-photon conversion efficiency. Figure 3.18b shows the photon spectrum from EJ228 with and without PDE considered, which gives an overall PDE

$$\epsilon_{\text{all}} = 34.84\,\%. \tag{3.5}$$

Table 3.2: Key properties of SiPM S13360-3050VE from Hamamatsu. Data from [94].

Property	Symbol	Value
Active Area [mm^2]	-	3×3
Pixel Size [µm^2]	-	50×50
Number of Pixel	N_{pixel}	3584
Fill Factor [%]	-	74
Refractive Index of Window	n_{win}	1.55
Operation Temperature [°C]	T_{opt}	-20 to 60
Typical Gain	M	1.7×10^6
Breakdown Voltage [V]	V_{br}	53±5
Temperature Coefficient [mV/°C]	$\Delta T_{V_{\text{opt}}}$	54

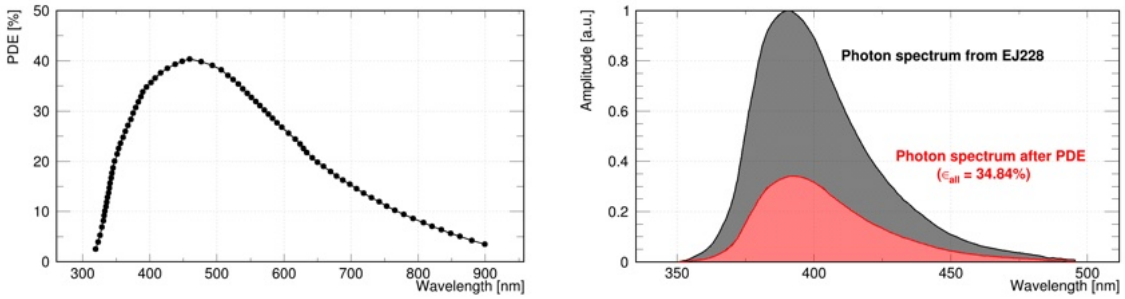

(a) PDE of SiPM

(b) Photon spectrum with/without PDE

Figure 3.18: PDE of SiPM S13360-3050VE [94] and its influence on the photon spectrum. (a) PDE of the SiPM used in the Tile Detector, with the peak located at approximately 450 nm. (b) The photon spectrum from EJ228 before and after accounting for SiPM photon detection, resulting in an overall PDE of 34.84 %.

The differential-readout technique is implemented to optimize the Tile Detector timing in the readout circuit design, illustrated in Figure 3.19. The positive signal P readout port is directly coupled to the SiPM anode. In contrast, the negative signal N is coupled to the cathode via the capacitor C_0 =100 nF. A resistor R_0=1 kΩ is employed for circuit protection. Based on this design, the rise time τ_r of the SiPM signal is around 1 ns which suppresses the timing jitter contributed by the electronic noise, while the decay time τ_d is around 30 ns avoiding the adjacent events pile-up at a high rate. The ports P and N are the differential signal couple that will feed to the readout chip MuTRiG. Moreover, the V_{bias} port will connect to the common High-Voltage (HV) power supply for all the SiPMs. More technical design details will be introduced in subsection 3.3.3.

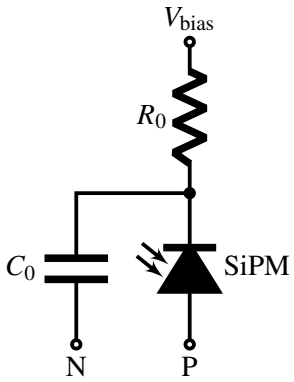

Figure 3.19: Differential read-out circuit design for single Tile Detector SiPM.

3.3.2 Timing discrimination

To obtain a precise time stamp from the SiPM signal, a leading edge timing discrimination algorithm was implemented in the readout chip MuTRiG, specifically designed 32-channel ASIC for the readout of timing detectors in the Mu3e experiment.

As illustrated in Figure 3.20, two different thresholds are employed to discriminate the signal from the Tile Detector SiPM. The lower threshold, referred to as the timing threshold, is designed to obtain the time stamp when the leading edge crosses the threshold. With a threshold range from the single photon to a few tens photons level, an excellent timing resolution can be achieved. The higher threshold, named energy threshold, is used to measure the energy-related value Time-over-Threshold (ToT), which is a function of the detected number of photons. The primary purpose of the ToT is used for time-walk correction and noise filtering in later data analysis. Both timing and energy outputs from the discriminators are digitalized by a time bin size of 50 ps. Figure 3.21 also shows the process from the SiPM input signal to the digitalized timing and energy information with the schematic of the MuTRiG single channel. The digitized event data will then send to the overall Mu3e DAQ system.

3.3.3 Technical design

Due to its advantages, the modular concept is applied in the Tile Detector technical design. The Tile Detector channel is the fundamental detection element, which involves a wrapped scintillation tile, a

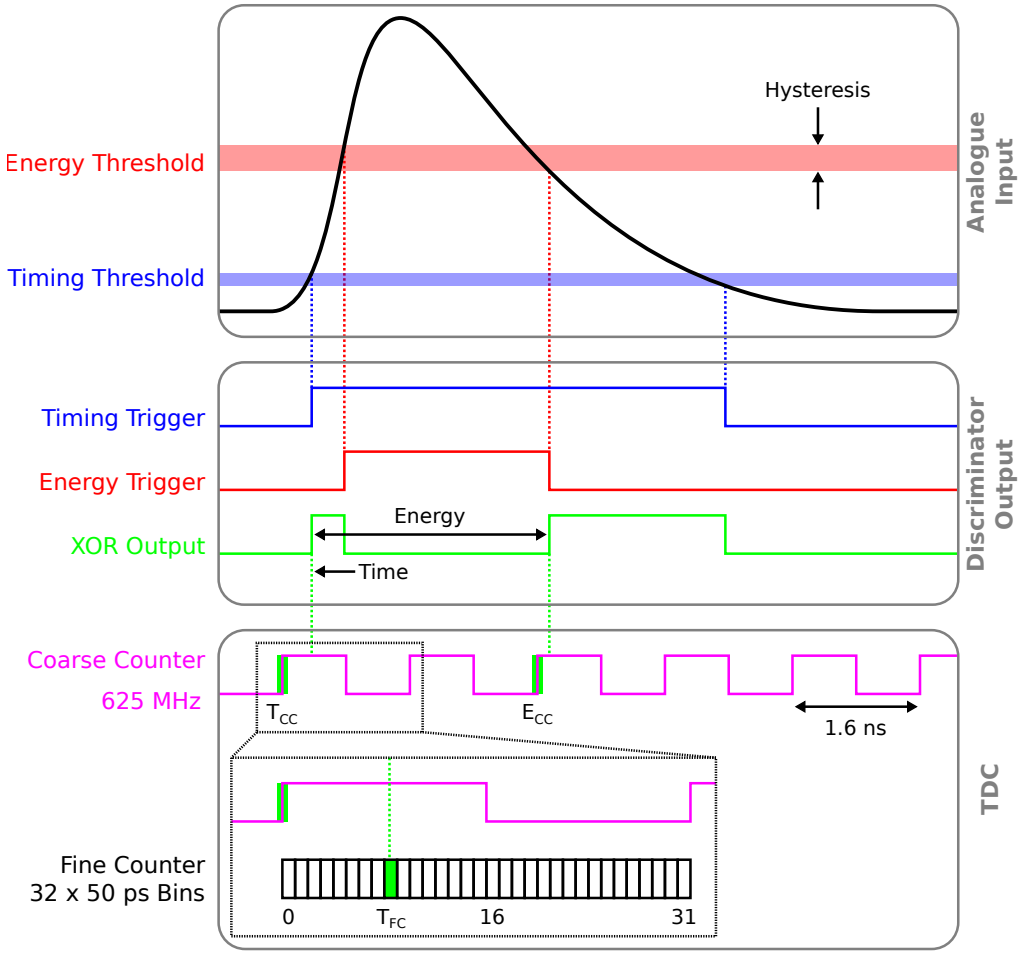

Figure 3.20: Principle of the signal discrimination in MuTRiG. The time stamp of signal's leading edge cross the timing threshold is the primary timing for the event. The energy ToT is used for time-walk correction as well as noise filtering. Figure from [83].

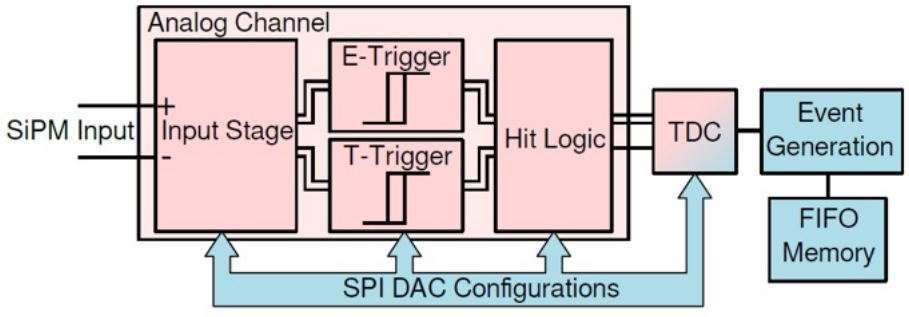

Figure 3.21: Diagram of the MuTRiG single channel. The input signal is separated to two branches: timing and energy branches. The analog process part is marked with red and the digital part is blue. Figure from [83].

SiPM and its corresponding readout electronics. Figure 3.22 gives the technical design flow chart. In the design, the base unit of the Tile Detector is the Tile Detector Matrix involving 16 channels arranged in a 4×4 matrix, and each Matrix is read out by a flexible PCB. Twenty-six matrices mounted on an aluminum cooling support structure by a 2×13 array form a Tile Detector Module. In the Tile Detector Module, every two Matrices mounted on the opposite position are read out by the same MuTRiG chip soldered on the readout board, the Tile Module Board (TMB), see Figure 3.23. Thus, every TMB includes 13 MuTRiG chips. Each Tile Detector Station includes seven Tile Detector Modules mounted on two endrings, read out by seven identical TMBs. The Mu3e Tile Detector comprises two stations mounting separately on the Upstream (US) and Downstream (DS) beam pipes.

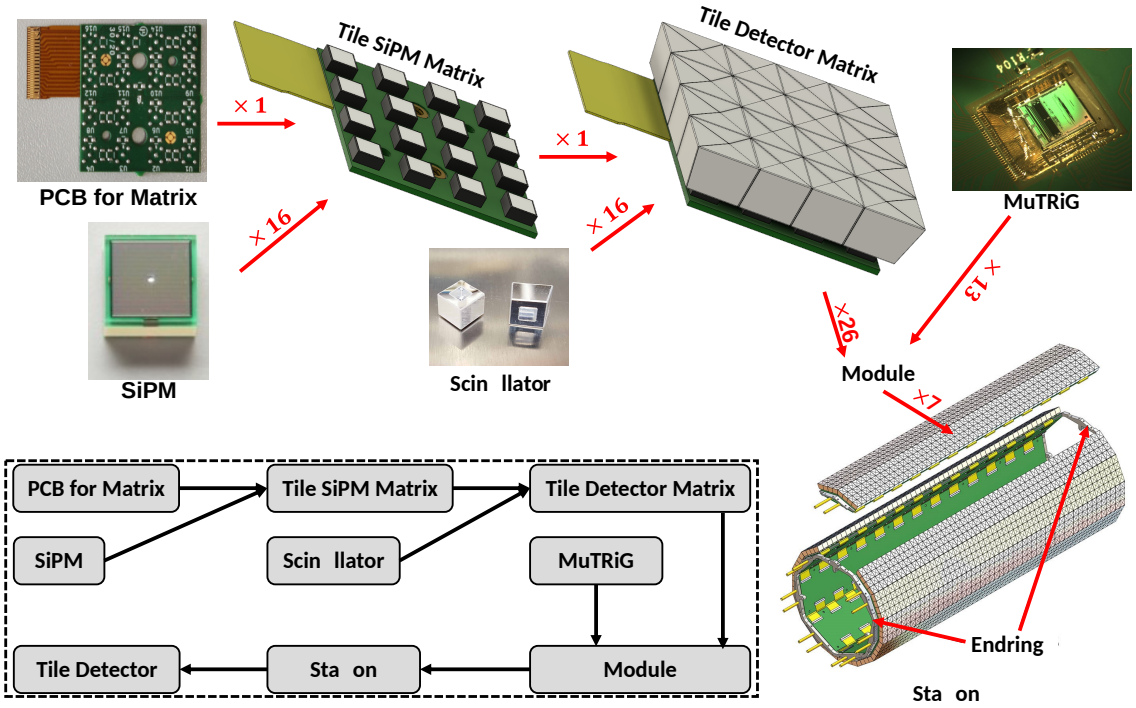

Figure 3.22: Schematic of the Tile Detector with modular concept.

Figure 3.24 illustrates the signal flow of the Tile Detector, in which the circuit of the single tile channel is shown in Figure 3.19. Every 32 differential analog signals from frond-end sensors are read out by one MuTRiG chip, where the timing and energy information is obtained and digitalized. The digital signals from all 13 MuTRiG chips are read out by the overall Mu3e DAQ via the Front-end FPGA. For the whole Tile Detector, there are, in total, 5824 analog signal lines read out by 182 MuTRiG chips. Each MuTRiG chip has one output signal line. Thus, 182 digital signal lines are feeding to the Mu3e DAQ. More details about the Mu3e DAQ can be found in [83, 95].

3.3.4 Support system

This section will introduce the support system for the Tile Detector , inlcuding cooling and low-/high-voltage power supply.

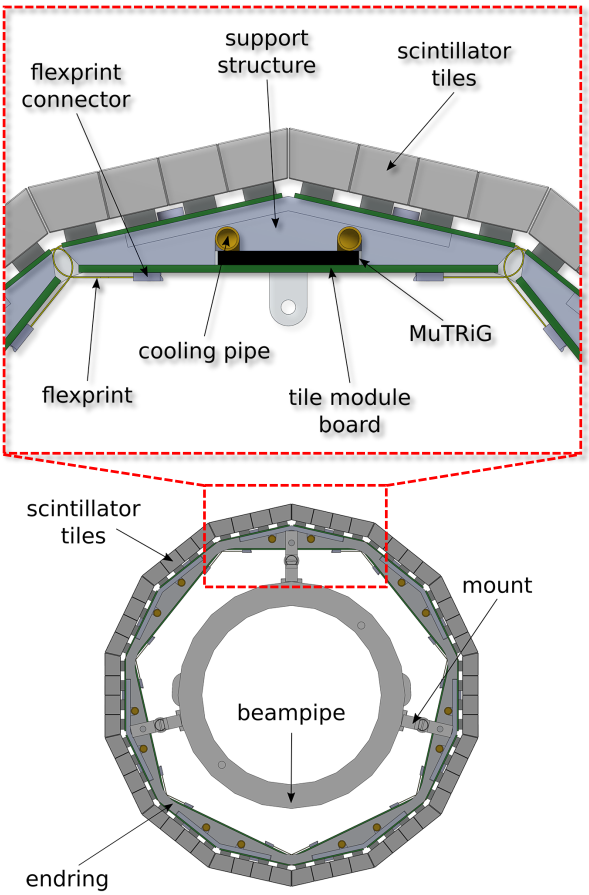

Figure 3.23: Sideview of the Tile Detector Station. Both Tile Detector Matrices and TMBs are mounted on the cooling structure directly and a thermal connection is designed for better cooling.

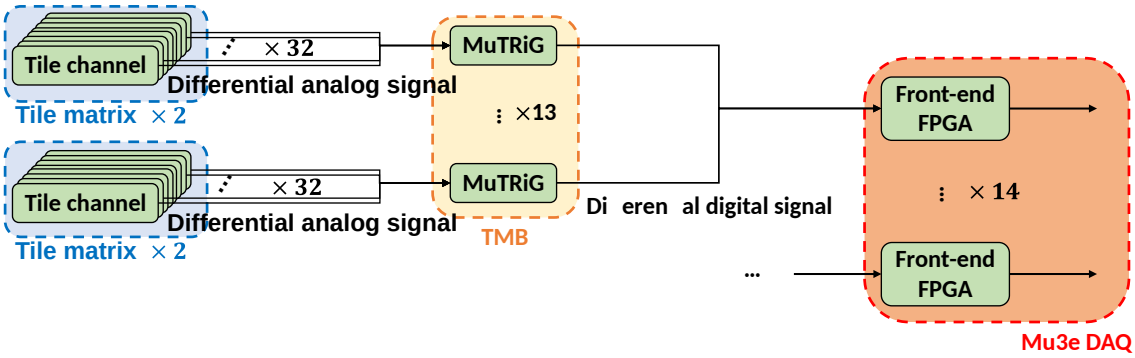

Figure 3.24: Signal flow chart of the Tile Detector.

Cooling

A stable temperature environment is significant for the consistent performance of the Tile Detector . The temperature effects on all the key components were considered before the cooling design. For the MuTRiG chip, only small impacts on threshold shift were observed within a cooling liquid temperature from around 40 °C to −35 °C. Furthermore, No timing performance deterioration was found in a 100-hour test without cooling, where the surface temperature of the MuTRiG is around 95 °C. For both scintillation tile and SiPM in the Tile Detector, an operating temperature range of −20 °C to 60 °C is suggested by the datasheet, see Table 3.1 and Table 3.2. Furthermore, the SiPM requests the temperature to be as low as possible because its Dark Count Rate (DCR) reduces when temperature decades. A small temperature fluctuation is also required due to the temperature coefficient of SiPM breakdown voltage $T_{V_{\text{br}}}$ =54 mV/°C. Overall, the temperature for the Tile Detector cooling was initially designed to be just above 0 °C to avoid surface icing.

A liquid cooling system was designed for the Tile Detector cooling[83]. As shown in Figure 3.23, all the Tile Detector components are mounted on an aluminum support structure, which is thermally connected to a metal pipe cooled by the low-temperature liquid flowing inside. The liquid is pumped from the overall Mu3e liquid cooling system. The component which produces most of the heat in the Tile Detector Module is the MuTRiG chip, with a power consumption of around 1.2 W/chip. A temperature simulation for the total Tile Detector Module was conducted with a water temperature of 1 °C at a speed of 1 m/s. With setting the environment temperature to 50 °C, a temperature of 10 °C with a maximum difference smaller than 1 °C was observed on the surface of SiPM PCBs in the whole module, which fulfills the requirement described in the SiPM datasheet [91].

It is worth noting that no irradiation behavior was described in the SiPM datasheet. This work will propose a new temperature requirement, which will be discussed in Chapter 8 with irradiation results considered.

The temperature of the SiPMs is monitored by the temperature sensor mounted on the center of each Tile Detector Matrix PCB and will be used in SiPM bias voltage correction, which can be done with the MuTRiG ASIC. There are also two more temperature sensors mounted on the TMB to monitor the temperature on the TMB surface. All the temperature sensors are read out by I2C buses, and data will be sent to the Mu3e database via the slow control data chain. Figure 3.25 shows the temperature sensor positions for SiPM temperature monitoring and structure of the I2C tree for temperature readout.

Power supply

Two types of voltages are needed for the Tile Detector: HV for SiPM bias voltage and Low-Voltage (LV) for the other electronics.

An HV up to 60 V is needed to bias the SiPMs above breakdown voltage. Each HV for a Tile Detector Module is provided by an HV board with adjustable voltage from 0 to 150 V and maximum power of 1.5 W. Moreover, the HV for individual SiPMs can be tuned by the MuTRiG chip, which allows fine tuning of bias voltage within a range up to around 0.5 V.

Two LVs are needed for the Tile Detector: 1.8 V mainly for the MuTRiG chip, and 3.3 V for the other components on the TMB. The estimated current in the normal working mode of the 1.8 V branch

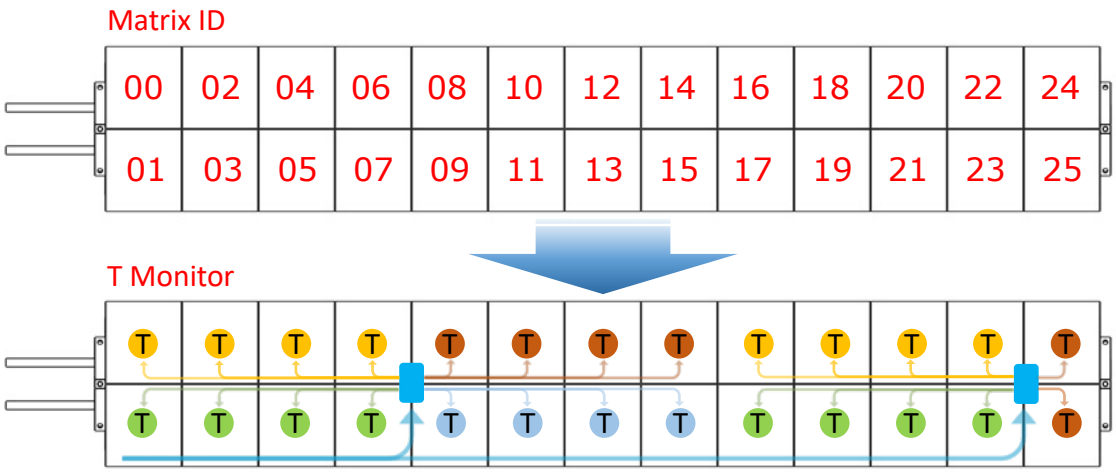

Figure 3.25: Temperature monitor of the Tile Detector Module. (up) the Tile Detector Matrix ID and (down) corresponding temperature monitor with I2C buses.

is around 9.0 A per Module with a 10 % margin involved. Due to the significant voltage drop along the power line, the output voltage to power the 1.8 V branch is set to be around 2.0 V to ensure stable MuTRiG chip performance. Moreover, the estimated current for 3.3 V is about 3.0 A.

Every Module monitors the HV power via the power measurement system of the HV board. In comparison, a sub-Module monitor system is designed on the TMB for the LV power monitor, which enables a more detailed power monitoring. The current is measured by probing the voltage drop on a small resistor, while the voltage is measured related to the corresponding ground voltage. All the 1.8 V MuTRiG chip power is monitored individually, and the 3.3 V power is monitored by one sensor on TMB. Moreover, the power data is sent to the Mu3e database with the same data chain used for temperature data.

Chapter 4

The Irradiation Challenge for the Tile Detector

Irradiation damage is a critical concern for silicon detector systems in particle physics [96, 97]. For instance, the timing resolution of SiPMs used in the MEG experiment, which shares the same muon beam as the Mu3e experiment, deteriorates by 30 % at 30 °C after exposure to a radiation field of $O(10^{11})$ e^+/cm^2 [98]. In contrast, the Mu3e Tile Detector SiPMs are subjected to a positron fluence of up to $O(10^{12})$ e^+/cm^2, which is one order of magnitude higher than the fluence experienced in the MEG experiment. Therefore, it is essential to investigate the effects of radiation on the Mu3e Tile Detector SiPMs. This chapter will first provide an overview of the mechanisms of radiation damage in silicon and its impact on SiPMs. Subsequently, a GEANT4-based simulation utilized for the Tile Detector SiPM dose estimation in Mu3e experiment will be introduced.

4.1 Irradiation Damage in Silicon

Irradiation damage in silicon is the alteration in crystalline silicon that results from a particle's energy loss in silicon. This type of damage is classified into two categories based on the energy loss processes involved. The first is surface damage, which occurs due to Ionization Energy Loss (IEL), and the second is bulk damage, which occurs due to Non-Ionization Energy Loss (NIEL) [96, 97]. The two types of effects will be described in details in the next two subsections.

4.1.1 Surface damage due to ionization energy loss

Surface damage is a type of damage that occurs due to IEL, which involves a particle ionizing the atoms through EM interaction. Figure 4.1 depicts the surface damage production process in a Metal-Oxide-Semiconductor (MOS) structure. When a particle interacts with the Silicon Dioxide (SiO_2) via EM interaction, electrons are excited to the conduction band, and electron-hole (e-h) pairs are produced. Some of the e-h pairs recombine, and the remaining electrons are swept out of the oxide slowly. The remaining holes transport to the Si-SiO_2 interface direction via polaron hopping through localized states in the SiO_2 bulk. Some of the holes fall into the relatively deep, long-lived trap states with a lifetime ranging from hours to years, resulting in stable trapped holes near the Si-SiO_2 interface. In the Si band-gap, radiation-induced traps build up right at the Si-SiO_2 interface. It is worth noting that all particles that deposit enough ionization energy to produce e-h holes have the potential to cause surface damage, including photons, charged particles, and other particles having photons or charged particles involved as secondary particles.

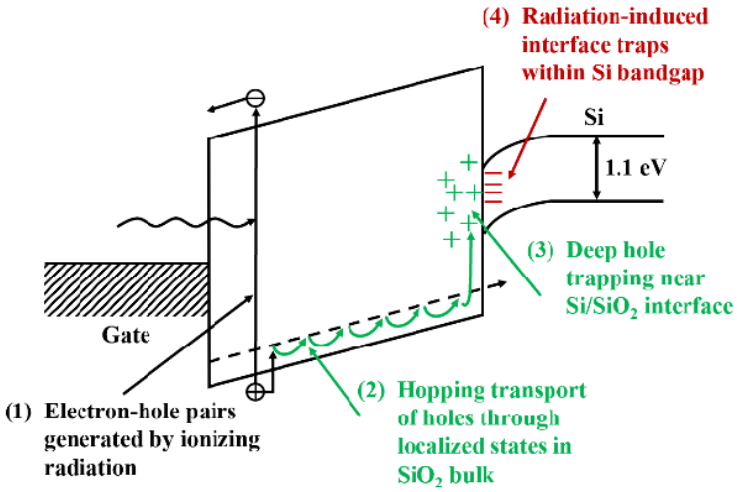

Figure 4.1: Schematic to show surface damage production process in a MOS structure due to IEL. Figure from [99].

Positively charged traps near the Si-SiO_2 interface and the interface states in the Si band-gap can cause various effects. The positive charge may lead to charge trap and release, resulting in charge loss in the main signal and increased noise. Additionally, the positive charge may alter the expected electric field, leading to changes in effects such as reduced breakdown voltage and increased depletion voltage. The IEL is quantified by the deposited ionization energy per unit mass, with the unit of gray, defined as the absorption of one joule of radiation energy per kilogram of matter.

4.1.2 Bulk damage due to non-ionization energy loss

Bulk damage in silicon refers to the displacement of silicon atoms due to a particle's NIEL, which occurs when a particle directly interacts with the nucleus via EM interactions, such as Coulomb scattering of electrons or strong interactions and nuclear scattering with neutrons. Figure 4.2 illustrates the process in which a silicon atom is kicked out of the lattice and relocated to another position, forming a vacancy and interstitial pair called a Frenkel-pair. When the energy transferred to the Primary Knock-on Atom (PKA) E_T in the scattering is higher than 25 eV, the atom can be kicked out of the original lattice and relocate to a new position. If the kinetic energy of the PKA is higher than 1 keV, additional Frenkel-pairs can be produced, resulting in a cluster defect. Furthermore, multiple-cluster defects can be formed if the PKA's energy is higher than 12 keV. Table 4.1 presents some kinematic collision properties of different particles in silicon, and Figure 4.3 illustrates some simulation results.

Some Frenkel-pairs may annihilate or diffuse out of the surface at temperature above 150 K, curing defects due to its relatively high mobility. The other Frenkel-pairs may combine with other defects and form stable defects resulting in a permanent formation or removal of donors and acceptors. For example, the combination of interstitials (I), vacancies (V) with C, O, P atoms may form VP, VO, Divacancy (V2), and Trivacancy (V3) [102]. Those stable combined defects are very stable even at room temperature, but atoms mobility can be improved with increasing temperature, which accelerates the defects' recovery, named annealing.

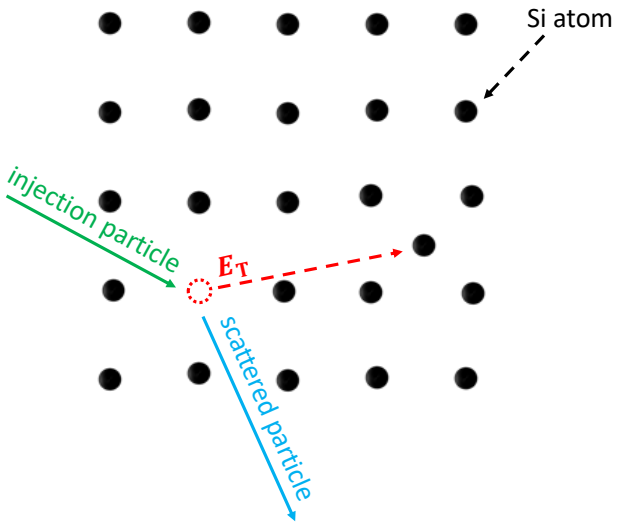

Figure 4.2: Schematic of bulk damage production: the energy transferred E_T to the silicon atom is high enough to relocate it somewhere else.

Table 4.1: Kinematic collision properties of different particles in Si, from [100], where the $E_{\mathrm{Tmax/avg}}$ is the maximum/average transferred energy to silicon atom. The E and $E_{\mathrm{min/max}}$ are energy of the particle. Energy in keV.

Particle	$e^{\pm}$	Proton	Neutron	Si^{+}
Interaction	EM	EM + strong	strong	EM
E_{min} for point	260	0.19	0.19	0.025
E_{max} for cluster	4600	15	15	2
E_{Tmax} of E=1 MeV	0.155	133.7	133.9	1000
E_{Tavg} of E=1 MeV	0.046	0.21	50	0.265

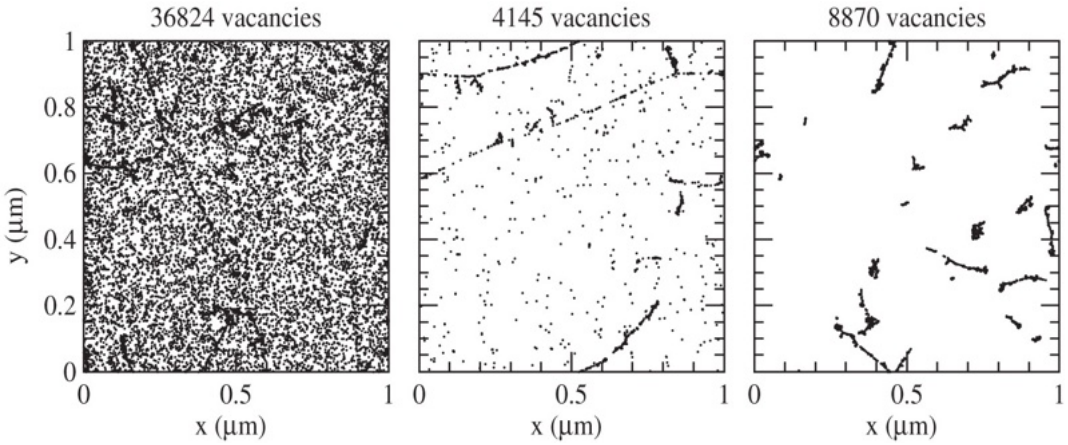

Figure 4.3: Initial distribution of vacancies produced in silicon by (left) 10-MeV protons, (middle) 23-GeV protons, and (right) 1-MeV neutrons. The plots are projected over 1 μm depth (z) and correspond to a fluence of 10^{14} particles/cm^2. Figure taken from [101].

The Shockley-Read-Hall (SRH) [103] model is commonly used to categorize the effects of bulk damage based on the defect centers in the band gap (Figure 4.4). Defects very close to the conduction (valence) band act as donors (acceptors), leading to changes in the electric field distribution in the device. Moreover, deeper defects serve as additional trapping centers for charges, resulting in a reduction in signal amplitude and an increase in correlated noise. Furthermore, defects close to the center of the energy gap increase the charge generation and recombination probability, which dominates the dramatic increase in dark current above breakdown voltage. Beyond the SRH model, the breakdown and depletion voltage will change when the effective doping density change is not ignorable. Moreover, the silicon doping type can even flip at very high radiation doses. Figure 4.5 shows an example for a silicon detector type inversion in the LHCb, which occurs around 2×10^{13} n_{eq}.

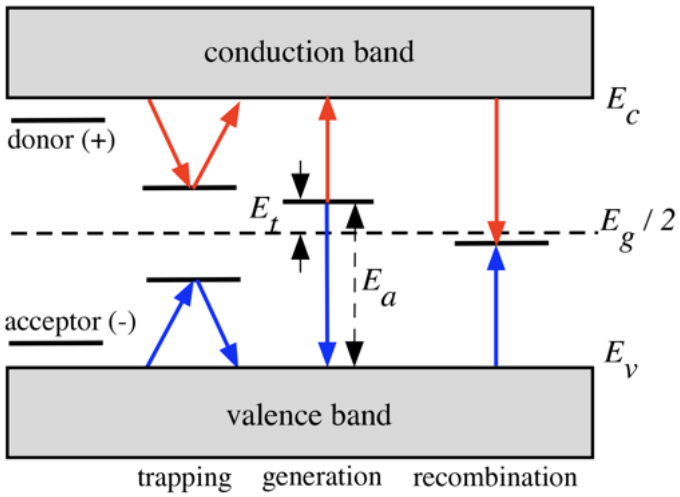

Figure 4.4: Schematic of possible effects in the band gap and its macroscopic effect on the silicon sensor. Red lines indicate movement of electrons and blue ones of holes. Figure from [103].

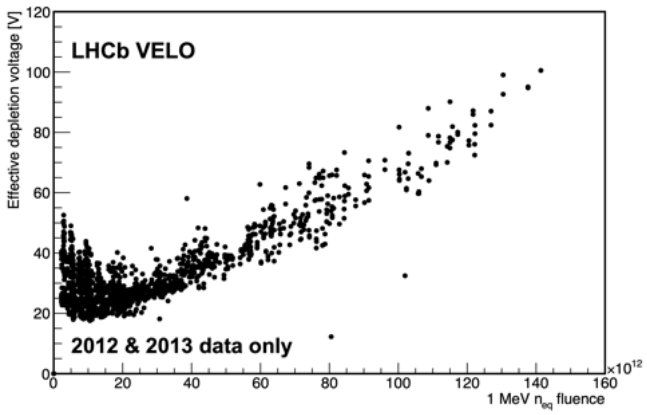

Figure 4.5: Example of effective doping type inversion in silicon detector. Figure from [104].

The NIEL hypothesis [102, 105, 106] is a method for describing the distribution of bulk damage defects (nuclear recoil) in the silicon lattice. The fundamental assumption of this hypothesis is that the bulk damage induced by the NIEL process is proportional to the energy transferred to the silicon atom E_T during that process. As a result, the NIEL value can be expressed in terms of the displacement

damage cross-section in silicon:

$$D(E) = \sum_i \sigma_i(E) \cdot \int_0^{E_{\mathrm{T}\max}} f_i(E, E_{\mathrm{T}}) P(E_{\mathrm{T}}) dE_{\mathrm{T}}, \tag{4.1}$$

which is also called damage function. This function takes all possible interaction types between incoming particles and the silicon atoms, where the index i denotes the type of interaction into account. The $\sigma_i(E)$ represents the cross-section of a specific interaction i for an incoming particle with energy E, while the $f_i(E, E_{\mathrm{T}})$ is the corresponding probability of generating a recoil atom with energy E_{T}. The Lindhard partition function [107], $P(E_{\mathrm{T}})$, is used to calculate the partition of transferred energy to displacement damage, equals to zero if the energy transfer E_{T} is below the displacement energy threshold. Figure 4.6 displays the damage function of pions, protons, neutrons, and electrons in an energy range from 0.1 meV to 10 GeV, normalized to the 1-MeV neutron with $D(E_{\mathrm{neutron}} = 1\,\mathrm{MeV})$=95 MeVmb.

The damage function $D(E)$ is not only a function of particle type but also particle energy, making it challenging to compare damage generated by different particles with individual energy spectra. To address this issue, the hardness factor, κ, is defined as the normalized integral of the particle's damage function along the corresponding energy spectrum, $\phi(E)$:

$$\kappa = \frac{\int D(E)\phi(E)dE}{D(E_{\mathrm{neutron}} = 1\,\mathrm{MeV}) \cdot \int \phi(E)dE} \tag{4.2}$$

aiming to compare NIEL-induced damage directly from different radiation. Though the NIEL scaling hypothesis is not universally and ideally valid due to its dependence on the specifics of energy transfers, it is still a useful tool to cancel out most of the particle and energy dependence to obtain an equivalent value [108].

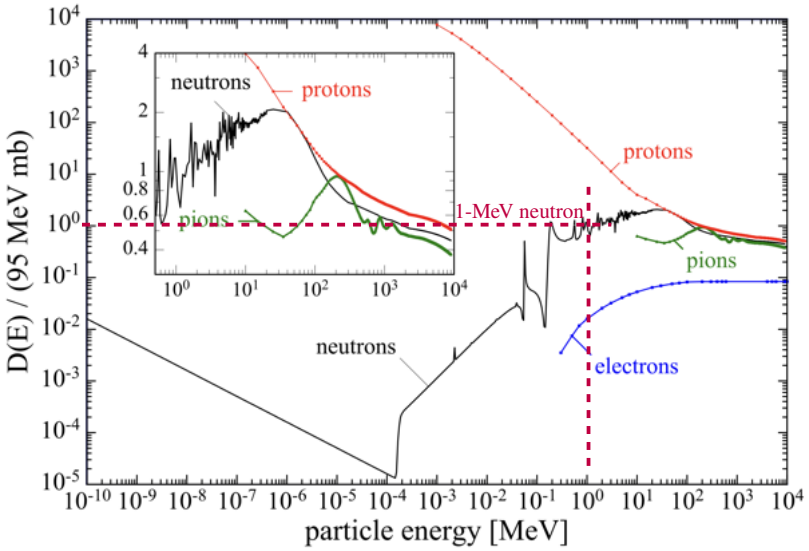

Figure 4.6: NIEL cross-sections normalized to 95 MeVmb, value for 1-MeV neutron, based on figure from [108] and data collected from [109–112].

Thus, Given a radiation field fluence Φ with an energy spectrum $\phi(E)$, the equivalent fluence Φ_{eq} can be calculated using

$$\Phi_{eq} = \kappa \cdot \Phi, \tag{4.3}$$

where the hardness factor κ is calculated based on the energy spectrum $\phi(E)$ for the corresponding particle. The unit of Φ_{eq} is 1-MeV n_{eq}/cm^2 or can be simplified to n_{eq}/cm^2.

4.2 Irradiation Environment for the Tile Detector

The primary radiation particle in the Mu3e detector is the positron from the Michel decay $\mu^+ \rightarrow e^+ \bar{\nu}_\mu \nu_e$, whose energy spectrum is shown in Figure 4.7a. Not all the positrons generated by muon decays can reach the Tile Detector in the Mu3e experiment due to the limited length of the detector, and Figure 4.7b presents the energy distribution of the positrons that reach the Tile Detector. The lower edge of the distribution is due to the minimal requirements on both the transverse momentum p_T and momentum in the z-direction p_z. Additionally, the escape of positrons with large momentum leads to a decrease in the energy range above 40 MeV. In the Phase II of the experiment, a larger momentum range will be covered due to longer recurl stations.

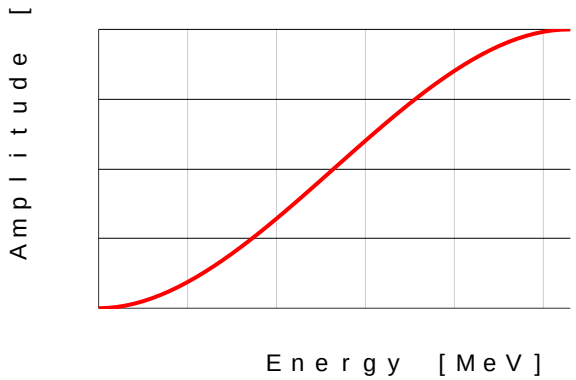

(a) Position energy spectrum from theoretical calculation.

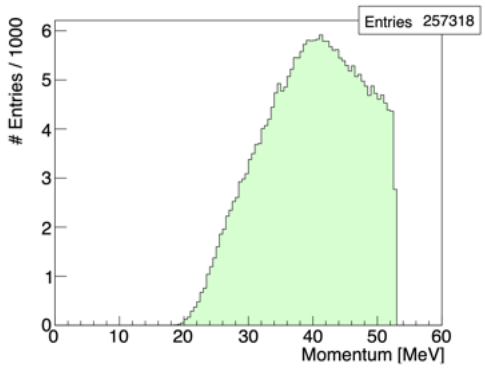

(b) Positrons reached the Tile Detector.

Figure 4.7: Energy spectrum of positron. (a) Theoretical calculation of positron energy spectrum based from Michel decay based on [113]. (b) Energy spectrum of positrons reached the Tile Detector in the Mu3e experiment based on GEANT4 simulation [114].

4.2.1 Introduction to the radiation environment

For plastic scintillation tiles, many investigations of radiation damage have been conducted [115–119]. These studies have demonstrated a reduction in output photon emission of less than 10 % at doses below 10^4 Gy. This level of radiation exposure significantly exceeds the dose anticipated in the scintillation tiles employed in the Mu3e experiment, as illustrated in section A.1. Considering that the total number of photons reaching the Mu3e Tile Detector SiPM is estimated to be greater than 3000 for each particle hitting a Tile, the potential impacts of radiation-induced timing and efficiency perturbations due to a decrease in photon emission can be deemed negligible.

The MuTRiG ASIC is not expected to experience any significant radiation effects during the Mu3e experiment, neither. Permanent damage to the ASIC only occurs with a high dose exposure, and temporary effects such as accumulated charge from IEL only impacts the ASIC under extreme conditions of high dose rate or radiation with high-energy particles.

Therefore, the SiPM is the most sensitive component to radiation damage in the Tile Detector, with previous studies reporting a significant increase in the DCR after exposure to radiation [103, 120–122]. Although the radiation-induced increase in DCR is not expected to impact the efficiency of the Tile Detector significantly due to the high number of scintillation photons, it is still a challenge for precise timing measurements. Both surface damage and bulk damage can occur in the SiPM, but bulk damage is expected to dominate the noise contribution when operating above breakdown voltage.

4.2.2 Dose simulation for the Tile Detector in the Mu3e experiment

A GEANT4-based simulation software was developed for the Mu3e Tile Detector radiation study, based on the common simulation framework. The general simulation setting, including the muon beam, magnetic field, physics process, and detector geometry, can be found in the simulation chapter (chapter 18) of Mu3e Technic Design Report (TDR) [83].

To have a more detailed simulation of the bulk damage in the silicon layer of the SiPM, the SiPM was modified to a three-layer model from the single silicon bulk used before. The implemented SiPM structure is shown in Figure 4.8, based on the SiPM dimensions from the data sheet, as shown in Figure 4.9. The active area of the Tile Detector SiPM implemented in the simulation was $3.0 \times 3.0\,\mathrm{mm}^2$. The SiPM was modeled as a stack of SiO_2 (20 μm), Si (300 μm), and bonding PCB[1].

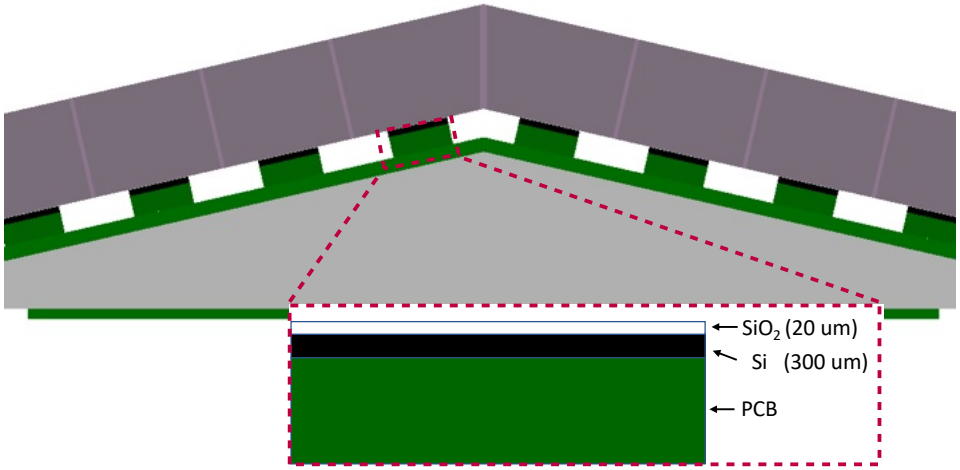

Figure 4.8: Sideview of the setting in GEANT4 simulation. The SiPM was implemented with a stack of 3 layers material: SiO_2, Si and PCB.

In a complex radiation field, Equation 4.3 cannot be directly employed for calculations due to the interdependence between overall κ and overall Φ. Individual particle data is utilized to compute the

[1] Special thanks to Hamamatsu for the data sharing.

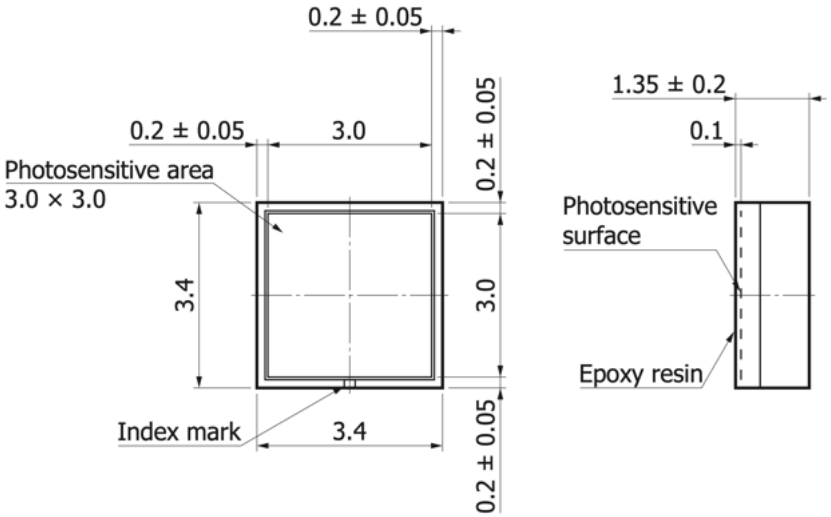

Figure 4.9: Dimension of SiPM S13360-3050VE from data sheet [94]: (left) frontview and (right) sideview. The unit of the dimension in the scratch is mm.

equivalent fluence Φ_{eq} using the following expression:

$$\Phi_{\text{eq}} = \sum_{i}^{N_{\text{type}}} \sum_{j}^{N_i} \kappa_{\text{mono}}(E_{ij}) \cdot \Phi_{ij}, \tag{4.4}$$

where N_{type} represents the number of particle types and N_i denotes the total count of the i-th particle. Additionally, the hardness factor for monoenergetic radiation, $\kappa_{\text{mono}}(E_{ij})$, can be calculated by treating $\phi(E)$ as a delta function $\delta(E - E_{ij})$:

$$\kappa_{\text{mono}}(E_{ij}) = \frac{\int D(E)\delta(E - E_{ij})dE}{D(E_{\text{neutron}} = 1\,\text{MeV}) \cdot \int \delta(E - E_{ij})dE} = \frac{D(E_{ij})}{D(E_{\text{neutron}} = 1\,\text{MeV})}, \tag{4.5}$$

where $D(E_{ij})$ signifies the damage function based on radiation type and energy, obtainable from Figure 4.6. The data points of $D(E_{ij})$ used in the simulation are provided in section A.3.

Furthermore, Φ_{ij} represents the normalized individual equivalent fluence with respect to the selected surface. For example, considering a rectangular cuboid object with an area A of interest and a thickness d, Φ_{ij} can be expressed as:

$$\Phi_{ij} = \frac{l_{ij}}{d} \cdot \frac{1}{A} = \frac{l_{ij}}{V}, \tag{4.6}$$

where l_{ij} is the path length of the monoenergetic particle traversing the silicon with volume $V = A \cdot d$ (Figure 4.10). The term l_{ij}/d corresponds to the path-weighted fluence of the individual particle, which is proportional to the path length. Moreover, $1/A$ serves as a factor to average the fluence on the surface of interest.

Consequently, based on Equation 4.5 and Equation 4.6, Equation 4.4 can be rewritten as a function of the individual path length l_{ij} and energy E_{ij} for each particle type:

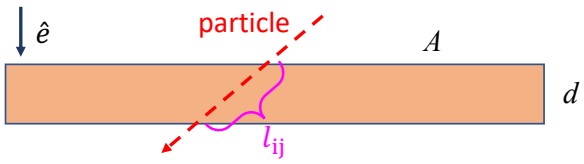

Figure 4.10: Schematic example of equivalent fluence of single particle, where $\hat{e}$ is the unit normal vector of the interested surface.

$$\begin{aligned}\Phi_{\text{eq}} &= \sum_{i}^{N_{\text{type}}} \sum_{j}^{N_i} \frac{D(E_{ij})}{D(E_{\text{neutron}} = 1\,\text{MeV})} \cdot \frac{l_{ij}}{V} \\ &= \frac{1}{D(E_{\text{neutron}} = 1\,\text{MeV}) \cdot V} \cdot \sum_{i}^{N_{\text{type}}} \sum_{j}^{N_i} D(E_{ij}) \cdot l_{ij},\end{aligned} \tag{4.7}$$

where both $D(E_{ij})$ and l_{ij} can be directly acquired from the GEANT4 simulation, while $D(E_{\text{neutron}} = 1\,\text{MeV})$ and V remain constant given the specific SiPM geometry.

In the simulation, the muon source was positioned at $-100\,\text{cm}$ with a double-Gaussian distribution. Data from approximately 1.3×10^7 stopped muons on the target were employed to determine the dose distribution and subsequently scaled to encompass the complete phase I run with an expected 2.5×10^{15} muons halted on the target. Furthermore, dose values of SiPMs sharing the same z position, 56 SiPMs on a ring, were averaged.

Figure 4.11 exhibits the simulated SiPM dose distribution along the z-direction. The maximum dose values, 2.23×10^{11} n_{eq}/cm^2 and 1.40×10^{11} n_{eq}/cm^2 for the US and DS regions respectively, are observed at the SiPMs primarily proximate to the target. And the dose decreases as the distance to the target increases. Additionally, SiPMs in the US were exposed to higher radiation compared to those in the DS, due to approximately half of the muons decaying prior to reaching the target and the supplementary dose primarily originating from secondary particles produced by these decays.

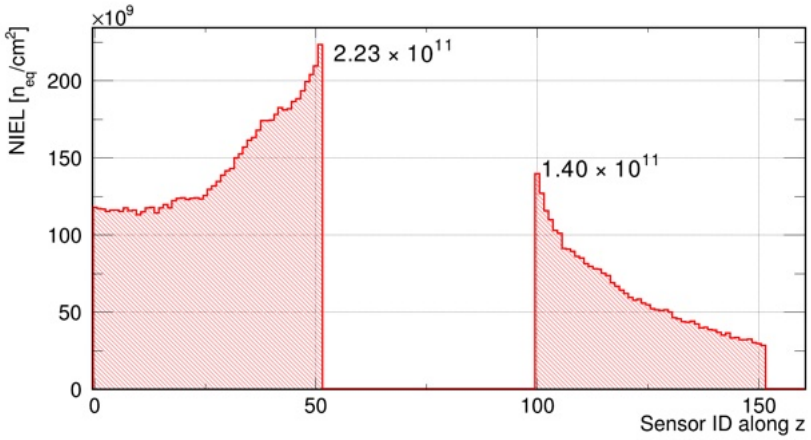

Figure 4.11: Dose distribution expected in the Tile Detector SiPM at end of the Mu3e phase I run (2.5×10^{15} muons stopped on the target). Each bin value is the average of dose values in the 56 SiPMs in the same ring at same z position. US: sensor ID from 0 to 51; DS: sensor ID from 100 to 151.

Chapter 5

Irradiation Damage Campaign for the Tile Detector

As mentioned in the previous chapter, predicting the radiation damage impacts on specific SiPMs based on the existing results in the literature is not straightforward. This is because different radiation fields (particle types and energy spectrum) have varying effects on different devices (SiPM types) and applications where distinct performance aspects are of interest.

The radiation damage to the Tile Detector primarily stems from the positrons produced in Michel decays. In order to assess the radiation damage in the real Mu3e experiment, a beam-test campaign was conducted at PSI using the πE5 beamline to expose the devices to the particle flow from muon decays, replicating both the radiation particles and the energy spectrum encountered in the experiment. This chapter will detail the experimental setup, the muon beam calibration, and the methods applied for determining the proton beam current and the muon-to-dose response which are needed for the radiation dose estimation. Furthermore, the dose in the SiPMs estimated by a GEANT4 simulation will be presented.

5.1 Radiation Damage Beam-test Campaign

To accurately simulate the radiation damage experienced in the Mu3e experiment, the same muon beam employed for the experiment was utilized for the radiation damage beam-test campaign (Figure 5.1). As described in section 3.2, the muons are generated by the proton beam from the High Intensity Proton Accelerator (HIPA) at PSI. Following the CMBL, the muons arrive at a stopping target, after which the radiation Tile Detector samples were installed. This section will initially present the muon beam information and the method employed for muon beam calibration. Subsequently, a detailed description of the irradiation setup will be presented.

5.1.1 Muon beam for radiation damage campaign

Investigating the muon beam information is essential for radiation dose estimation, where the total number of muons and its distribution are mandatory parameters needed for GEANT4 simulation. These parameters are determined by both the proton beam arriving at target TgE and the CMBL configuration. The quantity of protons arriving at target TgE can be quantified by the proton beam current I_{p} measured just before the TgE. With constant CMBL configurations implemented during the

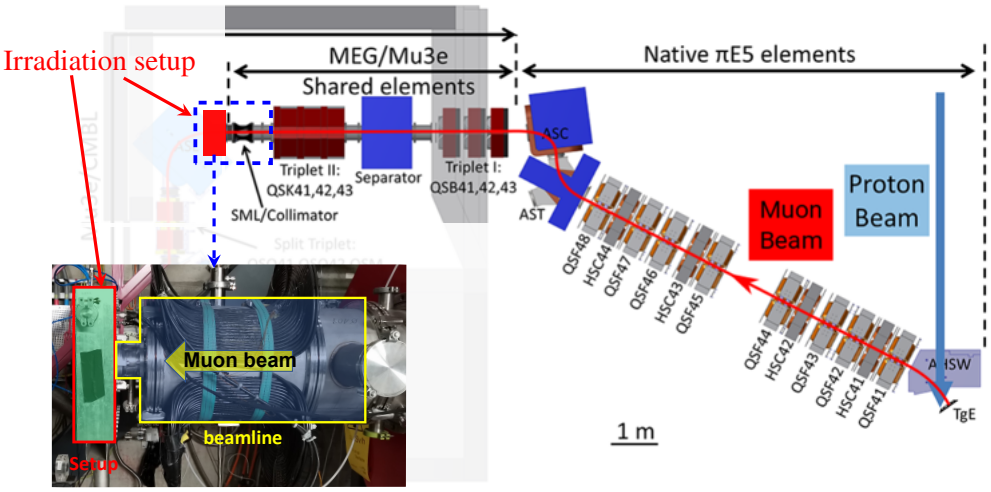

Figure 5.1: Overview of the muon beam facility and irradiation setup during the radiation damage campaign. Surface muons generated at target TgE are guided to the experimental area by the CMBL. The irradiation setup, positioned within an aluminum box (highlighted by a red rectangle on the left side of the figure), is mounted at the end of the beam pipe.

beam-test, a constant proton-to-muon ratio $\alpha_{p-\mu}$ and muon distribution $D_\mu(x, y)$ is expected, which can be determined by the calibration before the beam-test. The $x - y$ plane here is perpendicular to the direction of the muon beam z.

Proton beam current during radiation damage

The proton beam current I_p before hitting target TgE can be obtained from the HIPA control system, and it was logged for the entire test beam period. Figure 5.2 displays the effective proton beam current, which represents the current when the shutter of the πE5 beamline is in the "open" status, as well as its integral over time. The interruptions between the tests were caused by the shutdown of the HIPA facility, and a total current integral of 20.28 mADay was achieved in the test.

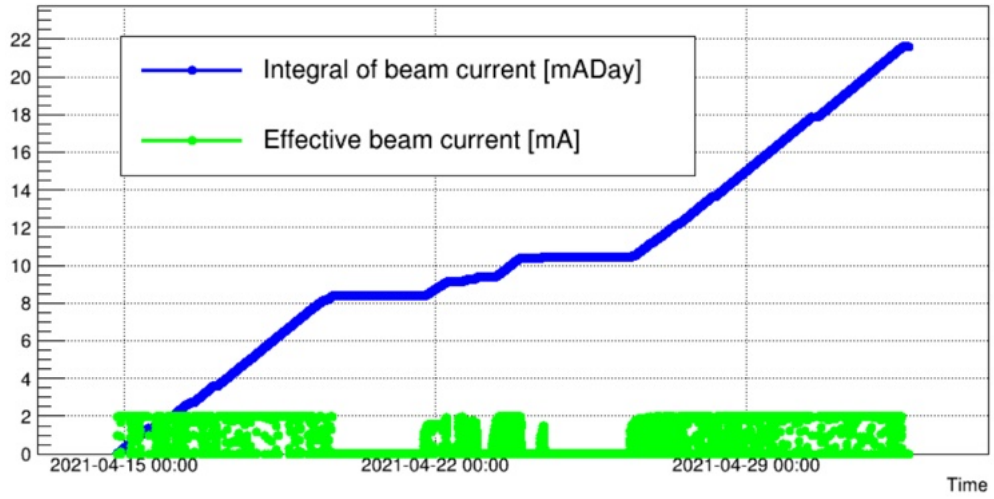

Figure 5.2: Effective proton beam current acquired during the test and its time-integrated value. The interruptions between the tests were caused by the shutdown of the HIPA facility.

Muon beam calibration

The CMBL was configured to a common setting, as detailed in Figure B.1. No configuration changes, except for the shutter status, were made until the end of the test. The constant muon beam distribution $D_\mu(x, y)$ and proton-to-muon ratio $\alpha_{p-\mu}$ were obtained from the muon beam calibration.

A 2D beam scanner [123] developed at PSI was utilized to calibrate the muon beam before and after the radiation campaign, just before the stopping target. Figure 5.3 illustrates the setup for muon beam calibration. The scanner is a sensor, composed of a Bicron BC418 scintillator and a Hamamatsu R7400U SiPM, mounted on PC-controlled x-y movable arms. Prior to the measurement, the x-y plane of the scanner was aligned to be perpendicular to the beam direction (z-direction) with the assistance of a laser collimation system. The beam rate was measured by a 2D scan with a 5-mm step along both x and y directions, while the proton beam current was recorded for the corresponding muon measurement point. As a result, $D_\mu(x, y)$ was obtained by dividing the rate at each point by its corresponding proton beam I_p. Additionally, the $\alpha_{p-\mu}$ was calculated by integrating the normalized beam rate in the x-y plane.

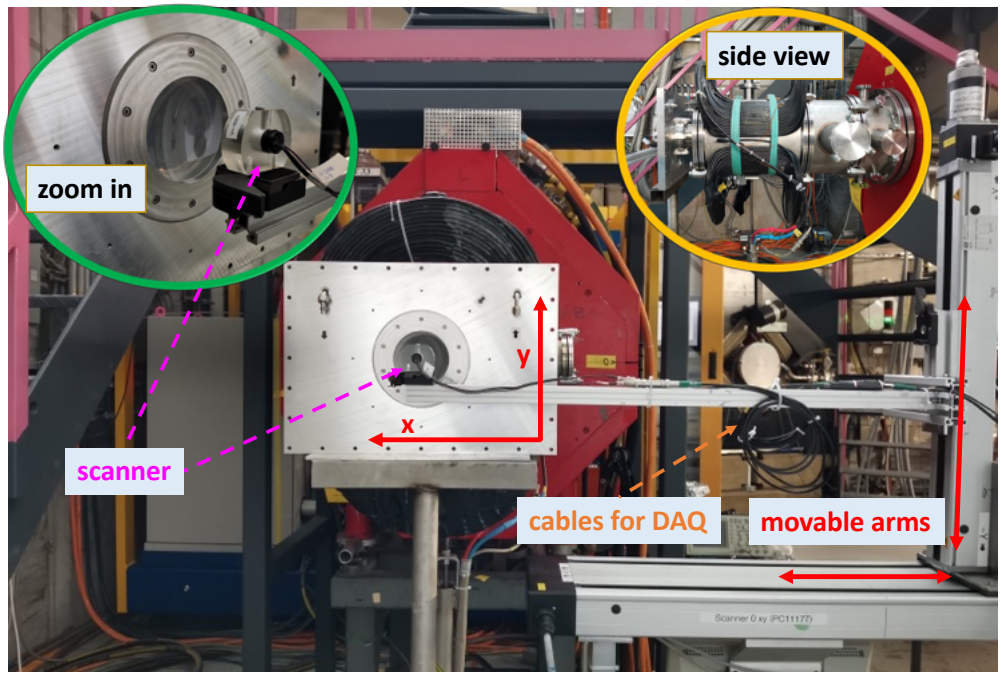

Figure 5.3: Muon beam profile measurement system. The muon beam data were obtained using a scanner mounted on x-y movable arms, while the proton beam current was read from the HIPA control system. The proton beam current can also be found in the web-based status page: http://gfa-status.web.psi.ch/hipa-info.html.

The result from the beam calibration can be seen on Figure 5.4 which shows the normalized muon beam profile in the range of ±60 mm (x-direction) and ±70 mm (y-direction), with Full Width at Half Maximum (FWHM) of around 40 mm along both x- and y-direction and a maximum value locates at around (5 mm, 5 mm) in the x-y plane. Moreover, the $\alpha_{p-\mu}$ obtained from the measured rate is 6.99×10^7 $\mu^+/s/mA$ which corresponding to a muon rate of 1.54×10^8 μ^+/s at I_p=2.2 mA.

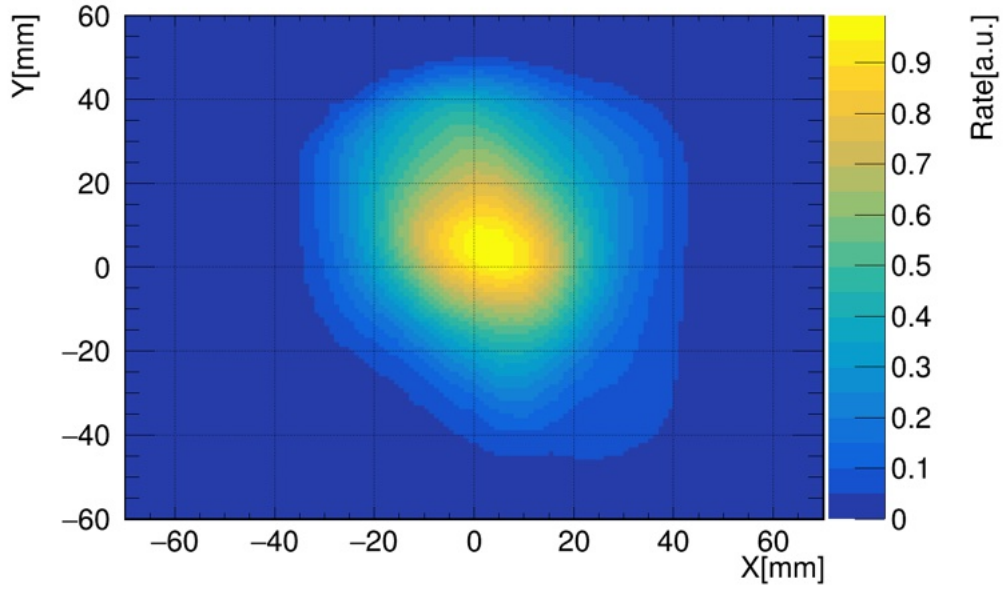

Figure 5.4: Normalized muon beam profile with respect to the maximum value. The coordinate system's origin aligns with the center of the beamline, indicating that the beam's center is shifted by (5 mm, 5 mm) towards the upper right from the beamline center. The beam profile exhibits a roughly double-Gaussian distribution.

5.1.2 Irradiation setup

Figure 5.5 displays the irradiation setup mounted on the πE5 beamline. A 2-mm-thick polyethylene plane was selected as the stopping target to halt the muons, and the Tile Detector samples, comprising 6 Mu3e Tile Matrices, was positioned directly behind the target. Each Matrix was individually connected to a PCB board, through which SiPMs were biased with a HV of 55 V to simulate the actual experiment's working conditions. Furthermore, dark current measurements were conducted during the radiation for indirect monitoring of radiation damage in SiPMs, which is expected to be proportional to the dark current. Figure 5.6a presents a schematic of the HV supply and current measurement. The six HVs were supplied by LEMO cables connected to the same feed-through board. Additionally, an amperemeter was used to measure the total current of all SiPMs on each Matrix, with individual matrix measurements taken via the switch circuit controlled by the programmable output signal from the Keithley 6487 power supply [124], which also provided the HV. To eliminate current contributions from room light, the aluminum box was light-tight.

The Aluminum box, including a *base* mounted on the beam pipe and a *cover* to close the setup, is helium tighted and dry helium gas flowed through the setup with slow speed to simulate the real Mu3e atmosphere. Furthermore, a constant temperature was provided by a water-cooled Aluminum block for smaller current measurement uncertainty, and the temperature on the center of the Matrix was read out by the I2C buses via the feed-through board (Figure 5.6b). The water temperature was set to 13 °C, which is a trade-off between surface condensation and annealing. In addition, the muon beam was aligned to the center of Matrix 3 to get a wider irradiation dose range.

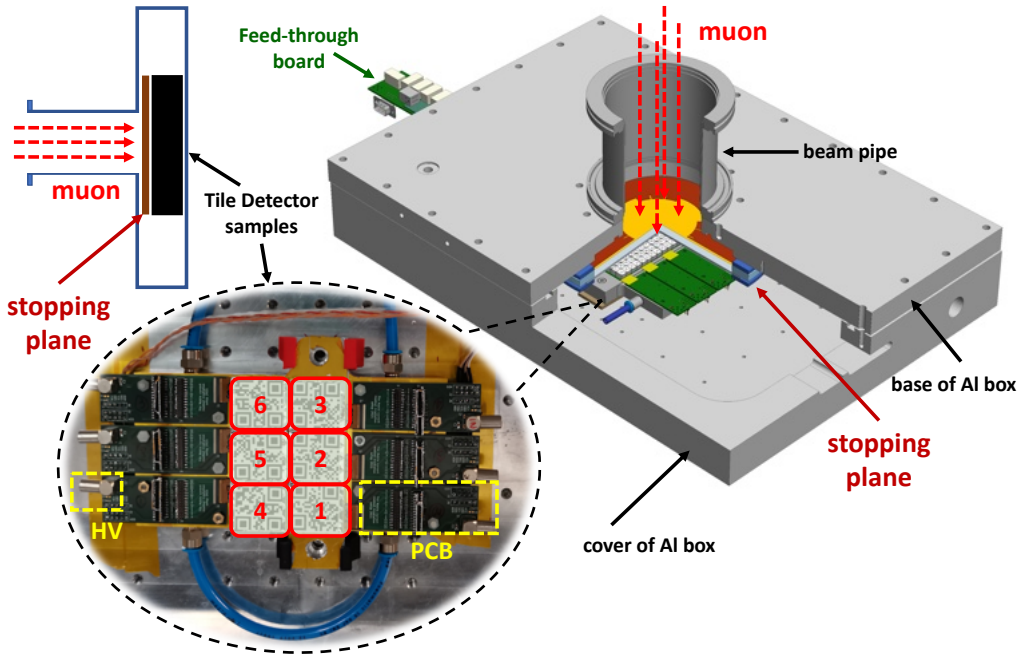

Figure 5.5: The irradiation damage setup. (Top-left) 2D schematic and (Top-right) 3D model. (Bottom-left) Photo of the Tile Detector samples, including 6 Mu3e Tile Matrices, each comprising a 4x4 SiPM array. The blue pipe supplied water to cool the aluminum block on which the six Matrices and PCB were mounted. Plastic spacers were used to minimize heat transfer between the block and the wall. The entire box was filled with a continuous flow of dry helium gas.

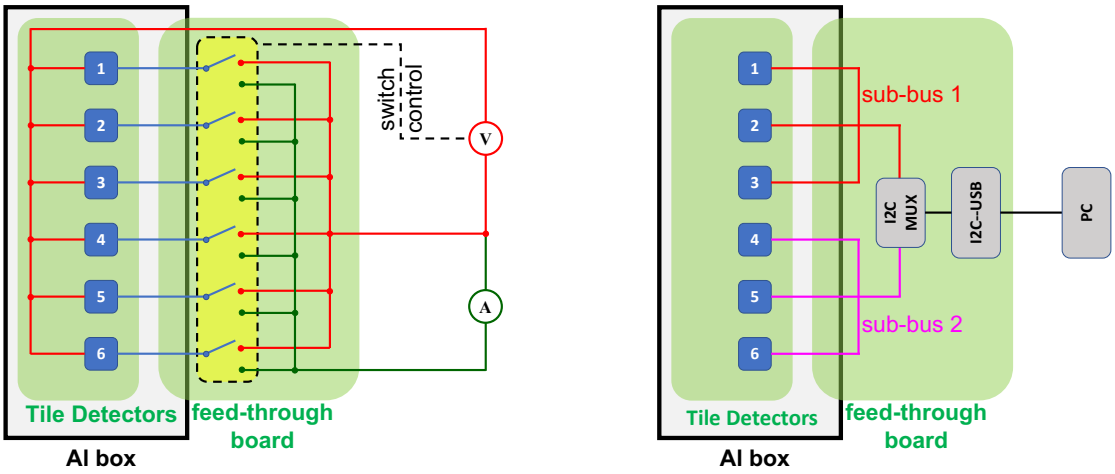

(a) HV supply and current monitor.

(b) Temperature monitor.

Figure 5.6: Schematic of HV connection and temperature monitoring for the irradiation damage beam-test setup. Matrix currents were read out sequentially, controlled by the programmable control signal from Keithley 6487. Six temperature sensors (TMP117) were read out through two I2C sub-buses using the multiplexer (MUX) TCA9548A.

5.2 Dose Estimation

The dose distribution $\Phi(x, y)$ in the SiPMs can be determined through GEANT4 simulation, using the muon number distribution $N_\mu(x, y)$ in the radiation test beam as input parameters:

$$\Phi(x, y) = f_{G4}(N_\mu(x, y)) = n_\mu \cdot f_{G4}(D_\mu(x, y)), \tag{5.1}$$

where n_μ represents the total number of muons arriving at the plane stopping target, and $f_{G4}(D_\mu(x, y))$ is the muon-to-dose response function, which indicates the equivalent dose contribution from a single muon.

Total muon number: n_μ

The total muon number can be estimated by the proton-to-muon ratio $\alpha_{p-\mu}$ and proton beam current $I_p(t)$:

$$n_\mu = \alpha_{p-\mu} \cdot \int_t I_p(t) \cdot dt. \tag{5.2}$$

A total muon number of $n_\mu \approx 1.23 \times 10^{14}$ μ^+ was obtained based on the muon beam calibration results:

$$\alpha_{p-\mu} = 6.99 \times 10^7 \ \mu/(\text{mA} \cdot \text{s})$$
$$\int_t I_p(t) \cdot dt = 20.28 \ \text{mA} \cdot \text{Day}.$$

Muon-to-dose response: $f_{G4}(D_\mu(x, y))$

The muon-to-dose response was acquired from the GEANT4 simulation, implemented based on the geometry of the measurement setup and the muon distribution $D_\mu(x, y)$ obtained during the beam-test campaign, as discussed in the previous sections. The same physics processes and dose calculation algorithm used in subsection 4.2.2 were implemented in this simulation to ensure comparable results. The radiation setup was modeled in GEANT4, including the 2 mm muon stopping plane, Tile Detector samples, cooling block, and the Aluminum box. The muon-stopping plane mounted on the aluminum base and the Tile Detector samples on the cover are shown in Figure 5.7, where their models are also depicted.

Moreover, a 2D muon source, a surface source in the $x - y$ plane, was implemented in the GEANT4 simulation, sampled from the interpolation of the measured discrete muon distribution. The relative position of the source distribution and the Tile Detector samples in $x - y$ coordinates is displayed in Figure 5.8. The muons were set to generate at a distance of $\Delta z = 5$ mm before the muon stopping plane in the simulation. The same muon energy spectrum used in subsection 4.2.2 was implemented, due to the lack of energy spectrum data from the beam calibration. However, this has no significant impact on the results because (a) the muon beam energy spectrum with the common CMBL configuration was well calibrated, which forms the basis of the energy spectrum used in subsection 4.2.2, and (b) the stopping plane is thick enough to stop all the muons, leading to zero kinetic energy before decay.

A 2D distribution of $f_{G4}(D_\mu(x, y))$, normalized to its maximum value, was obtained from the

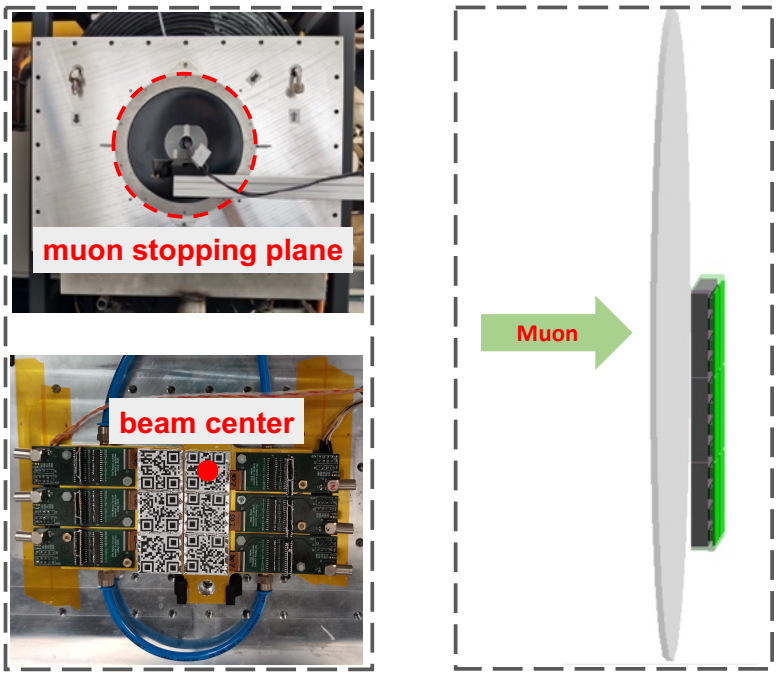

Figure 5.7: (left) Images and (right) 3D model of the muon stopping plane and Tile Detector samples in the radiation campaign. The muon stopping plane was attached to the base of the aluminum box, while the Tile Detector samples was mounted on the cover. The distance between the plane and the Tile Detector samples was just a few millimeters, as illustrated in the 3D model. The muon beam center was aligned with the center of the Matrix mounted in the top-right corner (Matrix 3).

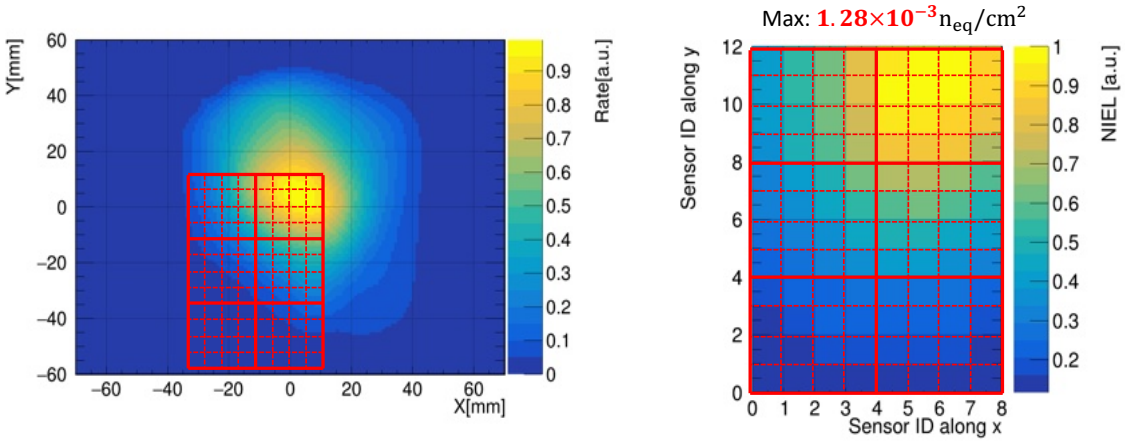

Figure 5.8: (left) The position of the Tile Detector samples relative to the beam profile; (right) Normalized dose distribution from the GEANT4 simulation. The small squares separated by dashed lines represent individual Tile Detector channels, and the large squares separated by solid lines represent the Matrices. The maximum values of both muon beam rate and radiation dose appear in the top-right corner, indicating that the simulation aligns with expectations.

simulation with over 10 million muons generated, as illustrated in Figure 5.8. The maximum muon-to-dose response in the SiPM obtained from the simulation is 1.28×10^{-3} n_{eq}/cm^2 per muon.

Thus, the NIEL dose in SiPMs $\Phi(x, y)$ obtained in the radiation beam-test follows the distribution of $f_{G4}(D_\mu(x, y))$ as shown in Figure 5.8, and the maximum dose reached in the beam-test is:

$$\Phi_{eq,max} = n_\mu \cdot f_{G4,max}(D_\mu(x, y)) = 1.57 \times 10^{11}\ n_{eq}/cm^2. \tag{5.3}$$

Moreover, the maximum dose obtained in the radiation damage campaign is around 70 % of the maximum dose expected at the end of the Mu3e phase I run and is already higher than 80 % of the SiPMs' full dose for phase I. Hence, the dose is high enough to study the radiation damage impacts on 80 % of the SiPMs used for the Mu3e phase I run and extrapolate the impacts on the full Mu3e Tile Detector.

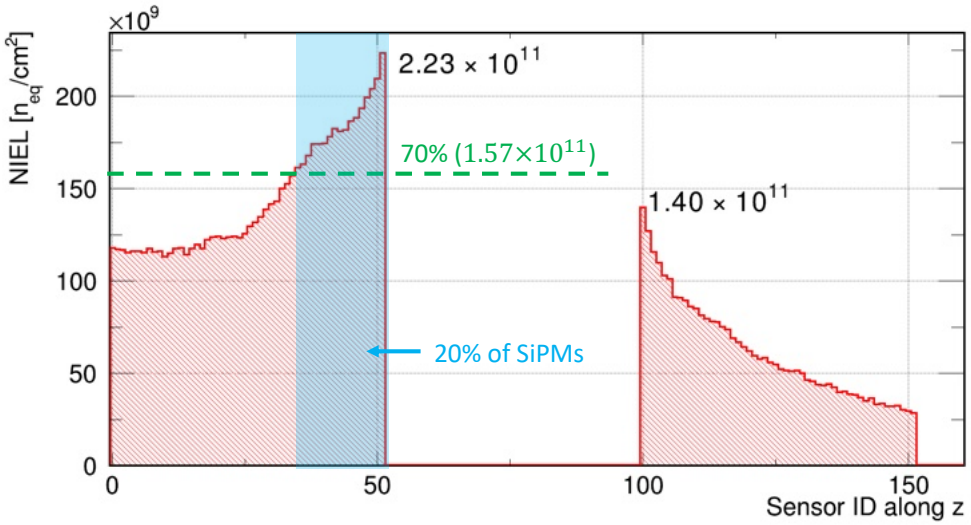

Figure 5.9: Comparison between the maximum dose reached in the beam-test campaign and the full Mu3e dose distribution in SiPMs. The maximum dose reached in the beam-test is around 70 % of the maximum dose expected in the full Mu3e experiment, and it is already higher than the maximum dose for 80 % of SiPMs.

After the radiation damage campaign, the SiPMs were comprehensively characterized in the lab, which will be presented in the next chapter.

Chapter 6

Sensor Characterization in the Laboratory

The irradiated Tile Detector SiPMs were examined using a variety of techniques to assess the impact of radiation-induced damage. Emission light imaging offers visualization of the damage distribution across the pixels, while Current-Voltage (IV) curve measurements evaluate the effect of damage on the SiPMs' electronic performance. Additionally, DCR estimation and temperature dependence measurements serve to characterize the influence of radiation on crucial parameters.

Furthermore, the noise produced by the irradiated SiPMs is thoroughly analyzed in the frequency domain (f-domain). A noise model, which accurately corresponds with the measurement, has been developed to characterize the SiPMs' noise. The potential sources of noise in different frequency ranges were also discussed, which is valuable for understanding the noise mechanisms and predicting performance. In addition, an annealing study was carried out to investigate the capacity for defect restoration at various temperatures. This comprehensive analysis offers essential insights into the effects of radiation damage on SiPMs and informs strategies for optimizing their performance in the Tile Detector.

6.1 Defects Characterization

This section focuses on the characterization of defects in SiPMs, which is critical to understanding their performance and reliability. Through various measurements and analyses, we will investigate the impact of radiation damage on SiPM properties, such as dark current and breakdown voltage, and explore the relationship between these properties and temperature.

6.1.1 Visualization of radiation damage defects

The avalanche process in a SiPM biased above its breakdown voltage can generate optical or infrared (IR) light with a photon emission probability of 3×10^{-5} per charge carrier [125, 126]. Since defects centers will trigger more avalanche processes, utilizing an imaging technique to visualize the photons emitted from a SiPM provides an efficient approach for identifying the distribution of these defects within the device. A self-built microscope-based camera setup is employed to capture light emitted from the SiPM when biased above its breakdown voltage.

The setup, illustrated in Figure 6.1, comprises an adjustable optical path constructed with commercial components, including a 50/50 optical splitter, a mirror, collimators, and lenses. These components

were mounted on an aluminum base assembled from two planes, and the entire setup was housed in a dark box to eliminate interference from ambient light.

A Starlight Xpress SXVR-H18 camera, known for its low noise, was utilized for capturing the images. To minimize noise from the camera sensor, the camera's cooling setting was configured to −15 °C, achieved using the camera's built-in two-stage thermoelectric cooler together with a cooler made from an aluminum block cooled with 5 °C liquid Kry30 [127]. The SiPM was also cooled with the same liquid loop to avoid overheating by the dark current.

A 10x objective lens, mounted on a remote-controlled movable arm, was employed to image the SiPM's microstructure in detail, enabling the differentiation of individual pixels while including a considerable number of pixels within the scope of observation. Furthermore, a light-emitting diode (LED) served as an external light source for setup calibration, with the LED branch wrapped in black foil to prevent light interference with the camera.

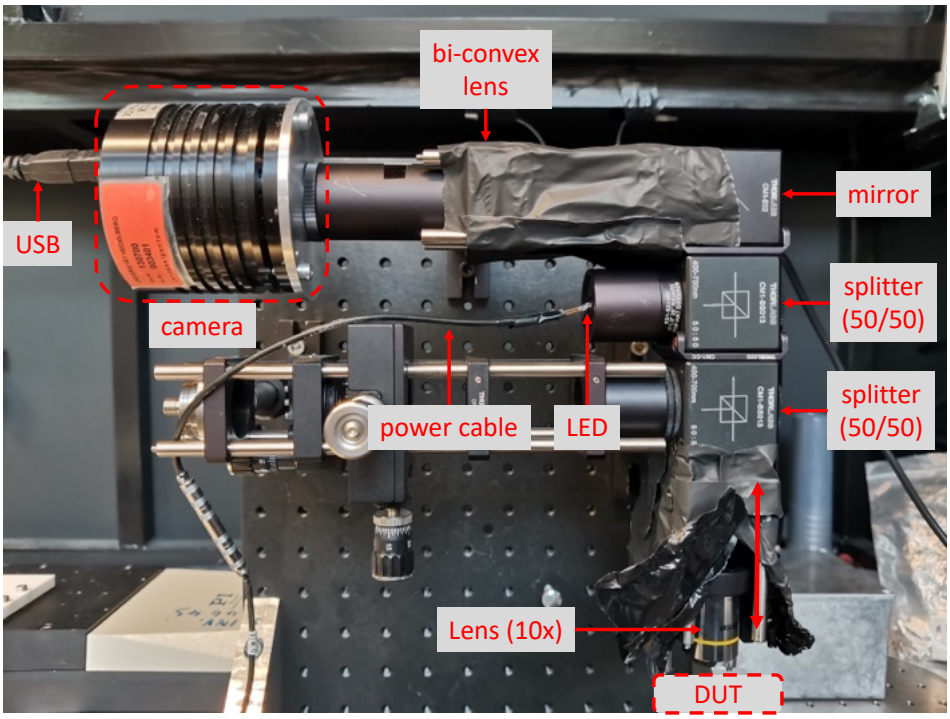

Figure 6.1: Microscope-based camera system for defect visualization. Key components from Thorlabs are indicated: bi-convex lens (LB1676-B), mirror (CM1-E02), 50/50 beamsplitter (CM1-BS013), and diffuser (ED1-S20-MD). The objective lens is an Olympus 10x microscope objective lens, and the camera is Starlight Xpress SXVR-H18.

Setup calibration

The camera system was calibrated before each measurement. Figure 6.2a presents the schematic for the focus calibration to ensure it focused on the SiPM surface. In this configuration, the SiPM was not biased and was illuminated by the LED light instead. The setup was adjusted until the best image clarity was achieved, with the key parameter being the distance between the objective lens and the SiPM surface. The camera exposure time depended on the LED luminance and was typically set to

around 0.1 s, which was fast compared to the time required to measure photon emission from the SiPM. Figure 6.2b shows an image captured with the best-clarity configuration, where the 50×50 µm^2 SiPM pixels can be clearly distinguished, indicating the ability to differentiate photons emitted from different pixels during measurements.

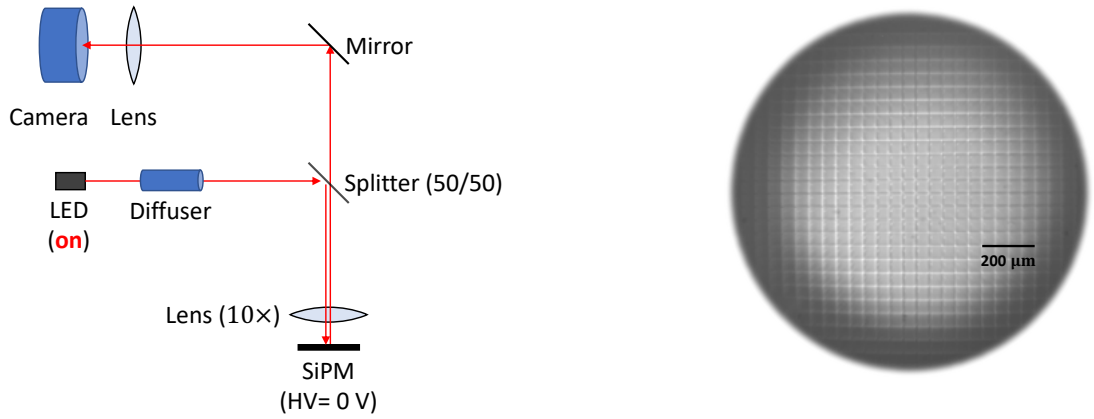

(a) Schematic of calibration setup.

(b) Image of SiPM surface with LED on.

Figure 6.2: Imaging system calibration. A clear image was obtained after adjusting LED voltage and exposure time to avoid overexposure and underexposure. The exposure time was set to $O(0.1)$ s.

Additionally, the camera sensor's noise calibration was conducted in a dark environment with the LED off. A lengthy exposure time of 30 minutes ensured sufficient noise collection. Figure 6.3 presents a noise image example measured, exhibiting random hotspots distributed across the frame. Each hotspot corresponds to an individual camera pixel, aligning with the established understanding of camera sensor noise as randomly distributed and uncorrelated with adjacent pixels. The calibration shows that the noise of the camera is sufficiently low for the SiPM avalanche photon imaging with the cooling system. The noise obtained from each calibration was employed for noise extraction in the measured avalanche photon image.

Photon emission measurement

After calibration, the photon emission from the SiPM was measured with a reverse bias voltage of 58 V, as shown in Figure 6.4a. The exposure time was set to 30 minutes to ensure sufficient photon collection. Figure 6.4b presents the result with the camera's intrinsic noise removed. The pixels can be clearly distinguished due to the absence of photon emission between pixels. Moreover, the uniform distribution of photons suggests a uniform distribution of defects in the SiPM. This is likely attributable to the low probability of positrons producing cluster or multiple cluster defects, which are the main defects caused by strong interactions. Emission light from non-irradiated SiPMs was also measured, but no distinct light source from the SiPM surface was observed due to the low light emission.

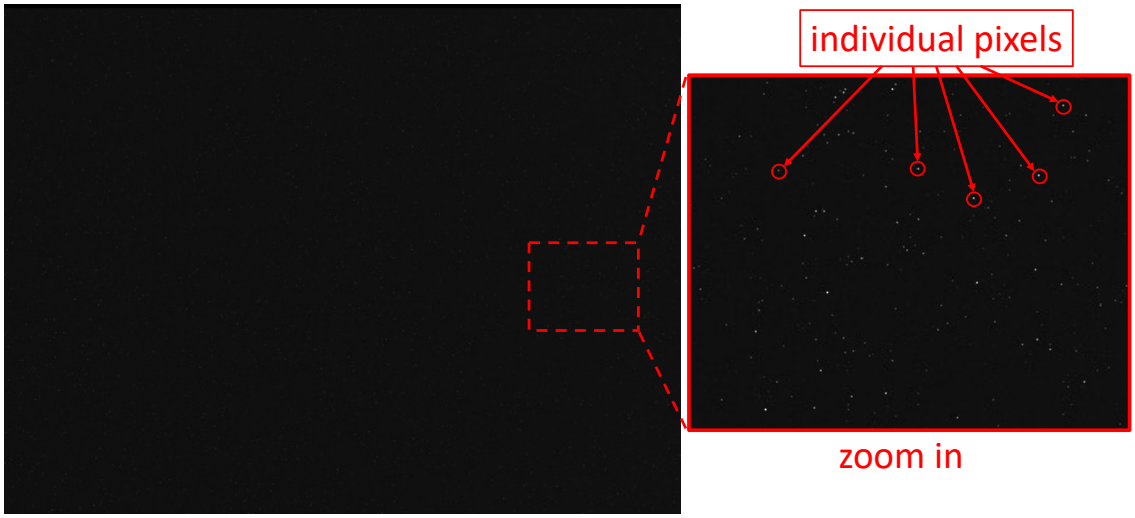

Figure 6.3: Example of measured intrinsic noise from the camera sensor. The noise level is adequately low, ensuring that it does not impact SiPM avalanche light imaging.

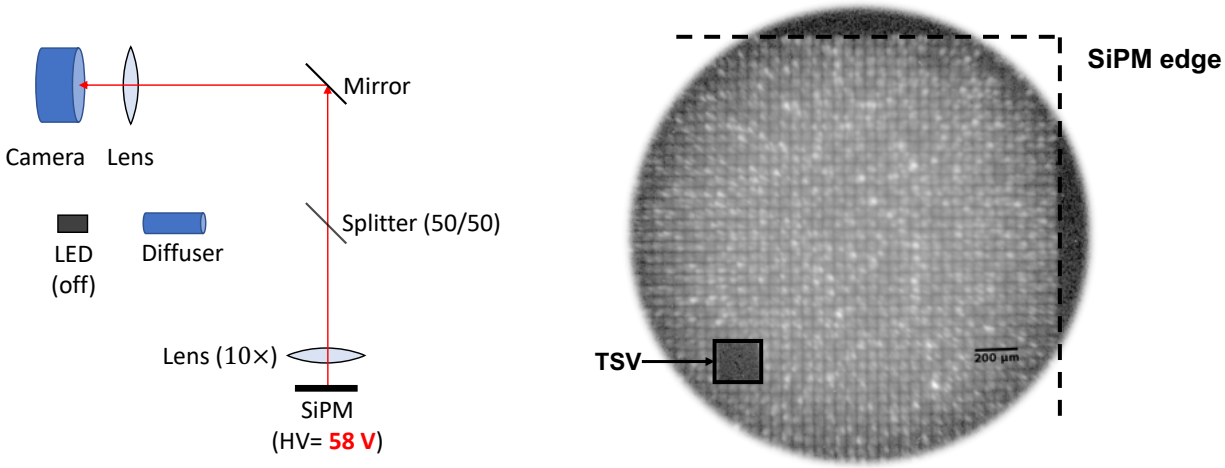

(a) Schematic of setup.

(b) Avalanche light image.

Figure 6.4: Imaging light from the biased SiPM. (a) The setup for light imaging from avalanche in SiPMs, with the LED branch turned off and a 58 V high voltage applied to bias the SiPM. (b) the avalanche light image from SiPM with a radiation dose of approximately 1.5×10^{11} n_{eq}/cm^2 with exposure time of 30 minutes. Through-Silicon Via (TSV) is at the SiPM's center where no photon is emitted.

6.1.2 Current-voltage curve measurement

Measuring the IV curve is another common method for investigating the effects of radiation on important SiPM parameters, such as the breakdown voltage V_{br} and the dark current I_d above V_{br}, which are significant for SiPM operation and performance.

As shown in Figure 6.5, a specific setup was constructed for the IV curve scan of SiPMs. The Matrix under test was connected to a specially designed PCB, where a dual-row connector enabled the connection of individual SiPMs to the measurement circuit by shorting the corresponding pin pair with

a jumper. Both current measurement and SiPM bias were supplied by the Keithley 6487 [124], which could be programmed to scan the supply voltage in a given voltage range (V_{min} to V_{max}) and step (ΔV), as well as a time delay (t_{delay}) between two measurement points. Moreover, the corresponding current at each HV point was read back automatically.

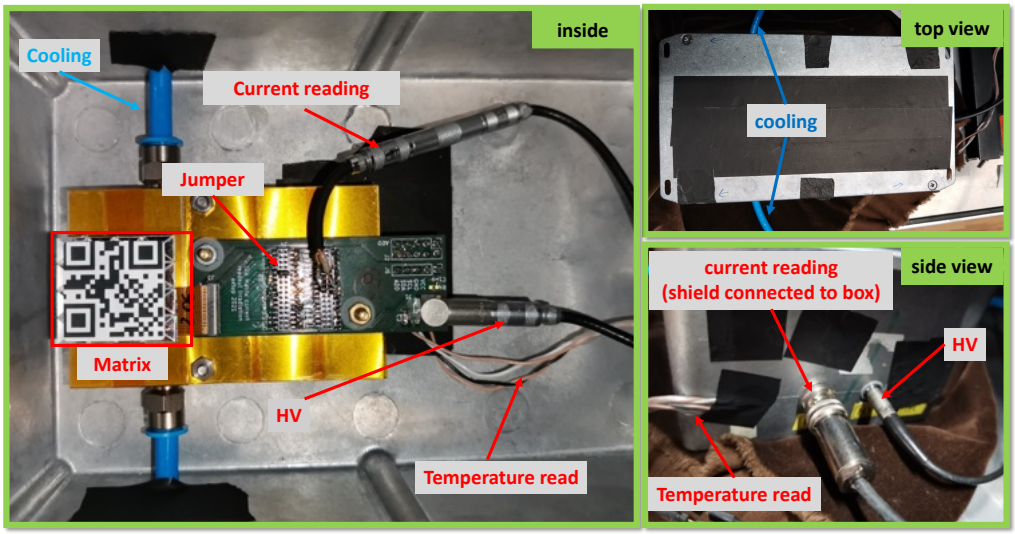

(a) Pictures of setup.

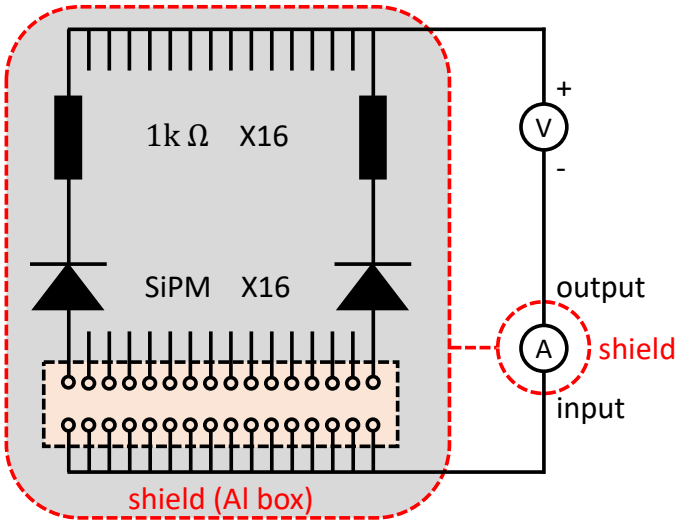

(b) Schematic of setup.

Figure 6.5: I-V curve measurement setup. The setup is housed in an aluminum box, also serving as a noise shield. The current measurement cable connects to the amperemeter via a triax connector, with "input", "output," and "shield" lines connected. Each SiPM can be individually connected to the measurement circuit by attaching a jumper to short the corresponding pin pair in the dual-row connector.

The current of the SiPM is highly sensitive to the working temperature. Therefore, a liquid-cooled aluminum block, in tight contact with the Matrix thermal pad, was employed to stabilize the temperature, effectively suppressing the self-heating of the radiated SiPM. The liquid temperature was set to about 10 °C to avoid condensation, and the temperature was monitored by the temperature sensor mounted on the center of the Matrix temperature reading out per second. Figure 6.6a shows a temperature example

during an IV scan, where SiPM self-heating was observed. Moreover, Figure 6.6b presents the averaged temperature of all the Matrices, which is around 11.38 °C.

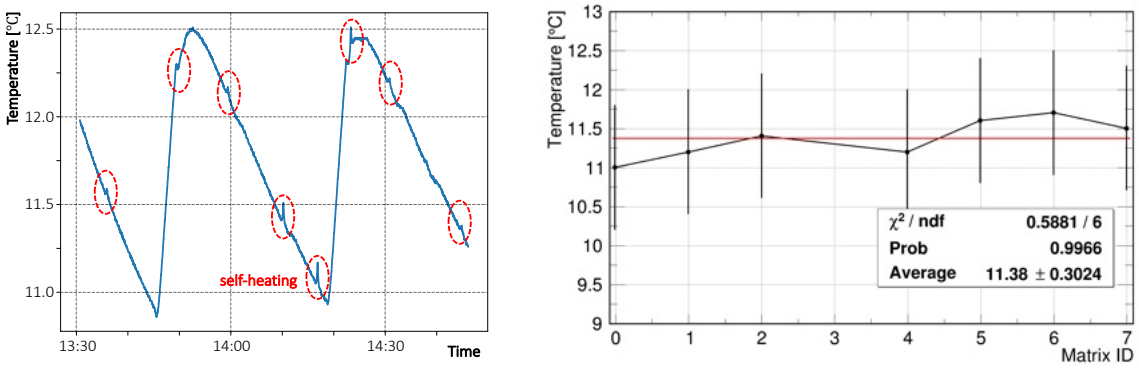

(a) Temperature of IV scan for single Matrix.

(b) Averaged temperature for all Matrices' IV scan.

Figure 6.6: Temperature monitoring during IV scan. (a) The temperature cycle, with a period of approximately 35 minutes, results from the chiller's cooling cycle. Red circles show SiPM self-heating, where temperature changes primarily depend on the SiPM's heat production and its distance to the temperature sensor. (b) The error bar assigned to each data point represents the maximum temperature difference resulting from the heating and cooling cycle of the chiller. Matrix 3's temperature sensor is broken, but it is cooled by the liquid with the same temperature. Matrices 0 and 7, non-irradiated, serve as references.

Additionally, the full setup was installed in an aluminum box for better optical and electrical isolation. The setup was measured in a larger black box to ensure no extra current originated from external light sources. Furthermore, the aluminum box was connected to the "shield" pin of the Keithley 6487 to provide effective electrical noise shielding, ensuring a small measurement uncertainty for ultra-low current.

Forward current measurement

The settings for the forward IV scan are given in Table 6.1. Figure 6.7 shows an example of a forward IV curve from a SiPM. The knee voltage V_k and quenching resistor R_q can be obtained by fitting the forward current curve in [−3 V,−1 V] with

$$I = \frac{(V + V_\mathrm{k})}{R_0 + \frac{R_\mathrm{q}+R_\mathrm{s}}{N_\mathrm{pixel}}} \approx \frac{(V + V_\mathrm{k})}{R_0 + \frac{R_\mathrm{q}}{N_\mathrm{pixel}}}, \tag{6.1}$$

where $R_0 = 1\,\mathrm{k\Omega}$ is the protection resistor, $N_\mathrm{pixel} = 3584$ is the total number of pixels in a single SiPM, and R_s is the series resistance of a pixel that fulfills $R_\mathrm{s} \ll R_\mathrm{q}$. It should be noted that the sign the voltage is negative to maintain consistency with the sign used in the Tile Detector HV.

The V_k obtained from different SiPMs is plotted along radiation dose, as shown in Figure 6.8a. The averaged V_k around 607 mV for the non-irradiated SiPMs ($\Phi_\mathrm{eq} = 0$), and it slowly drops by around 10 mV when the dose increased to the maximum dose reached in the radiation beam-test. However, the drop, with a relative difference smaller than 2 %, will not affect the electronic performance of the SiPM and can be ignored.

Table 6.1: Parameters for forward IV curve scan.

Parameter	Value
V_{min} [V]	0
V_{max} [V]	-3
ΔV [V]	-0.1
t_{delay} [s]	0.5

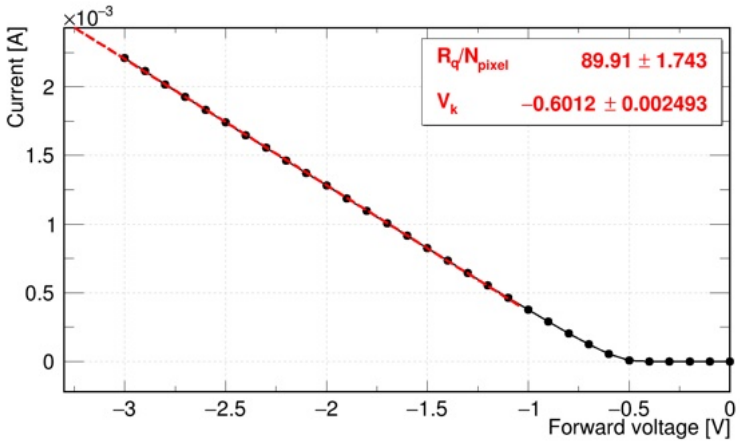

Figure 6.7: Forward IV curve example with linear fitting in range of (−3 V,−1 V).

The obtained R_{q} is given in Figure 6.8b. No significant change was found either, with R_{q} remaining constant with an average value of 313 kΩ and the largest error smaller than 10 %. Therefore, no significant impact on the quenching resistor was observed in the radiated SiPMs as well.

Reverse current measurement

The setting for the reverse IV scan is given in Table 6.2. The IV curve examples from SiPMs with different exposure doses are shown in Figure 6.9, and the IV curve from a non-irradiated SiPM is also given in the plot as a reference. In addition, the HV in the plot is the bias voltage direct on SiPM with voltage drop on protect-resistor corrected, and if not specified, all the HV values from here on indicate the direct bias voltage on SiPM.

Table 6.2: Parameters for reverse IV curve scan.

Parameter	Value
V_{min} [V]	0
V_{max} [V]	+58
ΔV [V]	+0.2
t_{delay} [s]	0.5

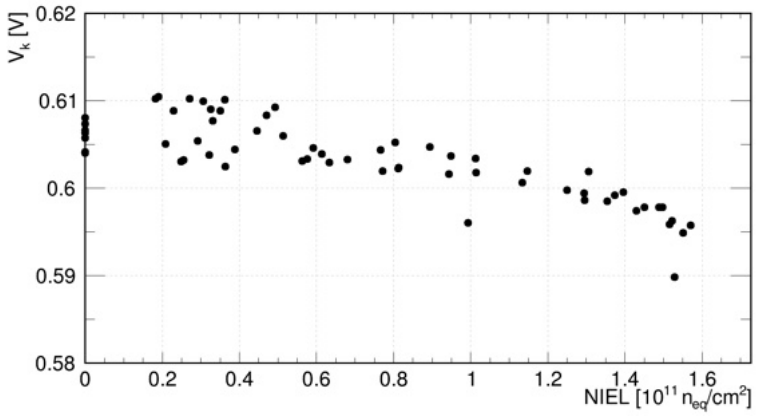

(a) Parameter V_k.

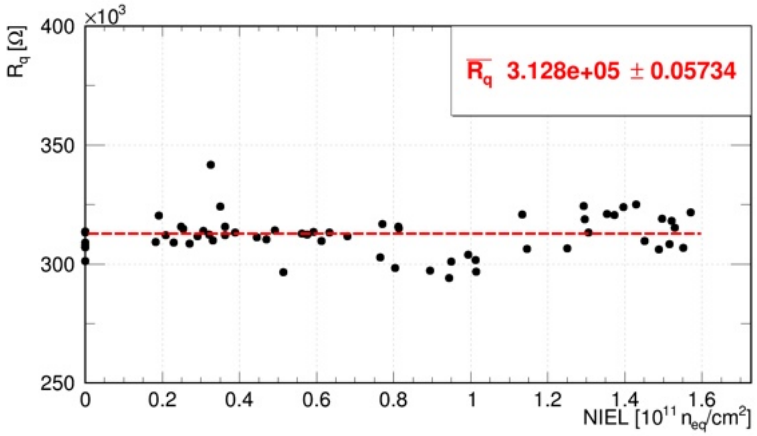

(b) Parameter R_q.

Figure 6.8: Parameters derived from forward IV curve for various SiPMs. (a) V_k slowly declines from 607 mV by around 10 mV as dose increases due to the self-heating increase in irradiated SiPMs. (b) No dose-dependence in R_q is observed.

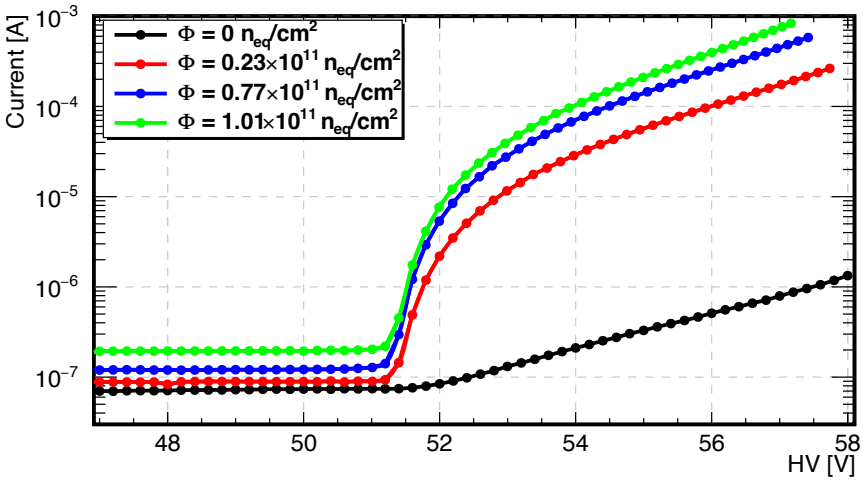

Figure 6.9: Reverse IV curve of SiPMs with differing exposure doses. The HV on the x-axis represents the direct bias voltage on the SiPM.

Breakdown voltage The breakdown voltage V_{br} can be obtained from the reverse IV curve by various methods. In this work, a method based on the 3rd derivative of SiPM's reverse current [128] was applied to get the V_{br}. The method is based on a Direct Current (DC) model which describes the breakdown phenomenon by distinct avalanche turn-on (V_{01}) and turn-off (V_{10}) voltages, predicting that the 3rd derivative of the reverse current curve follows:

$$\frac{\mathrm{d}^3 I}{\mathrm{d}V^3} = A_{3\text{rd}} \cdot [2 - \frac{h}{\sigma^2}(V - V_{01})] \cdot e^{-\frac{(V-V_{01})^2}{2\sigma^2}}, \tag{6.2}$$

where the parameters are turn-on voltage (V_{01}), its standard deviation (σ), amplitude of 3rd derivative ($A_{3\text{rd}}$), and hysteresis between turn-on and turn-off voltage ($h = V_{01} - V_{10}$). Figure 6.10 shows an example of the 3rd derivative of the measured reverse IV curve [1] and its fitting result with Equation 6.2.

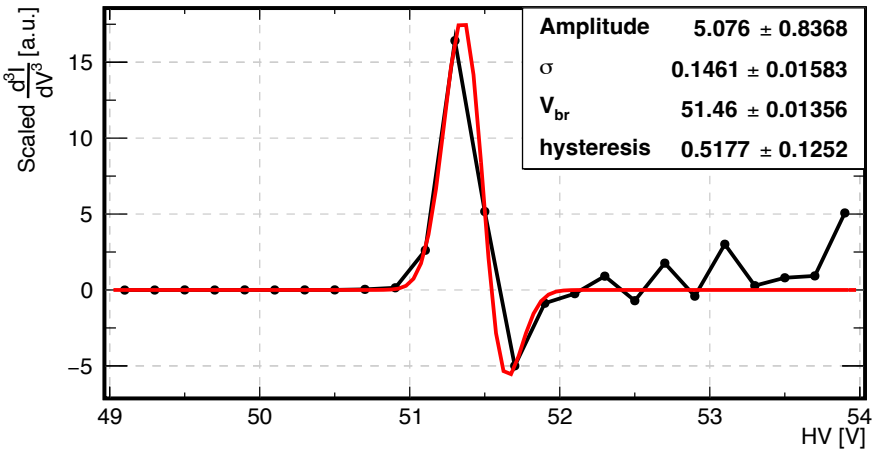

Figure 6.10: 3rd derivative of reverse IV curve and its fitting result using Equation 6.2. The discrete derivative is determined by the slope of adjacent points. V_{br} in the parameter pad corresponds to the turn-on voltage V_{01} in Equation 6.2.

Figure 6.11 illustrates the parameters obtained from SiPMs exposed to dose up to $1.57\times10^{11}\,\text{n}_{\text{eq}}/\text{cm}^2$. The V_{01} is plotted along different doses, where no clear dependency on dose was found. Therefore, the breakdown voltage in the Tile Detector SiPM will not be strongly impacted by the radiation damage from the Mu3e positron with a dose up to $1.57 \times 10^{11}\ \text{n}_{\text{eq}}/\text{cm}^2$. In addition, the averaged turn-on voltage V_{01} of 51.44 V was obtained with a standard deviation σ of 0.15 V (Gaussian distribution). With $h = 0.45$ V, the turn-off voltage $V_{10} = V_{01} - h = 50.99$ V. Moreover, a breakdown voltage $V_{\text{br}} = 51.24$ V at $T = 11.38\,°\text{C}$ was obtained based on the data provide by Hamamatsu, which verifies that the measured breakdown voltage should be between V_{01} and V_{10} or close to either one of them[128].

It was found that the uncertainty of the parameters is still quite large, which can be improved by smaller voltage steps in the IV scan. However, the voltage step length must compromise for test time

[1] Method used to calculate discrete IV curve derivative:
$I'(V + 0.5\Delta V) = \frac{I(V+\Delta V)-I(V)}{\Delta V}$,
$I''(V) = \frac{I'(V+0.5\Delta V)-I'(V-0.5\Delta V)}{\Delta V}$,
and $I'''(V + 0.5\Delta V) = \frac{I''(V+\Delta V)-I''(V)}{\Delta V}$,
where the ΔV is the voltage step used in the reverse IV scan.

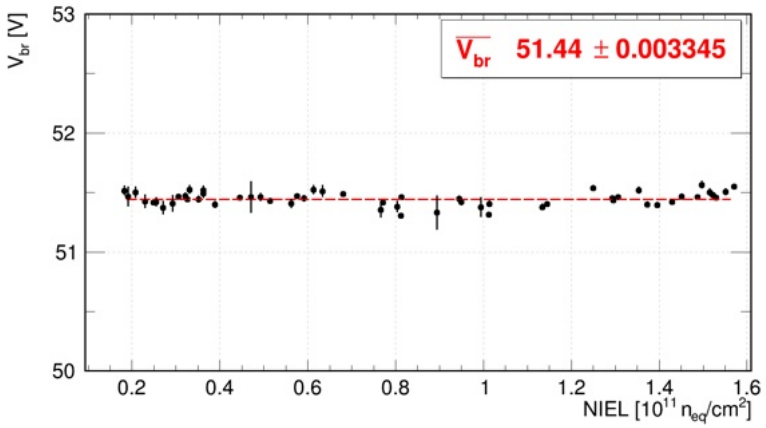

(a) Parameter V_{01}.

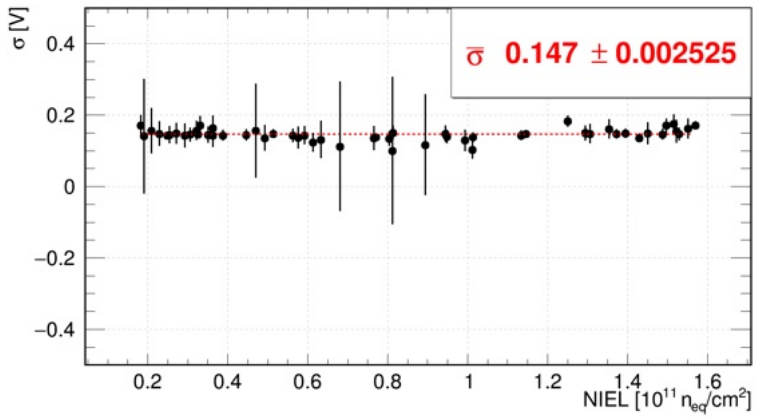

(b) Parameter σ.

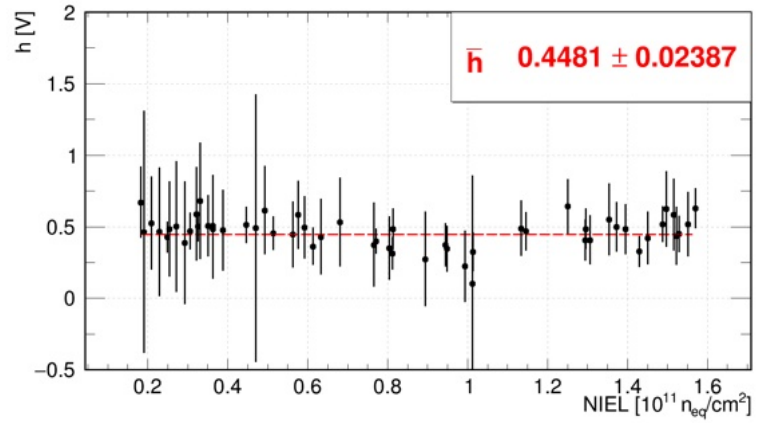

(c) Parameter h.

Figure 6.11: Parameters of Equation 6.2 acquired from SiPMs with different exposure doses. The results suggest that all the parameters are dose-independent.

to avoid annealing effects for later measurements in this work. Even though, the results are effective to conclude that the breakdown voltage was not impacted in the measured exposure dose range.

Dark current above V_{br} The dark current above the breakdown voltage is another useful parameter for characterizing radiation damage in SiPMs. With a constant $V_{ov} = 3.7\,V$ on SiPMs, the dark current was plotted along the corresponding exposure dose, as shown in Figure 6.12. The dark current is supposed to be proportional to the radiation dose. Therefore, a linear function was employed for fitting, and a good match between the data and the fitting function verified the linear relationship between the dark current and dose. Moreover, the slope obtained from the fitting indicates that the dark current increases by 0.21 mA when the dose increases by 10^{11} n_{eq}/cm^2.

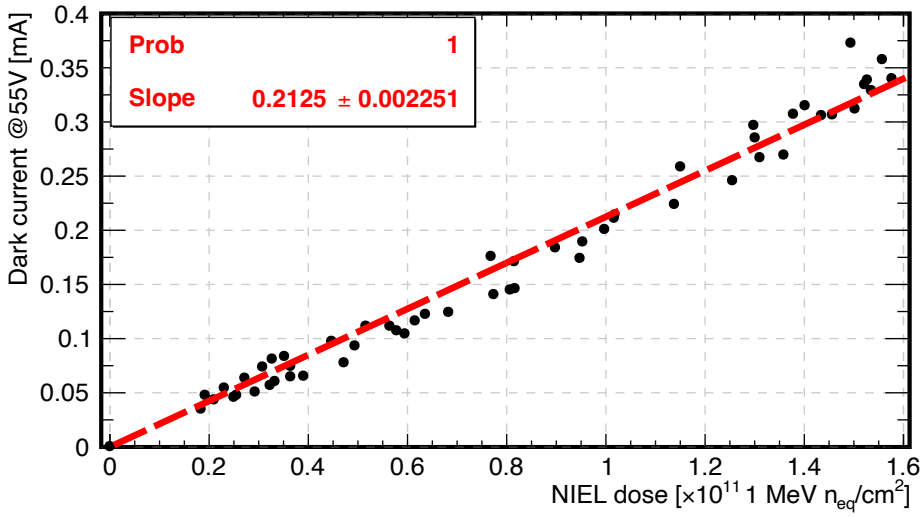

Figure 6.12: Dark current with $V_{ov} = 3.7\,V$ for SiPMs with different exposure doses. The calibration of hundreds of non-irradiated SiPMs exhibited good uniformity in dark current, effectively ruling out any influence from performance differences among individual SiPMs. As anticipated, the dark current above V_{br} is proportional to the radiation dose. With $T = 11.38\,°C$ and $V_{ov} = 3.7\,V$, the obtained coefficient is 0.21 n_{eq}/cm^2.

The slope of the data above 1.4×10^{11} n_{eq}/cm^2, mainly from Matrix 3 where the temperature is not monitored, is slightly higher than the slope at low dose. The reason may be that the stronger self-heating in the SiPM leads to a higher temperature in the SiPM, resulting in bigger current.

6.1.3 Dark count rate estimation

The DCR is not only an important parameter to characterize the irradiated SiPM but also a fundamental parameter for SiPM response simulation. However, direct measurements, such as single pulse counting or time delay between adjacent events, are impossible for the irradiated SiPM due to the loss of the single photon detection capability. Three different methods were employed for the DCR estimation based on the DC information.

Method 1:

The current of SiPM's single-event can be modeled by

$$i(t) = \begin{cases} i_0 \cdot e^{-\frac{t}{\tau_{\text{decay}}}} \cdot (1 - e^{-\frac{t}{\tau_{\text{rise}}}}) & \text{if } t > 0, \\ 0 & \text{else,} \end{cases} \tag{6.3}$$

where i_0 is the peak current and $\tau_{\text{decay/rise}}$ are the decay/rise time of the response. Since $\tau_{\text{rise}} \ll \tau_{\text{decay}}$, $i(t)$ can be simplified to

$$i(t) = i_0 \cdot e^{-\frac{t}{\tau_{\text{decay}}}} \quad (t > 0). \tag{6.4}$$

For the SiPM with DCR r_{d}, the number of dark events in the time interval $\text{d}\tau$ is supposed to follow a Poisson distribution with a mean value

$$\text{d}N = r_{\text{d}} \cdot \text{d}\tau. \tag{6.5}$$

Thus, the averaged current $\text{d}\bar{I}_{\text{d}}$ in $d\tau$ contributed from the dark events' response is given by

$$\text{d}\bar{I}_{\text{d}} = \text{d}N \cdot i(t - \tau) = r_{\text{d}} i_0 \cdot e^{-\frac{t-\tau}{\tau_{\text{decay}}}} \text{d}\tau \quad (t > 0). \tag{6.6}$$

Since the occurrence of dark events in different time intervals are statistically independent, the dark current I_{d} is the integral of Equation 6.6:

$$I_{\text{d}} = r_{\text{d}} i_0 \cdot \int_0^{\infty} e^{-\frac{t-\tau}{\tau_{\text{decay}}}} \text{d}\tau = r_{\text{d}} \cdot i_0 \cdot \tau_{\text{decay}}. \tag{6.7}$$

Consequently, the dark count rate r_{d} of a SiPM is given by

$$r_{\text{d}} = \frac{I_{\text{d}}}{i_0 \cdot \tau_{\text{decay}}}. \tag{6.8}$$

Since the single-event current peak and decay time measured from the non-irradiated SiPMs are $i_0 = 11.64\,\mu\text{A}$ and $\tau_{\text{decay}} = 30\,\text{ns}$ and the dose coefficient is $0.21\,\text{mA}/(10^{11}\,\text{n}_{\text{eq}}/\text{cm}^2)$, r_{d} can be written as a function of radiation dose Φ_{eq}:

$$r_{\text{d}}[\text{GHz}] = \frac{0.21\,\text{mA}}{11.64\,\mu\text{A} \cdot 30\,\text{ns}} \cdot \Phi_{\text{eq}}[10^{11}\,\text{n}_{\text{eq}}/\text{cm}^2] = 0.602 \cdot \Phi_{\text{eq}}[10^{11}\,\text{n}_{\text{eq}}/\text{cm}^2]. \tag{6.9}$$

Therefore, the DCR estimation for all the SiPMs at end of phase-I run follows the same distribution of the dose, as shown in Figure 4.11, with the maximum DCR of 1.34 GHz.

Method 2 and 3:

For comparison, the DCR was also estimated by the dark current with two additional methods [129]:

$$r_{\text{d1}} = \frac{I_{\text{d}}}{q_{\text{e}} G_{\text{c}}} \tag{6.10}$$

and

$$r_{d2} = \frac{I_d}{I_{d0}} \cdot r_{d0}. \tag{6.11}$$

The term q_e in Equation 6.10 is the elementary electron charge and G_c is the *Current Gain* which is not significantly impacted by the radiation damage within the Mu3e dose range. The I_{d0} and r_{d0} in Equation 6.11 are the dark current and DCR measured from the non-irradiated SiPMs. Table 6.3 gives the parameters used in the calculation and results are listed in Table 6.4. The DCR estimated from different methods agrees with each other quit well with the biggest difference smaller than 6 %.

Table 6.3: Parameters for DCR calculation. With the assumption that no strong pile-up in the same pixel, G_c is replaced by the gain given in the datasheet. I_{d0} and r_{d0} are the dark current and dark rate without radiation, which are carefully measured with in 32 Tile Detector SiPMs.

Parameter	Value
G_c	1.72×10^6
I_{d0} [nA]	94.42
r_{d0} [kHz]	289.37

Table 6.4: DCR estimated from different methods. The $I_d = 0.33$ mA corresponds to the radiation dose reached in the beam-test and $I_d = 0.47$ mA for the maximum dose reached in the Tile Detector SiPM at end of Phase I run. The V_{ov} is 3.7 V with temperature of 11.38 °C.

Different methods	DCR [GHz] ($I_d = 0.33$ mA)	DCR [GHz] ($I_d = 0.47$ mA)
Equation 6.8	0.95	1.34
Equation 6.10	0.97	1.39
Equation 6.11	1.01	1.44

6.1.4 Temperature dependency

The setup shown in Figure 6.13 was used to measure the SiPM temperature dependency. The same current measuring setting used in subsection 6.1.2 was employed in this measurement.

Improved thermal insulation was implemented to achieve lower setup temperatures. The aluminum box was installed in a thermal box instead of the standard black box for IV scan measurement, and the full setup was covered by four layers of black Polyurethane-Coated Nylon fabric for room light block-out. The aluminum surface was covered by one layer of thermal insulation material, and it was set on two plastic spacers to minimize direct connection to the thermal box, as shown in Figure 6.13b. Furthermore, the liquid cooling loop was also insulated by the insulation material.

The lowest temperature of −15 °C on the Matrix was reached with liquid cooling at a temperature of −35 °C, which is the lowest liquid temperature the chiller can provide. The temperature for Matrix 6 in different runs is shown in Figure 6.14 as example. Moreover, the SiPM closest to the temperature sensor was measured to ensure the monitored temperature closely matched the true temperature in the

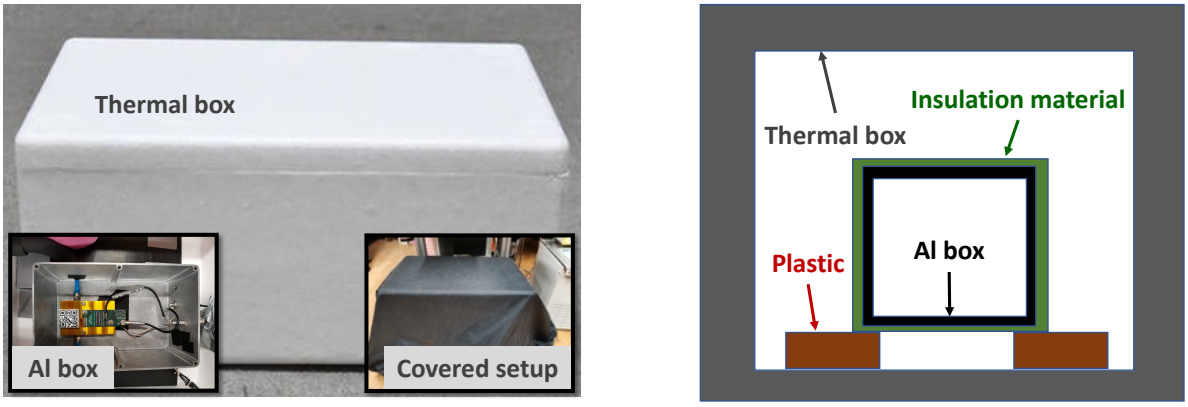

(a) Pictures of setup. **(b)** Schematic of setup.

Figure 6.13: Temperature dependency measurement setup. (a) The measurement setup was installed in a thermal box covered with black fabric for light block-out. (b) The setup was optimized for enhanced thermal insulation, including minimizing direct contact with the wall and additional coating for the Al box.

SiPM. The relative position of the measured SiPM and the temperature in the Matrix is also provided in Figure 6.14.

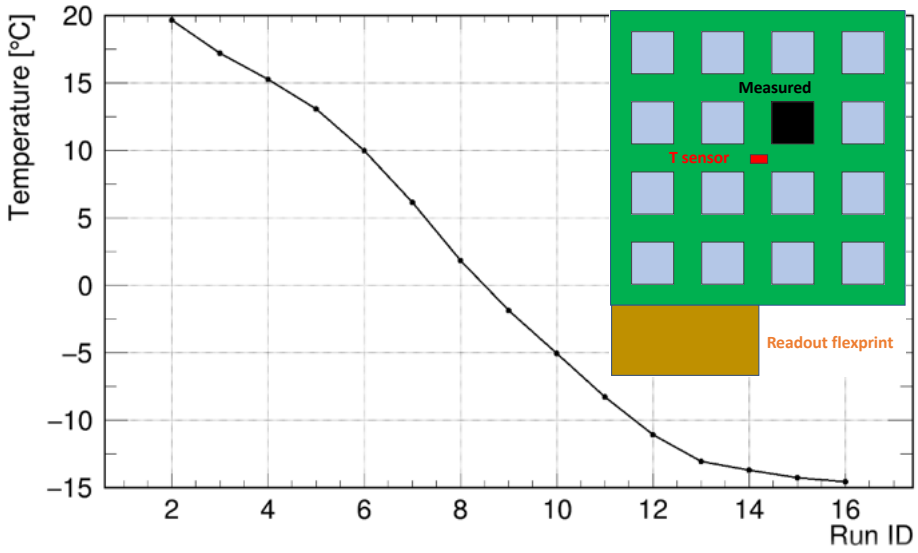

Figure 6.14: Temperature monitored on Matrix 6 in various runs. The inset in the upper-right corner displays the Matrix schematic with measured SiPM and temperature sensor indicated, where the SiPM closest to the temperature sensor was measured for more accurate temperature assessment.

Forward current

The forward IV curve was measured at different temperatures, and results are plotted in Figure 6.15. The overall resistor $R = R_0 + R_q/N_{pixel}$ and V_k were obtained with linear fitting, and the results are shown in Figure 6.16. No strong dependency of the resistor on the temperature in the measured range was found.

In contrast, a clear temperature dependency of V_k was obtained coefficient of $dV_k/dT = -1.95\,\mathrm{mV/°C}$ as shown in Figure 6.17.

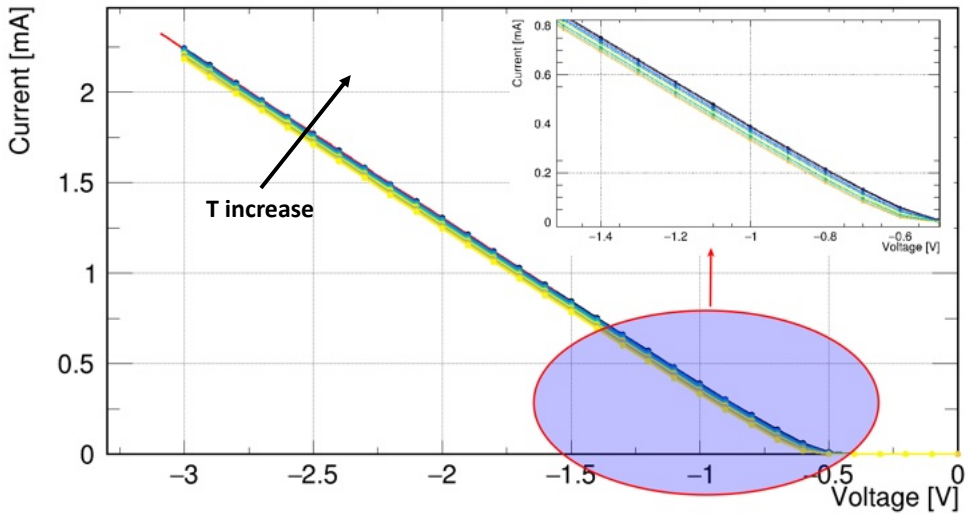

Figure 6.15: Forward IV curve at different temperatures. The IV curve shifts towards the upper-right as temperature increases, resulting in smaller V_k. No significant change in slope suggests constant R_q.

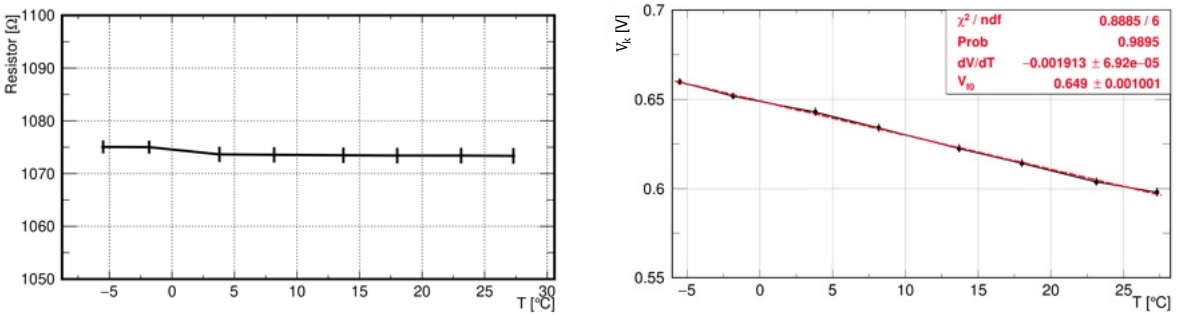

(a) The overall resistor $R = R_0 + R_q/N_{pixel}$.

(b) The knee voltage V_k.

Figure 6.16: Overall resistor and V_k obtained for different temperatures.

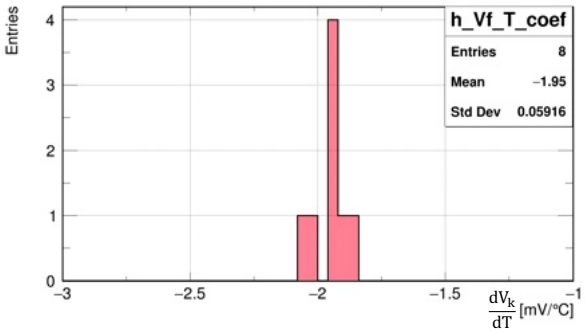

Figure 6.17: Temperature coefficient of V_k acquired from SiPMs exposed to different doses, with an average value of −1.95 mV/°C.

Breakdown voltage and dark current above breakdown voltage

The reverse IV curve was measured at different temperatures to characterize the temperature dependency of V_{br} and I_{d} above V_{br}.

Figure 6.18a shows the reverse IV curves at different temperatures. Figure 6.18b shows the obtained V_{br} plotted versus temperature for different SiPMs, and all the measured data are in the range of the given V_{br} from the datasheet which is the green region in the plot. The measured V_{br} agrees with the expectation very well with a temperature coefficient of 54 mV/°C.

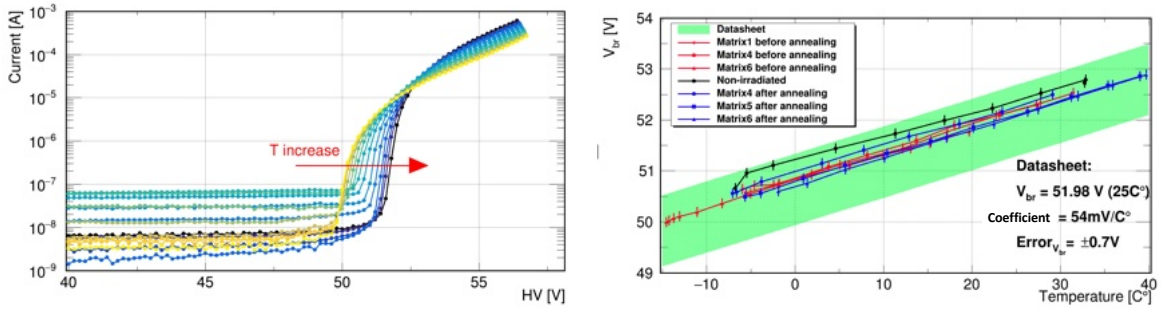

(a) Reverse IV curve at different temperatures.

(b) V_{br} versus temperature.

Figure 6.18: (a) Reverse IV curve and (b) V_{br} at varying temperatures. (b) The V_{br} from non-irradiated SiPMs differs the most from the datasheet value, primarily due to the large analysis uncertainty caused by the very small dark current.

The I_{d} at a constant over-voltage V_{ov}, instead of bias constant HV, was used to investigate the temperature dependency of I_{d} to exclude the temperature dependency of V_{br}. The reverse current at different V_{ov} is shown in Figure 6.19a, where temperature dependency of V_{br} was excluded by data from Figure 6.18b. The I_{d} with $V_{\mathrm{ov}} = 3.7\,\mathrm{V}$ at different temperature is plotted in Figure 6.19b, where the current was normalized to the $I_{\mathrm{d}}(T = 10\,^{\circ}\mathrm{C})$.

As reported in [130], the dark current can be written as

$$I_{\mathrm{d}} = q_e \cdot G \cdot r_{\mathrm{d}} \propto G \cdot T^{\gamma} \cdot e^{-\frac{E_{\mathrm{a}}}{kT}}, \tag{6.12}$$

where q_e is the charge of electron, G is the gain of SiPM, r_{d} is the DCR, T is the temperature, E_{a} is the active energy of silicon and k is the Boltzmann constant. Furthermore, $\gamma \sim 3$ for diffusion and ~ 2 for generation. Because the T^{γ} item is not important compared to the exponential item $e^{-\frac{E_{\mathrm{a}}}{kT}}$ [131], the temperature dependency of I_{d} is usually simplified to

$$I_{\mathrm{d}} \propto e^{-\frac{E_{\mathrm{a}}}{kT}}. \tag{6.13}$$

Therefore, the normalized I_{d} should follow

$$I_{\mathrm{d}} = A \cdot e^{\frac{T}{T_0}} \tag{6.14}$$

with parameters A and T_0. The parameter T_0 is a characteristic temperature whereby an increase in temperature by T_0 results in an increase of I_{d} by a factor of e. And $T_0 = 15.70\,^{\circ}\mathrm{C}$ was obtained by fitting

the measured data as shown in Figure 6.19b.

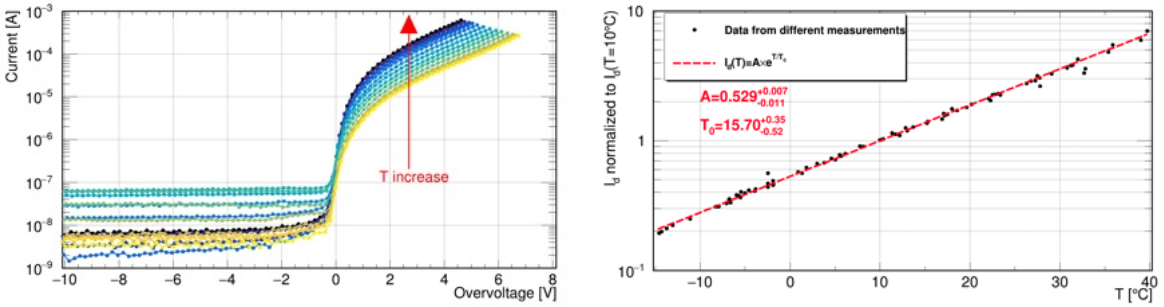

(a) Reverse current along different V_{ov}.

(b) I_d with $V_{ov} = SI3.7V$ versus temperature.

Figure 6.19: (a) IV curve and (b) I_d with a constant V_{ov} at different temperatures. (b) Fitting results reveal that I_d decreases by a factor of e when the temperature drops by 15.7 °C.

6.2 Noise Analysis

As discussed in subsection 6.1.2, the accumulation of dark events resulting from radiation damage leads to an increase in the average signal current, which is commonly used to characterize irradiated SiPMs. In addition to this, the stochastic nature of dark events' generation leads to significant fluctuations on the baseline, which is considered as an additional noise source in signal processing. This is particularly important for precise timing measurement. Measuring the RMS of the sensor output signal at different irradiation doses is a common method used to characterize this noise source. However, there is currently no clear parametric model available to explain and analyze the RMS, providing limited understanding of the mechanism and insufficient information for further application.

In this study, we characterized irradiated SiPMs based on noise analysis in the f-domain to gain further insights into the sensors. The *Power Spectral Density* (PSD) was investigated to better understand the overall noise contribution, and a parameterized model dependent on irradiation dose was employed to model the noise.

6.2.1 Noise in SiPMs

Due to different physical origins, the noise in SiPMs and their readout electronics can be subdivided into three categories: external noise, generic electronic noise, and SiPM-specific noise. External noise is noise from the external system and can be minimized by optimizing the external system; it will not be discussed in this subsection.

Generic electronic noise

The current signal in an electronic system can be expressed as a function of the number N and velocity v of the charge carriers:

$$i = \frac{Q}{t} = \frac{Ne}{d/v} = \frac{Nev}{d}, \tag{6.15}$$

where e is the elementary charge, and d is the distance traveled by the charge $Q = Ne$. Therefore, the electronic noise can be given by the fluctuation of charge carrier number dN or velocity dv:

$$(\mathrm{d}i)^2 = (\frac{ev}{d})^2(\mathrm{d}N)^2 + (\frac{Ne}{d})^2(\mathrm{d}v)^2. \tag{6.16}$$

This indicates that any process that can fluctuate the number and velocity of charge carriers should deliver electronic noise. For instance, both charge carrier emission over a barrier and the trap/release process can lead to charge carrier number fluctuation, resulting in shot noise and flicker ($1/f$) noise, respectively. The Brownian motion due to the thermal motion of the charge carriers results in the velocity fluctuation, which is called thermal noise. There are many more physical origins for electronic noise, which makes it tricky to distinguish all the noise origins.

The PSD S_ω was employed to characterize noise in the f-domain, which can be calculated from the measured signal $s(t)$ in the time domain (t-domain):

$$S(\omega) = \lim_{\Delta t \to \infty} \frac{1}{\Delta t} |\mathcal{F}[s(t)]|^2, \tag{6.17}$$

where Δt is the time period of measured signal $s(t)$ and the $\mathcal{F}[s(t)]$ is the Fourier Transform of $s(t)$. The most common electronic noise types are "white" noise with $\mathrm{d}S(\omega)/\mathrm{d}\omega = 0$ and flicker noise with $S(\omega) \propto 1/f^\gamma$. Therefore, the PSD of common electronic noise has a spectrum similar to what is shown in Figure 6.20.

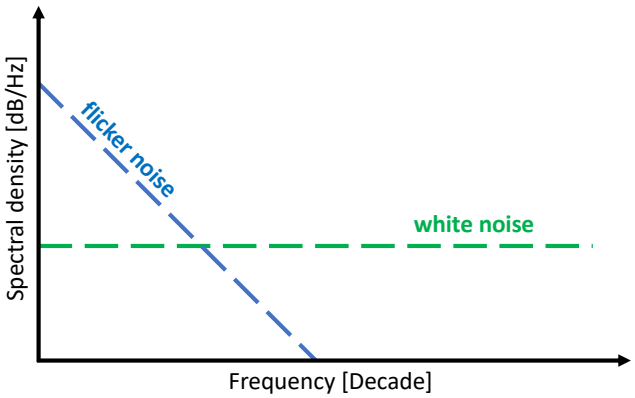

Figure 6.20: PSD of common electronic noise with white noise and $1/f$ noise.

SiPM-specific noise

The SiPM-specific noise discussed in this work is the noise related to the SiPM dark count events, which was found to be the main noise source for irradiated SiPMs. A SiPM signal response model was developed to understand the SiPM-specific noise. The generation of the dark count events in SiPM is a homogeneous Poisson process with a constant DCR r_d. Therefore, the sequence of firing timings (spike train) $s_\mathrm{in}(t)$ in a period Δt can be given by

$$s_{\text{in}}(t) = \sum_{j=1}^{N=r_{\text{d}}\cdot\Delta t} \delta(t - t_j), \tag{6.18}$$

where N is the total number of dark count events in the interested time period Δt and t_j is the time when the j-th event occurs. With the assumption that all the dark-event responses are identical, which is a requirement for the device design, the total response output $s_{\text{out}}(t)$ from a SiPM can be expressed as the convolution of the identical response $h(t)$ and the spike train $s_{\text{in}}(t)$:

$$s_{\text{out}}(t) = h(t) * s_{\text{in}}(t). \tag{6.19}$$

Based on Equation 6.17, the PSD of SiPM response $S_{\text{out}}(\omega)$ can be expressed as

$$\begin{aligned} S_{\text{out}}(\omega) &= \lim_{\Delta t\to\infty} \frac{1}{\Delta t}|\mathcal{F}[s_{\text{out}}(t)]|^2 \\ &= \lim_{\Delta t\to\infty} \frac{1}{\Delta t}|\mathcal{F}[h(t) * s_{\text{in}}(t)]|^2 \\ &= \lim_{\Delta t\to\infty} \frac{1}{\Delta t}|\mathcal{F}[h(t)] \cdot \mathcal{F}[s_{\text{in}}(t)]|^2 \\ &= |\mathcal{F}[h(t)]|^2 \cdot \lim_{\Delta t\to\infty} \frac{1}{\Delta t}|\mathcal{F}[s_{\text{in}}(t)]|^2 \\ &= |H(\omega)|^2 \cdot S_{\text{in}}(\omega), \end{aligned} \tag{6.20}$$

where $H(\omega) = \mathcal{F}[h(t)]$ is the Fourier Transform of $h(t)$ and $S_{\text{in}}(\omega)$ is the PSD of the spike train $s_{\text{in}}(t)$. A schematic of the model is shown in Table 6.5.

Table 6.5: Model of SiPM response in t-/f-domain with treating SiPM as a linear time-invariant (LTI) system.

	IN	SiPM	OUT
model			
t-domain	( ) = $\sum_{=}^{=}$ ( )	( )	( ) = ( ) ( )
f-domain	( ) = —| [( )]|	( ) = [( )]	( ) = ( ) | ( )|

Therefore, the PSD of SiPM-specific noise can be divided into two parts:

- $S_{\text{in}}(\omega)$ which represents the number fluctuation of the dark events and indicates the statistical feature of the stochastic process,
- and $H(\omega)$ which expresses the frequency components of the single-event waveform and indicates the single-event feature dominated by the rise and decay time of the SiPM.

Statistical feature $s_{\text{in}}(t)$ is defined in Equation 6.18, then its Fourier transform is:

$$\begin{aligned}\mathcal{F}[s_{\text{in}}(t)] &= \mathcal{F}[\sum_{j=1}^{N}\delta(t-t_j)] \\ &= \int \sum_{j=1}^{N}\delta(t-t_j)\cdot e^{-i\omega t}\cdot \mathrm{d}t \\ &= \sum_{j=1}^{N} e^{-i\omega t_j}.\end{aligned} \tag{6.21}$$

Thus,

$$\begin{aligned}|\mathcal{F}[s_{\text{in}}(t)]|^2 &= \mathcal{F}[s_{\text{in}}(t)]\cdot\mathcal{F}^*[s_{\text{in}}(t)] \\ &= (\sum_{j=1}^{N} e^{-i\omega t_j})\cdot(\sum_{k=1}^{N} e^{i\omega t_k}) \\ &= \sum_{j=1}^{N}\sum_{k=1}^{N} e^{-i\omega(t_j-t_k)} \\ &= \sum_{j=1}^{N}(\sum_{k=j}^{N} e^{-i\omega(t_j-t_k)} + \sum_{k\neq j,k=1}^{N} e^{-i\omega(t_j-t_k)}) \\ &= \sum_{j=1}^{N} 1 + \sum_{j=1}^{N}\sum_{k\neq j,k=1}^{N} e^{-i\omega(t_j-t_k)} \\ &= N + \sum_{j=1}^{N}\sum_{k\neq j,k=1}^{N} e^{-i\omega(\Delta t_{jk})},\end{aligned} \tag{6.22}$$

where $\Delta t_{jk} = t_j - t_k$ is used to simplify the symbol for better discussion. Since the indices j and k both range from 1 to N, any Δt_{jk} can find another $\Delta t'_{jk}$ and satisfy $\Delta t_{jk} + \Delta t'_{jk} = 0$. Thus, Equation 6.22 can be simplified to

$$\begin{aligned}|\mathcal{F}[s_{\text{in}}(t)]|^2 &= N + \sum_{j=1}^{N}\sum_{k\neq j,k=1}^{N} cos(\omega\Delta t_{jk}) \\ &= r_{\text{d}}\Delta t + \sum_{j=1}^{r_{\text{d}}\Delta t}\sum_{k\neq j,k=1}^{r_{\text{d}}\Delta t} cos(\omega\Delta t_{jk})\end{aligned} \tag{6.23}$$

and the corresponding PSD can be given based on Equation 6.17:

$$\begin{aligned}S_{\text{in}}(\omega) &= \lim_{\Delta t\to\infty}\frac{1}{\Delta t}|\mathcal{F}[s_{\text{in}}(t)]|^2 \\ &= \lim_{\Delta t\to\infty}\frac{1}{\Delta t}(r_{\text{d}}\Delta t + \sum_{j=1}^{r_{\text{d}}\Delta t}\sum_{k\neq j,k=1}^{r_{\text{d}}\Delta t} cos(\omega\Delta t_{jk})) \\ &= r_{\text{d}} + \lim_{\Delta t\to\infty}(\sum_{j=1}^{r_{\text{d}}\Delta t}\sum_{k\neq j,k=1}^{r_{\text{d}}\Delta t} cos(\omega\Delta t_{jk})) \\ &= r_{\text{d}} + r_{\text{d}}^2\delta(\omega).\end{aligned} \tag{6.24}$$

Hence, the spike train $s_{\text{in}}(t)$ (Equation 6.18) of independent times t_j behaves almost like a white noise, as its power spectrum is flat for all frequencies, except for the spike at $\omega = 0$. Therefore, the PSD of $s_{\text{in}}(t)$ can be simplified to

$$S_{\text{in}}(\omega) = r_{\text{d}}, \tag{6.25}$$

with the direct-current ($\omega = 0$) excluded, as it has been discussed in subsection 6.1.2.

Equation 6.25 indicates the profile of the overall PSD $S_{\text{out}}(\omega)$ is independent of the statistical feature, while the amplitude of $S_{\text{out}}(\omega)$ is proportional to the DCR r_{d}.

Single-event feature The ideal response $h(t)$ of the SiPM is a double exponential, as shown in Equation 6.3, and its corresponding frequency spectrum is depicted in Figure 6.21. Under the assumption that all the dark events have identical response, the overall noise profile is constant, and the amplitude increases with DCR. The overall noise profile is dominated by the pile-up of the slow recovery tail from SiPM's single-event response, and the low-pass feature of the exponential tail leads to the plateau with a fixed cutoff frequency.

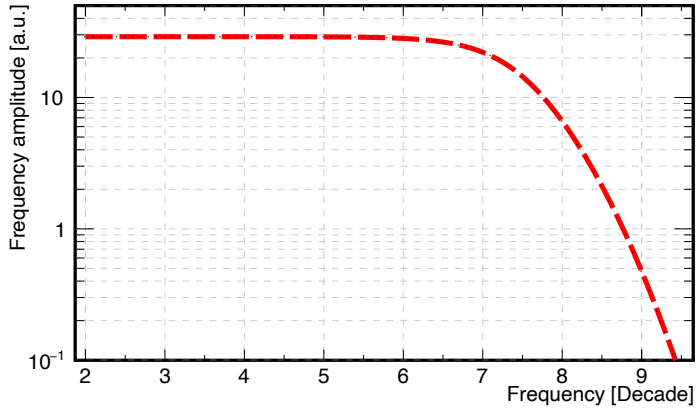

Figure 6.21: Frequency response of the ideal SiPM single-event response $h(t) = e^{-t/\tau_{decay}}(1 - e^{-t/\tau_{rise}})$ with $\tau_{decay} = 30\,\text{ns}$ and $\tau_{rise} = 1\,\text{ns}$.

To summarize, the PSD of the SiPM-specific noise is a combination of a low-pass-like spectrum and white spectrum, as shown in Figure 6.22. The overall noise PSD for SiPM is the merge of Figure 6.20 and Figure 6.22: a combination of $1/f$, low-pass-like, and white spectrum.

6.2.2 Laboratory characterization

The noise waveforms of SiPMs have been recorded using an oscilloscope with the setup shown in Figure 6.23. The SiPM Matrix board was mounted on an aluminum block cooled by water at 10 °C to stabilize the temperature. Moreover, V_{ov} was set to 3.7 V and the SiPMs were read out individually by the oscilloscope via two adapter boards. To minimize the influence from the light source, the setup was installed in a black box. The measured waveform is the voltage over a 50-ohm resistor and the waveform examples for SiPMs with different radiation doses are given in Figure 6.24.

To characterize the noise in a large frequency range, the measurements need to cover extremely low and high frequencies with different runs. A total waveform length of 1000 s, the combination of 2000

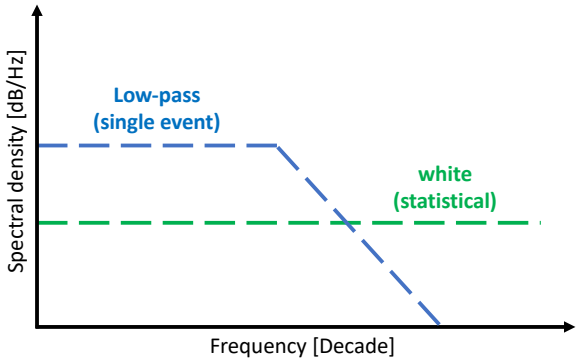

Figure 6.22: Schematic of PSD contributed from SiPM-specific noise.

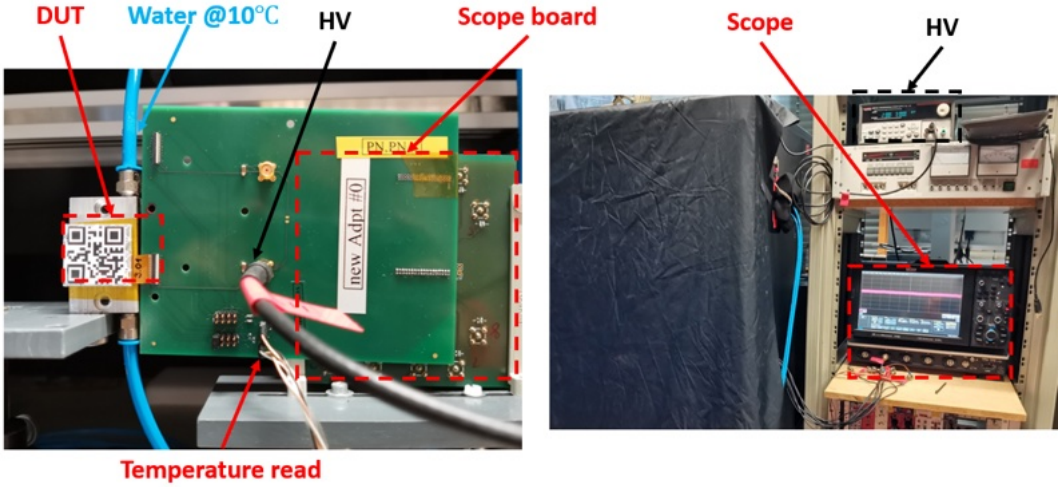

Figure 6.23: SiPM noise measurement setup. Installed in a large black box for light-tightness, the DUT Matrix was cooled by water at $T = 10\,^{\circ}\mathrm{C}$. Noise waveforms were individually read out by an oscilloscope outside the black box, with signal reading and HV supply via adapter boards.

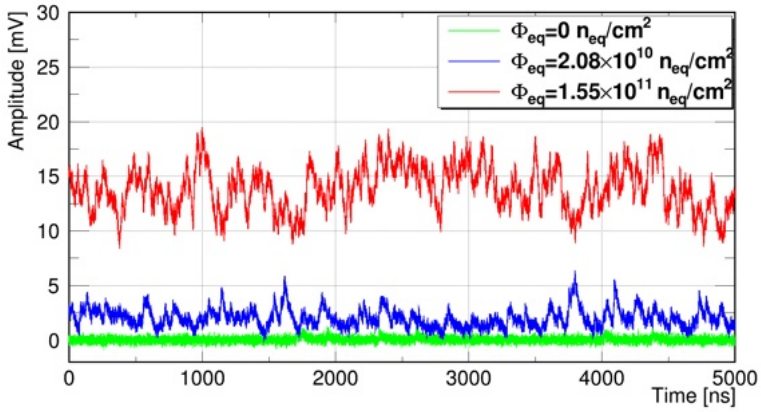

Figure 6.24: Waveform examples from SiPMs with different radiation doses. Noticeable increases were observed in both the baseline level and the fluctuations. The amplitude represents the voltage over a 50-ohm resistor.

waveforms with 0.5 s each, was measured to reach the lowest frequency of 10^{-3} Hz. To reduce the variance at the extremely low frequency range during estimation, Welch's method with a Hann window was applied in the PSD estimation [132]. On the contrary, a total time frame of 1.6 ms was measured with a sampling rate of 20 GS/s to probe the higher frequency region. The periodogram technique with a rectangle window [133] was employed to keep all the characteristics of the noise in the frequency domain and minimize the artifacts from the implemented time window simultaneously. Furthermore, the spectral subtraction method [134] was employed to minimize the interference from the inherent noise of the measurement system, which was represented by the noise measured without bias voltage on the SiPM.

6.2.3 Analysis and results

Figure 6.25 presents noise PSDs from two irradiated SiPMs with different doses in the frequency range from 10^{-2} to 10^{8} Hz[1]. To better quantify and understand the noise origins, the spectrum was split into 3 parts based on frequency, namely from 10^{-2} to $10^{0.5}$ Hz as the Low-Frequency Region (LFR), from 10^{3} to 10^{8} Hz as the High-Frequency Region (HFR) and the Transition Region (TR) in between.

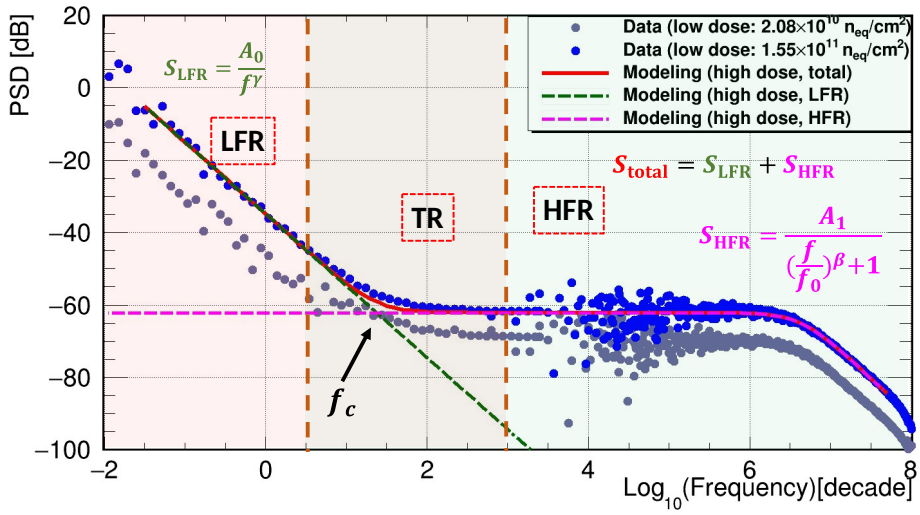

Figure 6.25: Noise PSDs from two irradiated SiPMs with different doses. The y-axis is in dB, where PSD[dB] = 10·log(PSD[mV^2/Hz]). Note that all PSDs and formulas in this work utilize normal units (mV^2/Hz), which are more convenient for discussion. Unless explicitly stated, PSD amplitude values (A_0 and A_1) are also in normal units.

LFR

An empirical formula, A_0/f^{γ}, was employed to describe the noise in the LFR due to its similarity to typical 1/f noise and examples with different doses are shown in Figure 6.26. The value of A_0 equals to the noise PSD amplitude at 1 Hz $S_{\mathrm{LFR}}(f = 1\ \mathrm{Hz})$. And γ determines the attenuation slope of the PSD.

[1] The extremely low frequency range ($< 10^{-2}$ Hz) has a big variance and the noise contribution in this small frequency range is negligible; The PSD above $> 10^{8}$ Hz is extremely low and leads to negligible noise contribution as well.

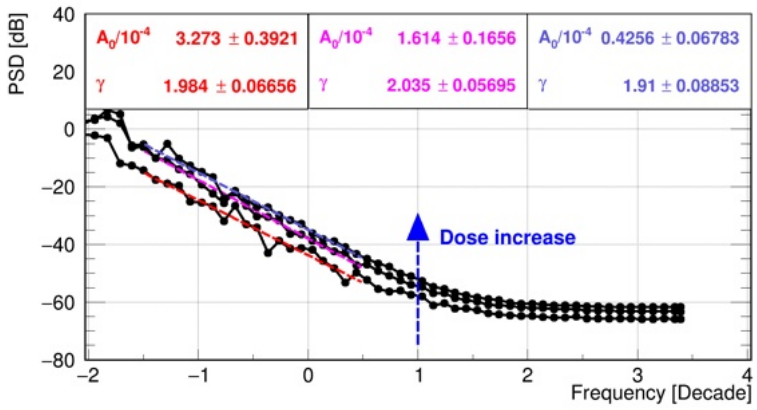

Figure 6.26: LFR noise PSDs from three SiPMs with different irradiation doses (fitted with $S_{\mathrm{LFR}} = A_0/f^{\gamma}$). As A_0 equals the PSD value at $f = 1$ Hz, A_0 in this work will be written in $\mathrm{mV^2Hz^{-1}}$ instead of $\mathrm{mV^2Hz^{\gamma-1}}$ for greater physical relevance.

The parameters γ and A_0 were obtained by fitting the noise PSD in the LFR with A_0/f^{γ} and results from SiPMs with different doses are shown in Figure 6.27. The exponent γ remains a constant of 1.973 (±0.032) for SiPMs with different irradiation doses, which is as expected due to the similar slope in different SiPMs. The γ from low irradiation dose (small I_{d} in the plot) has the biggest difference to the mean value because its PSD is very small such that the background subtraction leads to a big slope uncertainty. Various polynomials were tried to determine relationship between A_0 and I_{d} , whose optimum is $A_0 = a \cdot I_{\mathrm{d}}^{b}$. And the coefficient a and exponent b obtained from the fitting are 1.563 (±0.303) × 10^{-3} and 1.455 (±0.099), respectively.

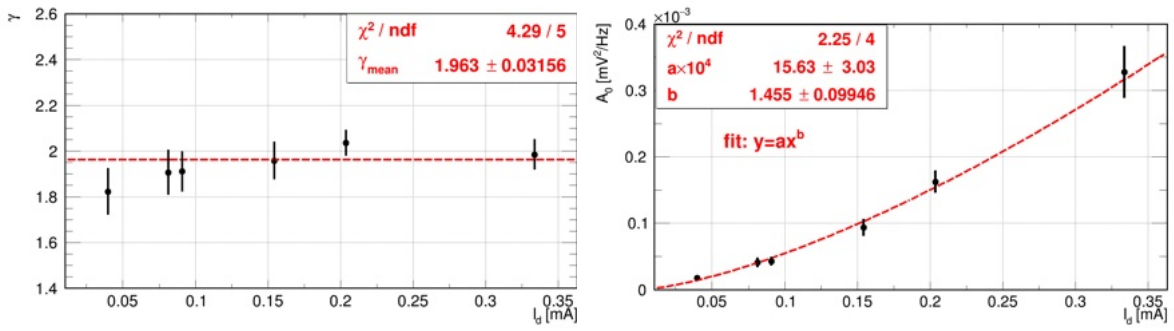

(a) Parameter γ.

(b) Parameter A_0.

Figure 6.27: Parameters in S_{LFR} from SiPMs' LFR PSD with different irradiation doses. The constant γ indicates a similar defect center distribution in SiPMs with varying doses. A_0 can be well described by $A_0 = a \cdot I_{\mathrm{d}}^{b}$.

Although many studies have been conducted to understand the low-frequency noise in semiconductor devices [135–138], it is still hard to develop a quantitative theoretical model to explain the $1/f$ noise in a sensor with thousands of diodes, resistors and capacitors. And no $1/f$ noise study on irradiated SiPM was found in previous studies. Fortunately, the past $1/f$ studies on general semiconductor devices [139–141] and irradiation effects [142] can still provide some inspiration.

In semiconductor devices, the $1/f$ noise is primarily caused by the defects and impurities and this

is ascribed by McWhorter to fluctuations in the carrier number caused by surface charge trap/release processes. The slope γ is dominated by the relaxation time constant distribution of all the trapping centers. The relaxation time constant distribution for all the irradiated SiPMs in this work should be the same, because all the SiPMs are identical in design and all of them are exposed to the same radiation field which delivers the same amount of defect centers. This explains why all the noise PSDs from SiPMs with different doses have a similar slope γ. Moreover, the A_0 can be roughly given by $A_0 = a \times I_{\mathrm{d}}^{b}$ with b = 1.455 (±0.099) in this work and similar exponents between 1 and 2 were reported in other irradiated devices [143].

Overall, the LFR noise PSD (S_{LFR}) of irradiated SiPMs can be well modeled by $S_{\mathrm{LFR}} = A_0/f^{\gamma}$, with γ =1.963 (±0.032) and A_0 = 1.563 (±0.303) × $10^{-3} I_{\mathrm{d}}^{1.455\ (\pm 0.099)}$. The dependence between PSD and the radiation dose indicates that the defect centers created by irradiation damage might be one of the main origins of the noise.

HFR

Concerning the HFR, a formula similar to the low-pass filter power response, $A_1/((f/f_0)^{\beta} + 1)$, was implemented for modeling due to the similarity with the response of the low-pass filter. A flat region between 10^4 and 10^6 Hz, referred to as plateau later, with a cutoff at the same frequency has been identified in all the SiPMs' noise PSDs.

Both attenuation slope β and cutoff frequency f_0 have been identified to be constant in all the irradiated SiPMs, which are β = 2.024 (±0.033) and f_0 = 6.598 (±0.035) decade, as shown in Figure 6.28. Moreover, the amplitude of the plateau A_1 distribution is given in Figure 6.29a and the profile matches the dose distribution (see Figure 6.29b) very well. Further investigation on A_1 shows that it scales linearly with respect to the dark current measured in each SiPM with a slope of 2.444 (±0.016) × 10^{-6} $(\mathrm{mV}^2/\mathrm{Hz})/\mathrm{mA}$, as shown in Figure 6.30.

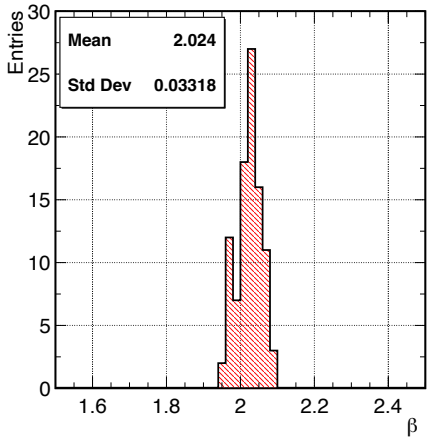

(a) Parameter β.

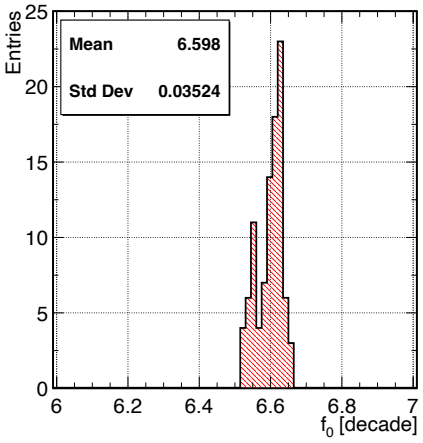

(b) Parameter f_0.

Figure 6.28: Parameters in the $S_{\mathrm{HFR}} = A_1/((f/f_0)^{\beta} + 1)$ obtained from all the irradiated SiPMs. (f_0[decade] = $\mathrm{Log}_{10}(f_0[\mathrm{Hz}])$). Both parameters remain constant across different radiation doses due to the similar PSD profiles in the HFR.

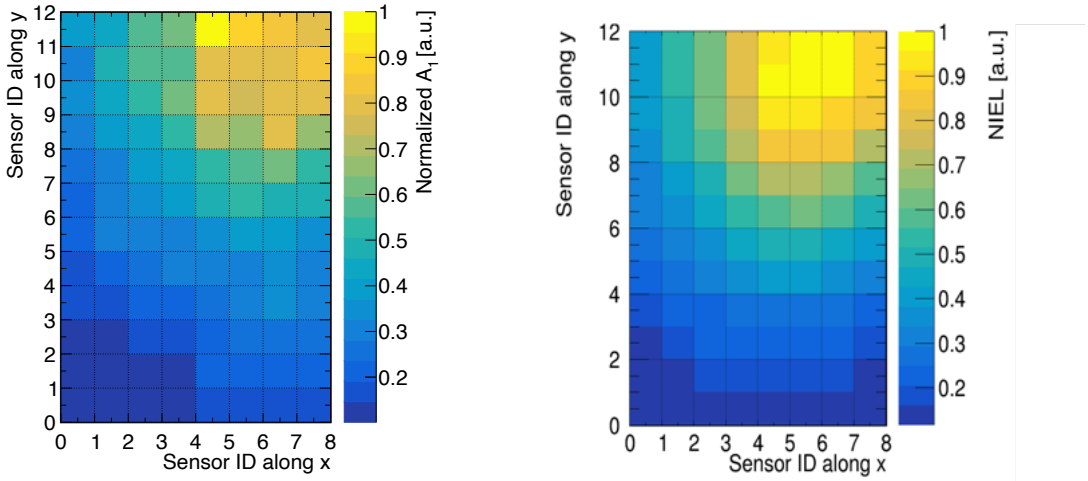

(a) A_1 distribution

(b) Dose Φ_{eq} distribution

Figure 6.29: 2D distribution of the plateau amplitude A_1 (left) and the normalized dose Φ_{eq} (right) along the sensor ID. Both are normalized to their maximum values, and their profiles closely match each other.

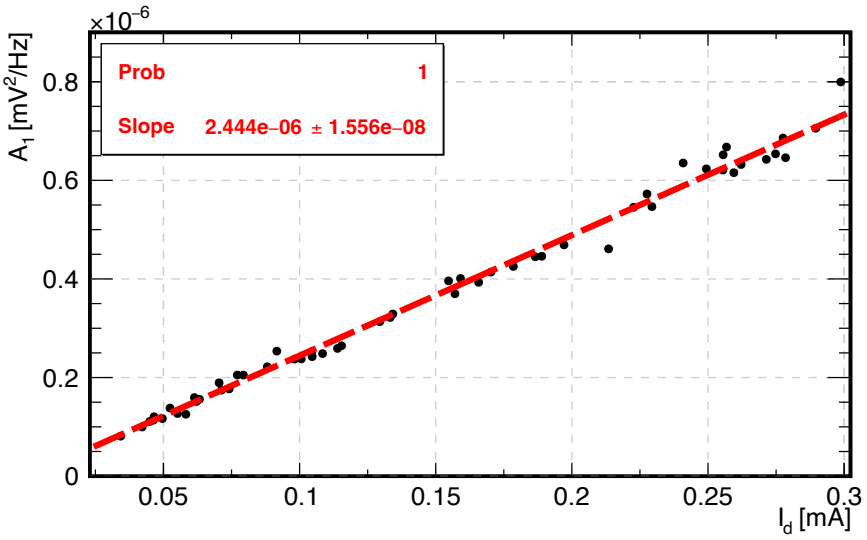

Figure 6.30: PSD plateau amplitude A_1 for SiPMs with different doses. Error bars are not presented due to the unknown temperature uncertainty. The fitting function (red line) is $A_1 = \text{Slope} \cdot I_d$.

The similarity of the cutoff frequency and linearity between A_1 and I_d agree well with the prediction of the SiPM-specific noise calculation discussed in subsubsection 6.2.1. Therefore, the noise in the HFR is presumably dominated by the pile-up of the slow recovery tail from the SiPM's single-event response, whose amplitude scales linearly with the DCR and the profile is only determined by the SiPM single-event waveform.

To have further quantitative investigation, the SiPM response with different DCRs was simulated based using the generic SiPM simulation framework, GosSiP[144]. To guarantee the simulation accuracy, important SiPM parameters were obtained from the datasheet or careful measurement (listed in Table 6.6). With setting different DCR, corresponding waveforms were generated with a sampling rate of 2 GS/s and a total length of 1 ms. Then the same analysis process implemented on lab-measured data was employed for analysis. Figure 6.31 shows an example of a comparison between measurement and simulation, where similar features was found in both spectrums.

Table 6.6: SiPM (13360-2050EV) Parameters for the GosSiP Simulation

Parameter	Value	Description	Comment
Npx, Npy	60,60	number of pixels	data sheet
Dx, Dy	50 um, 50 um	pixel dimension	data sheet
XT	7.6%	cross-talk probability	measured
τ_{rise}, τ_{decay}	1 ns, 30 ns	rise/decay time	measured
A_{single}	0.5 mV	single-event amplitude	measured
RMS_{en}	0.21 mV	RMS of the electronic noise	measured
r_d	–	DCR	variable

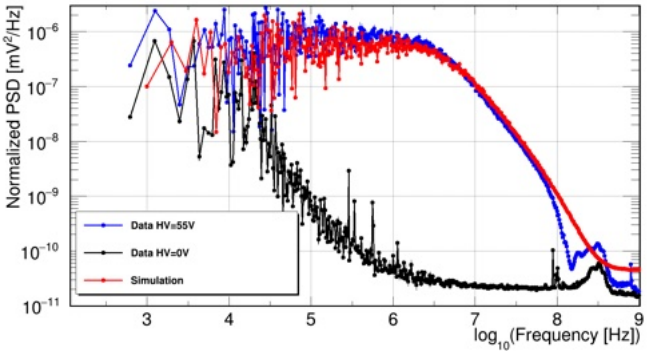

Figure 6.31: PSD comparison between measurement (blue) and simulation (red), including noise PSD from the measurement system (black). The PSD above 8 decades does not agree well with the simulation due to the measurement system.

The low-pass feature was also identified in all simulated PSDs with different DCRs (see Figure 6.32a) and the characteristic parameters (β, f_0 and A_1) were obtained from the PSDs. Both constants β and f_0, with 2.057 and 6.743 decade separately, agree well with the results obtained from measured data with relative errors of 1.63% and 2.20%. And the linearity between A_1 and the DCR was found in a DCR scale of 6 magnitudes, see Figure 6.32b, which not only shows a good agreement with measured

data but also verifies the assumption in a larger DCR range.

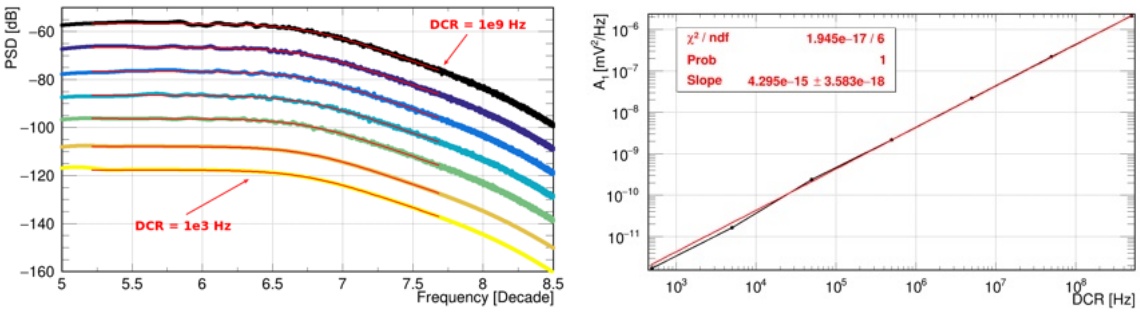

(a) PSD with different DCR

(b) A_1 along DCR

Figure 6.32: Simulation results with different DCRs. (a) Similar PSD profiles for different DCRs verify the developed model to describe noise in HFR. (b) The fit function is $A_1 = \text{Slope} \cdot r_\text{d}$, and the good agreement between fit results and measurement confirms the relationship between A_1 and I_d, even on a larger scale compared to the measurement.

Overall, the noise PSD (S_HFR) in HFR for different irradiation doses can be well described by $S_\text{HFR} = A_1/((f/f_0)^\beta + 1)$, with $\beta = 2.024$ (± 0.033), $f_0 = 6.598$ (± 0.035) decade and $A_1 = 2.444$ (± 0.016) $\times$ 10^{-6} (mV^2/Hz)/mA $\cdot\, I_\text{d}$. Both theoretic calculation and simulation in this section pointed out that the low-pass feature comes from the tail's time feature of SiPM's single-event response.

It should be noticed that all the SiPMs discussed here are only irradiated with low doses compared to SiPMs used in big experiments like HL-LHC [145]. The results might be different for SiPMs with a very high dose where the DCR r_d is too high to satisfy the assumption that the single-event response is identical due to strong pile-up in the same pixel. The pile-up in the same pixel will change the waveform tails, which results in the equivalent SiPM single-event response $h'(t)$ will not be independent to the dose anymore and leads to less contribution to PSD in the lower frequency range. Therefore, the PSD profile will change along dose and corresponding amplitude parameter A_1' will saturate at specific dose level. Thus, additional parameters are needed to describe the PSD at this dose level.

TR

TR is the region where neither S_LFR nor S_HFR can be ignored. The corner frequency f_c in the TR was defined as the frequency where $S_\text{LFR}(f_\text{c}) = S_\text{HFR}(f_\text{c})$. Thus, the $1/f$ noise dominates in the frequency range $f < f_\text{c}$ and the SiPM-specific noise dominates the range $f > f_\text{c}$, which means f_c is the characteristic frequency to separate noise from two totally different mechanisms.

Since $S_\text{HFR} \approx A_1$ in TR due to $f \ll f_0$, the solution of f_c from $S_\text{LFR}(f_\text{c}) = S_\text{HFR}(f_\text{c})$ is:

$$f_\text{c} = (\frac{A_0}{A_1})^{1/\gamma}, \tag{6.26}$$

where A_0, γ and A_1 are the parameters discussed in the LFR and HFR sections.

The f_c can be directly estimated by employing the parameter values obtained from LFR and HFR sections, which yields:

$$f_\text{c} = 26.787 \times I_\text{d}^{0.231}, \tag{6.27}$$

where I_d is in unit of mA. Equation 6.27 shows that the f_c only slowly increases with I_d increasing. Moreover, the f_c can also be obtained by directly fitting the PSD in the TR, as example shown in Figure 6.33.

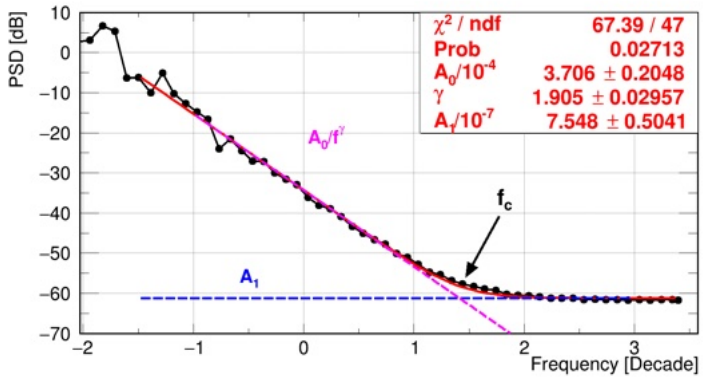

Figure 6.33: PSD in TR fitted with $S_{TR} = S_{LFR} + S_{HFR} \approx A_0/f^{\gamma} + A_1$. f_c is the frequency which fulfills $S_{LFR}(f_c) = S_{HFR}(f_c)$.

Figure 6.34 shows f_c from direct fitting, which matches Equation 6.27 with the biggest difference being smaller than 10 Hz. The measured f_c is constantly bigger than the theoretical value, especially for those obtained from SiPMs with the lowest dose. It was found that the shift is due to the background noise subtraction which leads to smaller γ when the background noise dominates the PSD around the corner region and then results in bigger f_c. Therefore, the overall fitting does not work well for the PSD with low dose. Fortunately, the results obtained from separated fitting of the PSD in LFR and HFR match Equation 6.27 very well.

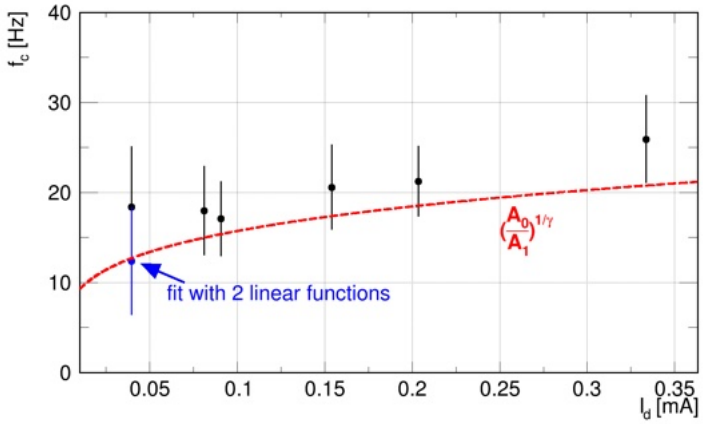

Figure 6.34: Corner frequency f_c obtained from SiPMs' PSD with different doses. Equation 6.27 (red dashed line) calculated based on parameters obtained from LFR and HFR sections; (black data points) f_c from direct fitting: $S_{TR} = A_0/f^{\gamma} + A_1$; (blue data point) f_c of the least irradiated SiPM obtained from fitting A_0/f^{γ} in $10^{-1.5}$ Hz to $10^{0.5}$ Hz and fitting A_1 in $10^{2.5}$ Hz to $10^{3.4}$ Hz.

Overall, the corner frequency f_c for all the SiPMs evaluated in this work is between 10 and 30 Hz, which can be roughly estimated by Equation 6.27. It concludes that the noise from 10^{-2} to 10 Hz is dominated by the $1/f$ noise (discussed in LFR section) and from 30 to 10^8 Hz is dominated by the DCR

events time response (discussed in HFR section).

In conclusion, the noise PSD studies clearly shows that different features were found in different frequency range and the PSD can be well modeled by

$$S_{\text{total}} = S_{\text{LFR}} + S_{\text{HFR}} = \frac{A_0}{f^{\gamma}} + \frac{A_1}{(\frac{f}{f_0})^{\beta} + 1}, \tag{6.28}$$

where all the parameters are listed in Table 6.7.

Table 6.7: Parameter summary for the noise PSD in Equation 6.28.

Parameter	Symbol	Description	value	unit
$S_{\text{LFR}}(f = 1\text{ Hz})$	$\boldsymbol{A_0}$	$\propto I_{\text{d}}^{b}$	$1.563\ (\pm 0.303)\times 10^{-3} I_{\text{d}}^{1.455\ (\pm 0.099)}$	$\text{mV}^2\cdot\text{Hz}^{-1}$
Exponent of 1/f noise	$\boldsymbol{\gamma}$	Constant	1.963 (±0.032)	unitless
$S_{\text{HFR}}(f = 0\text{ Hz})$	$\boldsymbol{A_1}$	$\propto I_{\text{d}}$	$2.444\ (\pm 0.016)\times 10^{-6} I_{\text{d}}$	$\text{mV}^2\cdot\text{Hz}^{-1}$
Attenuation slope	$\boldsymbol{\beta}$	Constant	2.024 (±0.033)	unitless
Cut-off frequency	$\boldsymbol{f_0}$	Constant	6.598 (±0.035)	decade

RMS cross check

The RMS contributed by noise within the frequency range $[f_1, f_2]$ can be estimated by the PSD:

$$RMS(f_1, f_2) = \sqrt{\int_{f_1}^{f_2} S(f)\mathrm{d}f}. \tag{6.29}$$

Figure 6.35 presents the $RMS(f_1, f_2)$, with $f_1 = 10^{-2}$ Hz, alongside f_2 for the irradiated SiPM with dose $\Phi_{\text{eq}} = 1.55 \times 10^{11}\ \text{n}_{\text{eq}}/\text{cm}^2$. The frequency range [$10^4$ Hz, 10^8 Hz] contributes the majority of the noise, which is dominated by SiPM-specific noise. Additionally, the frequency range [10^{-2} Hz, 10^{-1} Hz] contributes significant noise, dominated by $1/f$ noise.

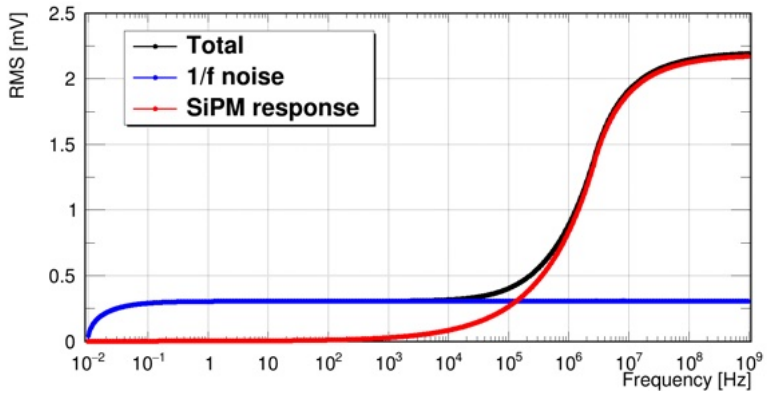

Figure 6.35: RMS estimated by Equation 6.29 with $f_1 = 10^{-2}$ Hz along different f_2 (x-axis). The result indicates that overall RMS is primarily originating from noise in the frequency ranges [10^{-2} Hz,10^{-1} Hz] and [10^4 Hz,10^6 Hz], corresponding to $1/f$ noise and SiPM-specific noise, respectively.

For further verification, the noise RMS was directly measured with the oscilloscope, with $f_1 = 625$Hz. As illustrated in Figure 6.35, the measured RMS is dominated by S_{HFR} which is proportional to the dark current I_{d}. Since $I_{\mathrm{d}} \propto \Phi_{\mathrm{eq}}$, the measured RMS should be proportional to the dose $\sqrt{\Phi_{\mathrm{eq}}}$. Figure 6.36 shows the measured RMS, and the function used for fitting is

$$RMS = \sqrt{RMS_0^2 + RMS_1^2 \cdot \Phi_{\mathrm{eq}}}, \tag{6.30}$$

where RMS_0 represents the intrinsic background noise RMS, and RMS_1 is the RMS coefficient of the radiation dose Φ_{eq}. The obtained RMS_0 and RMS_1 are 0.184(±0.026) and 1.800(±0.011). The good agreement between the data and the fit function further confirms the noise model.

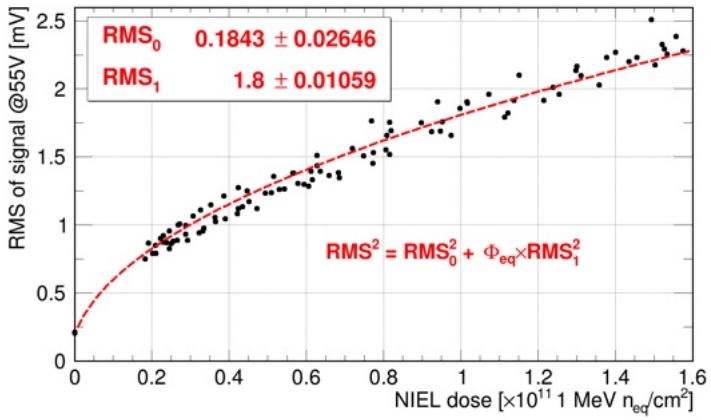

Figure 6.36: Measured RMS with oscilloscope along irradiation dose. The discrepancy between the measurement and fitting curve at the high dose range is due to self-heating caused by the large current in SiPM.

6.2.4 Discussion

The noise PSD reveals more features in the frequency domain that cannot be probed using traditional RMS measurement, providing a deeper understanding of the underlying physics. As anticipated, the noise in the measured frequency range (10^{-2}-10^{8} Hz) is primarily contributed by the noise caused by irradiation damage. However, the mechanisms in different frequency regions are entirely different. The noise in the LFR may be dominated by the fluctuations caused by charge trap/release of defect centers, which exhibit the statistical characteristics of stochastic processes. In contrast, the noise in the HFR is dominated by the low-pass feature of the slow-recovery tail, which displays the time characteristics of single-event responses. Understanding the origin of noise may inspire SiPM design optimization as well as readout electronics design optimization. For example, a SiPM with a shorter tail is expected to have less pile-up, which may lead to higher radiation tolerance in applications like timing detectors where a long tail is not significantly helpful for the application.

Moreover, the employed formula offers a quantitative description of the noise PSD based on the dark current I_{d}, which is determined by the radiation dose Φ_{eq}, temperature T and operation HV. This enables the possibility of estimating the detector's performance under given conditions (Φ_{eq}, T and HV).

6.3 Annealing Study

The three primary mechanisms involved in annealing—migration, formation, and dissociation processes—are temperature-dependent [102]. Consequently, temperature-dependent characterization of annealing is the most common measurement. Additionally, the annealing time feature, determined by the defect annealing rate, and the annealing capability, determined by the annealing capture radius, are widely used to characterize macroscopic annealing properties. In this section, we will obtain the annealing time feature and capability by monitoring the dark current change during annealing at various temperatures. The findings are crucial for the overall design of the Mu3e Tile detector.

6.3.1 Measurements

The same setup as used in the IV scan was employed to perform the annealing measurement. To characterize the temperature dependence, four temperature points, 0 °C, 10 °C, 20 °C and 40 °C, were chosen as the annealing temperatures T_{ann}. The reason for choosing 40 °C as the highest annealing temperature is that the upper limit of operation temperature for the Tile Detector is 60 °C, and the temperature margin is needed for SiPM self-heating. No test below 0 °C was used due to the small annealing capability, long annealing time, and the large measurement uncertainty.

The temperature was measured every 10 s by the temperature sensor on the center of the Tile Detector Matrix, and a part of the monitored temperature for T_{ann} =20 °C is illustrated in Figure 6.37a as example. The IV curve of the SiPMs was measured automatically every 12.7 min, resulting from the scan time of 2.7 min and a time gap of 10 min between two runs. To minimize the SiPM self-heating, the highest HV for the IV scan in the annealing measurement was only set to 57 V. Figure 6.37b shows examples of IV curves during the annealing with T_{ann} =20 °C.

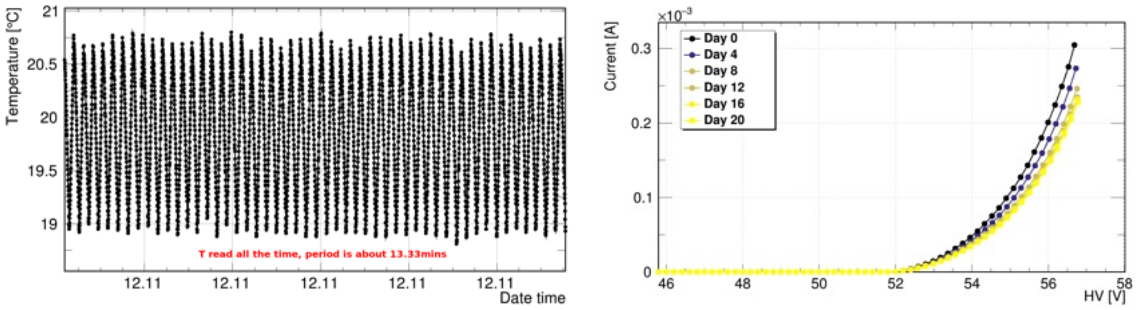

(a) Temperature example in annealing test.

(b) IV curves after different annealing time.

Figure 6.37: Examples of monitored (a) temperature and (b) IV curves during annealing with T_{ann} = 20 °C. (a) Temperature fluctuation is primarily due to the chiller's cooling process. (b) Dark current annealing is evident, with annealing speed decreasing over time.

6.3.2 Analysis and results

Temperature correction

The analysis method used in the IV curve analysis was similarly implemented for the measured IV curve during the annealing process to obtain the dark current at a constant $V_{ov} = 3\,V$[1], and the corresponding curve of I_d versus the annealing time is referred to as annealing curve later. Due to temperature fluctuations, a temperature correction for each annealing curve was performed by correcting the time shift between the time when the IV scan starts and the real-time point when the required V_{ov} reached. As discussed in subsection 6.1.2, the breakdown voltage V_{br} is proportional to the temperature. Therefore, the χ^2 from the linear fit of V_{br} versus temperature was checked at different time delays Δt in the range of 0 and 2.7 min. As shown in Figure 6.38a, the minimal χ^2 is found around $\Delta t = 118\,s$, which is reasonable because the HV was scanned from 0 to 58 V. With the temperature dependence of 54 mV/°C, all the I_d points were corrected to the setting temperature T_{ann}.

Figure 6.38b provides the comparison of I_d before and after temperature correction in the annealing period, indicating that most of the fluctuations due to temperature uncertainty can be excluded after temperature correction.

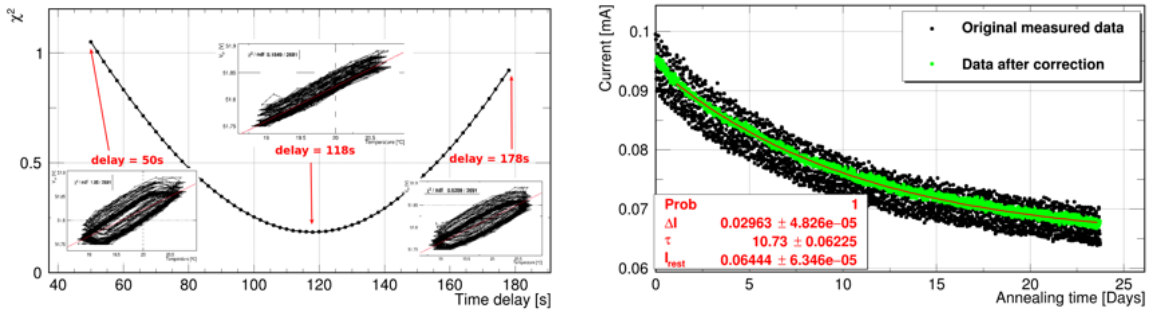

(a) Δt scan for time alignment of temperature data. **(b)** Temperature correction of annealing curve.

Figure 6.38: Temperature correction of dark current with $V_{ov} = 3\,V$. (a) Time alignment is achievable despite unknown absolute temperature in SiPM, as only the temperature difference is needed: $\Delta V_{br} \propto \Delta T$. (b) Most of the current fluctuation due to temperature data misalignment can be excluded by the temperature correction.

Annealing time and capability

Multiple damage defect centers are generated in silicon because the interaction between radiation and silicon atoms is a stochastic process [102]. Therefore, the I_d-based annealing curve is usually described by a sum of exponentials [146]:

$$I_d(t) = \Delta I_{ann} \cdot \sum_i \alpha_i e^{-\frac{t}{\tau_i}} + I_d(t = \infty) \tag{6.31}$$

[1]The rationale behind selecting $V_{ov} = 3\,V$ rather than a higher value is to minimize annealing uncertainty arising from self-heating caused by dark current.

with $\sum_i \alpha_i = 1$. The parameters α_i and τ_i are the relative amplitude and time constant of the i-th defect center, respectively. Moreover, ΔI_{ann} is the annealing capability corresponding to temporary defects, and $I_{\text{d}}(t = \infty)$ is the current when annealing stops or becomes unobservable, corresponding to permanent damage defects, which are both T-dependent. It was reported that $I_{\text{d}}(t = \infty)$ can only be reached after a few months at room temperature [147–149].

Due to limited quantified information on damage defect centers and limited experiment time, the annealing experiment was conducted with a maximum experiment time of 37 days, and a single exponential

$$I(t) = \Delta I \cdot e^{-\frac{t}{\tau}} + I_{\text{rest}} \tag{6.32}$$

was employed to fit the tail of the annealing curves to obtain the I_{rest}, which should be close to $I_{\text{d}}(t = \infty)$. Figure 6.39 illustrates the IV curves with different temperatures and their fitting results with Equation 6.32.

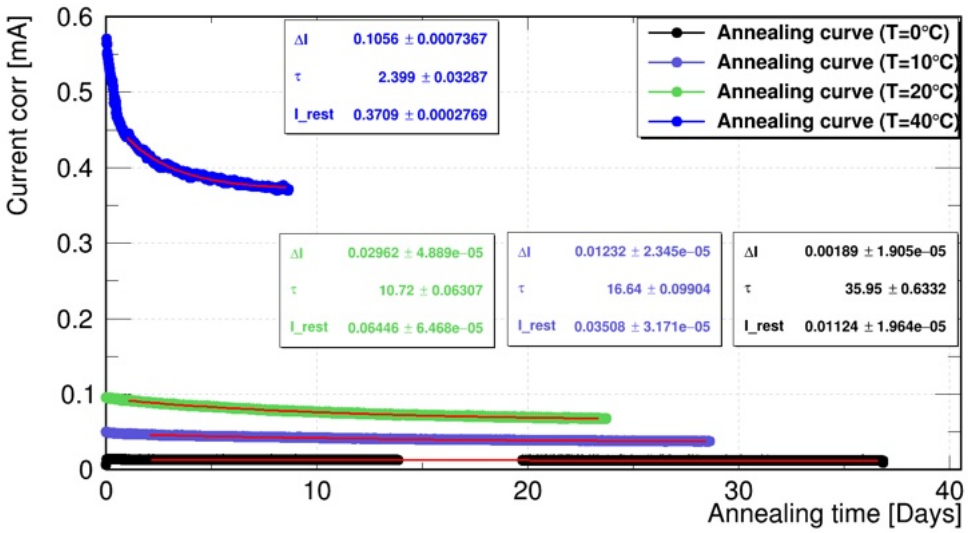

Figure 6.39: Annealing curves at various temperatures fitted with Equation 6.32. The 7-day gap in the annealing curve with $T_{\text{ann}} = 0\,^{\circ}\text{C}$ is due to a temperature reading issue.

The *annealing capability*, η_{ann}, was proposed to quantify the percentage of permanent defect-induced current at a specific temperature, and it can be calculated using

$$\eta_{\text{ann}} = \frac{\Delta I_{\text{ann}}}{I_{\text{d}}(t = 0)} = \frac{I_{\text{d}}(t = 0) - I_{\text{rest}}}{I_{\text{d}}(t = 0)}, \tag{6.33}$$

where $I_{\text{d}}(t = 0)$ is the dark current before annealing and I_{rest} is the current contributed by the permanent defects. With the assumption that both permanent and recoverable defects have a similar dark current coefficient, η_{ann} can be treated as the percentage of recoverable defects produced in the SiPM.

Figure 6.40 illustrates η_{ann} at different temperatures, indicating that the annealing capability increases as temperature increases. The η_{ann} with $T_{\text{ann}} = 40\,^{\circ}\text{C}$ already begins to saturate with a value of 34.31 %.

The time constant τ obtained in Figure 6.39 is not sufficient to characterize the annealing speed. Therefore, an *equivalent time constant*, τ_{eq}, was developed, defined as the time period when the

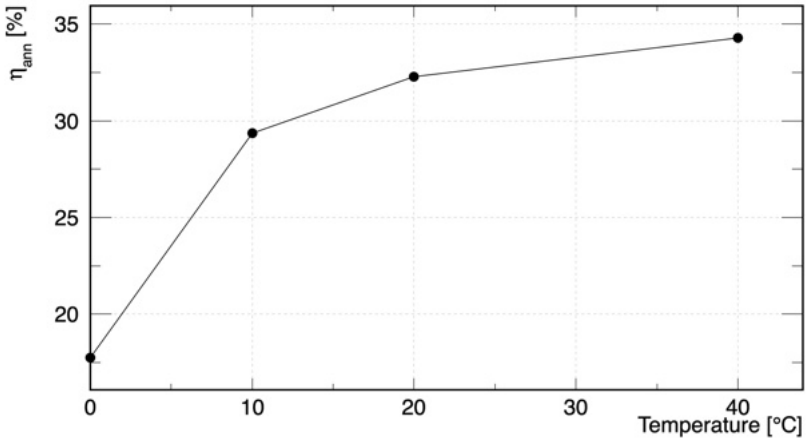

Figure 6.40: Annealing capability η_{ann} at various temperatures. η_{ann} increases as T rises due to enhanced Brownian motion and gradually saturates at $T_{\text{ann}} = 40\,^{\circ}\text{C}$.

remaining recoverable defects reach $1/e$ of the total recoverable defects. τ_{eq} can be calculated by solving

$$I_{\text{d}}(t = \tau_{\text{eq}}) = \frac{1}{e} \cdot \Delta I_{\text{ann}} + I_{\text{d}}(t = \infty) \approx (1 - \frac{e-1}{e} \cdot \eta_{\text{ann}}) \cdot I_{\text{d}}(t = 0). \tag{6.34}$$

Figure 6.41 illustrates the normalized annealing curves at different temperatures, where the $I_{\text{d}}(t = \tau_{\text{eq}})$ (dashed lines) and I_{rest} (solid lines) levels are marked in the plot. The obtained τ_{eq} at different temperatures is plotted in Figure 6.42, showing that τ_{eq} decreases as temperature increases. The τ_{eq} with $T_{\text{ann}} = 40\,^{\circ}\text{C}$ is around 0.94 days.

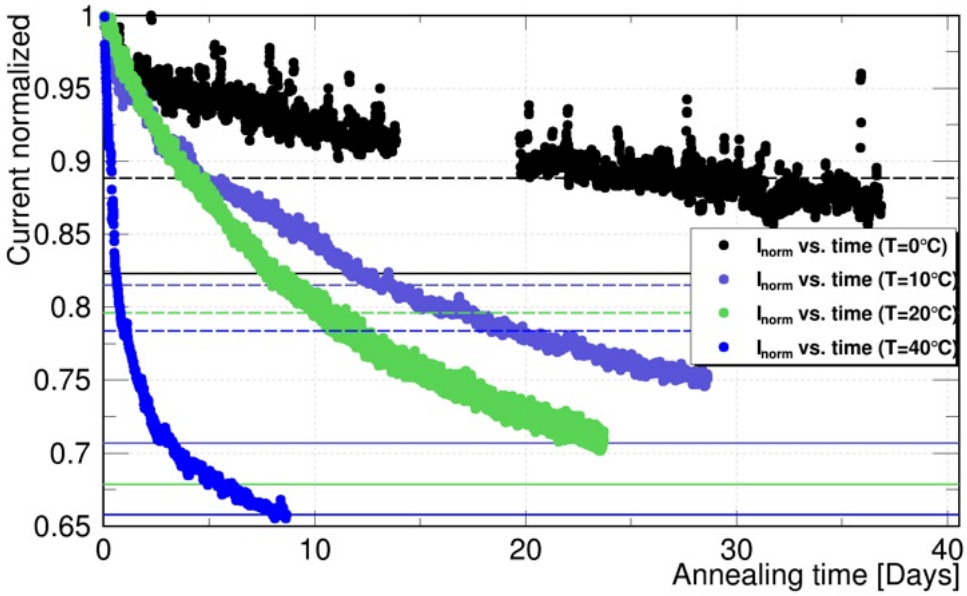

Figure 6.41: Normalized annealing curves with (dashed line) $I_{\text{norm}}(t = \tau_{\text{eq}})$ and (solid line) I_{rest} marked. The annealing curve at the lowest T exhibits the largest relative measurement uncertainty owing to the minimal current.

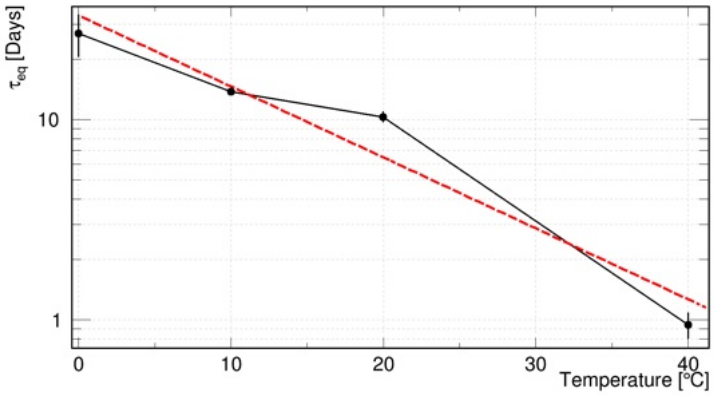

Figure 6.42: τ_{eq} at different annealing temperatures. τ_{eq} depends on I_∞, which is determined by the fitting parameter I_{rest} with the approximation: $I_\infty \approx I_{rest}$. The uncertainty of the T-dependence of I_{rest} primarily contributed from the difference between I_∞ and I_{rest} due to the fitting uncertainty.

6.3.3 Annealing temperature for the Mu3e Tile Detector

An annealing temperature around $T_{ann} = 40\,°C$ is a suitable candidate for the Tile Detector defects annealing during the Mu3e runs due to the following reasons:

- sufficient margin for self-heating to reach the upper operation temperature of 60 °C;
- good annealing capability with $\eta_{ann} = 34.31\,\%$;
- fast annealing speed with an equivalent time constant $\tau_{eq} = 0.94$ days.

Therefore, a more detailed analysis for the annealing curve with $T_{ann} = 40\,°C$ is performed for a more accurate annealing estimation.

Equation 6.31 with different numbers of exponentials was employed to fit the whole annealing curve at $T_{ann} = 40\,°C$, and the function with two exponentials was found to best match the data:

$$I_d(t) = I_{rest} + \Delta I_{fast} \cdot e^{-\frac{t}{\tau_{fast}}} + \Delta I_{slow} \cdot e^{-\frac{t}{\tau_{slow}}}, \tag{6.35}$$

with the relative error smaller than 5 % for all data points, as shown in Figure 6.43.

The annealing process was dominated by fast and slow processes with time constants $\tau_{fast} = 0.69$ days and $\tau_{slow} = 5.72$ days. Moreover, the current recovered due to these two processes are $\Delta I_{fast} = 0.129$ mA and $\Delta I_{slow} = 0.076$ mA, indicating that the fast annealing process has a more significant contribution compared to the slow process. Furthermore, the sum of ΔI_{fast} and ΔI_{slow} is equivalent to the ΔI_{ann} in Equation 6.31, which results in an annealing capability of

$$\eta_{ann} = \frac{\Delta I_{ann}}{I_d(t=0)} = \frac{\Delta I_{fast} + \Delta I_{slow}}{I_d(t=0)} = 37.29\,\%. \tag{6.36}$$

The η_{ann} here is approximately 3 % higher than the result obtained from the single-exponential fit, mainly due to the uncertainty of the single-exponential fit.

In Equation 6.35, the current-related variables and parameters ($I_d(t)$, ΔI_{fast} and ΔI_{slow}) are not only temperature-dependent but also V_{ov} dependent. To exclude the dependence on V_{ov}, Equation 6.35 can

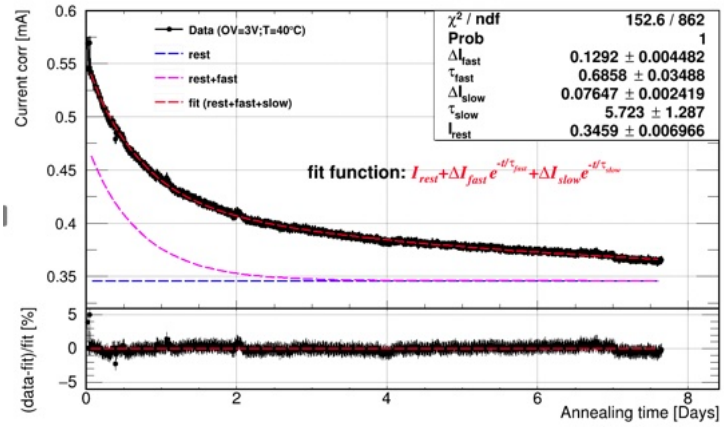

Figure 6.43: Annealing curves at $T_{\text{ann}} = 40\,^{\circ}\text{C}$ fitted with Equation 6.35. The fitting result demonstrates that Equation 6.35 adequately describes the annealing curve at $T_{\text{ann}} = 40\,^{\circ}\text{C}$ with the largest error $< 5\,\%$. Furthermore, the annealing contribution from the fast process surpasses that of the slow process.

be rewritten in a normalized form

$$\begin{aligned}\xi_{\text{ann}}(t) &= \frac{I_{\text{d}}(t)}{I_{\text{d}}(t=0)} \\ &= \frac{1}{I_{\text{d}}(t=0)} \cdot (I_{\text{rest}} + \Delta I_{\text{fast}} \cdot e^{-\frac{t}{\tau_{\text{fast}}}} + \Delta I_{\text{slow}} \cdot e^{-\frac{t}{\tau_{\text{slow}}}}) \\ &= (1 - \eta_{\text{fast}} - \eta_{\text{slow}}) + \eta_{\text{fast}} \cdot e^{-\frac{t}{\tau_{\text{fast}}}} + \eta_{\text{slow}} \cdot e^{-\frac{t}{\tau_{\text{slow}}}} \\ &= 1 - \eta_{\text{fast}} \cdot (1 - e^{-\frac{t}{\tau_{\text{fast}}}}) - \eta_{\text{slow}} \cdot (1 - e^{-\frac{t}{\tau_{\text{slow}}}}),\end{aligned} \tag{6.37}$$

where

$$\eta_{\text{fast}} = \frac{\Delta I_{\text{fast}}}{I_{\text{d}}(t=0)} \quad \text{and} \quad \eta_{\text{slow}} = \frac{\Delta I_{\text{slow}}}{I_{\text{d}}(t=0)}. \tag{6.38}$$

Table 6.8 lists all the parameters for the normalized equation based on the fitting results obtained from the annealing curve at $T_{\text{ann}} = 40\,^{\circ}\text{C}$, based on which 30 % of the dark current is vanished in around 3 days. All the parameters here are only T-dependent because the distribution of defect centers is fixed due to the same radiation field. Due to the similar radiation field in the real Mu3e experiment runs, the parameters should remain the same if setting the annealing temperature to 40 °C. Therefore, the parameters can be employed for later annealing prediction in the real Mu3e experiment.

Table 6.8: Parameters for Equation 6.37 obtained from normalized annealing curve with $T_{\text{ann}} = 40\,^{\circ}\text{C}$. Those parameters can be used directly in later annealing estimation with $T_{\text{ann}} = 40\,^{\circ}\text{C}$ because it is not bias voltage dependent.

Parameter	Symbol	value	unit
Annealing capability (fast)	η_{fast}	23.4 (±00.9)	%
Annealing time constant (fast)	τ_{fast}	0.686 (±0.035)	day
Annealing capability (slow)	η_{slow}	13.9 (±00.5)	%
Annealing time constant (slow)	τ_{slow}	5.723 (±1.287)	day

Chapter 7

Timing and Efficiency Characterization

In this chapter, a comprehensive analysis of the timing and efficiency characterization of the Tile Detector is presented. This chapter summarizes the key parameters for both timing and efficiency performance, followed by an examination of the detector's performance under various radiation doses during a beam-test campaign at DESY, Hamburg. Additionally, an in-depth analysis and discussion of the radiation impact is provided, along with suggestions for performance optimization of the Tile Detector after radiation damage.

7.1 Timing and Radiation Impact

The timing resolution is a critical requirement for the Tile Detector in the Mu3e experiment. Since both the general and the Mu3e-specific timing resolution have been extensively studied previously [4, 83, 150–157], this section will provide a concise summary of the timing resolution. Additionally, the impact of radiation on the timing resolution will be discussed.

7.1.1 Timestamp extraction techniques

Leading-edge discrimination is a prevalent technique for timestamp extraction in signal processing (Figure 7.1), particularly in fast-signal detectors like the Tile Detector. This method identifies the point where the signal's leading edge surpasses a predetermined threshold. However, the time-walk effect, which arises from varying leading edge slopes for signals with different amplitudes, can introduce timing inaccuracies. A time-walk correction, which compensates for the time delay among various signals reaching the threshold, is applied to enhance the overall timing resolution of the system.

7.1.2 Contributors to the timing resolution

In detectors employing SiPMs and plastic scintillators, such as the Tile Detector, several factors contribute to the overall timing resolution. This section discusses three primary contributors: vertical noise, photon statistics, and avalanche jitter, which were identified as the most significant contributors to the Tile Detector's timing resolution [4].

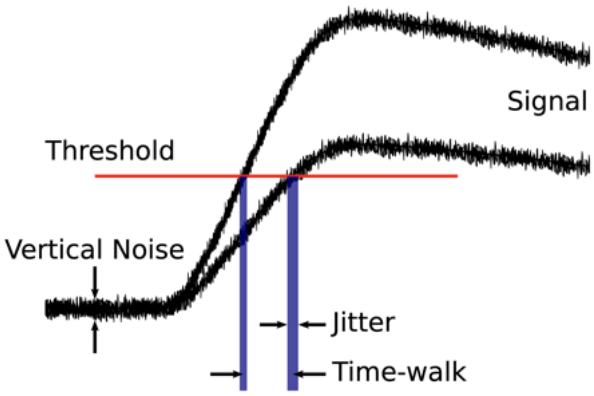

Figure 7.1: Schematic of the leading-edge discrimination technique for timestamp extraction in Tile Detector signal. The time-walk effect arises from varying leading-edge slopes for signals with different amplitudes, and the time difference, Δt_{tw}, needs to be corrected for the time delay among different signals as they reach the fixed threshold. The timing jitter contributes by the vertical noise. It is related to both the vertical noise amplitude and the signal slope when reaching the threshold.

Vertical noise

Vertical noise is a major contributor to the timing uncertainty in SiPM-based detectors. It arises from the electronic noise in the detector system, particularly at the input stage of the readout electronics. This noise can affect timestamp extraction, especially when using leading-edge discrimination techniques, by increasing the uncertainty in the threshold-crossing time. The timing jitter contributed by vertical noise can be expressed as:

$$\sigma_{\text{en}} = \frac{\sigma_{\text{noise}}}{\mathrm{d}V/\mathrm{d}t}, \tag{7.1}$$

where σ_{noise} is the vertical noise amplitude, and $\mathrm{d}V/\mathrm{d}t$ is the signal slope at the threshold crossing point.

Photon statistics

Photon statistics also plays a crucial role in determining the timing resolution of detectors with SiPMs and plastic scintillators. The number of photons produced in the scintillator and subsequently detected by the SiPM can vary from event to event, introducing fluctuations in the arrival time of these photons. The statistical nature of this process leads to uncertainties in timestamp extraction, and the timing jitter due to photon statistics follows:

$$\sigma_{t_{\text{photon}}} \propto \frac{1}{\sqrt{N_{\text{photon}}}}, \tag{7.2}$$

where N_{photon} is the number of detected photons. Enhancing light collection efficiency and optimizing the coupling between the scintillator and the SiPM can improve the timing resolution by increasing the number of detected photons and reducing statistical fluctuations. This motivated the individual tile wrapping.

A GEANT4 simulation for the Tile used in the Mu3e Tile Detector was conducted with general settings introduced in [4], where the new design discussed in subsection 3.3.3 was implemented. Figure 7.2a displays the energy deposited in the Tile, and Figure 7.2b shows the corresponding number of photons

arriving at the SiPM surface. The Most-Probable-Value (MPV) value of the number of photons arriving at the SiPM surface, N_{arrive}, is around 3500, and with an overall efficiency $\epsilon_{\text{all}} = 34.84\,\%$, the MPV of the number of detected photons, N_{detected}, is approximately 1000.

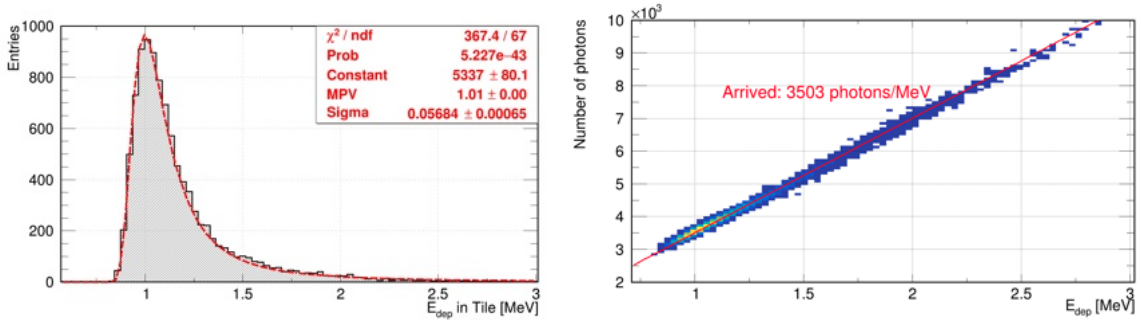

(a) E_{dep} in the Tile Detector scintillator. **(b)** Number of photons vs. E_{dep}.

Figure 7.2: GEANT4 simulation results of energy deposited in scintillator and photons arriving at the SiPM surface based on the Mu3e Tile Detector design. (a) The energy spectrum is fitted with a Landau function to obtain MPV and sigma. (b) The number of photons arriving at the SiPM surface is proportional to the energy deposited, and the corresponding MPV for the number of photons arriving is around 3504 photons.

The timing resolution also depends on the time distribution of photon generation. A faster photon-generation mechanism will deliver a more concentrated distribution in time, leading to smaller time jitter, which is the motivation for choosing the fast scintillator EJ228 with a rise time of 0.5 ns for photon generation. The time distribution of the photons arriving at the SiPM surface obtained from the simulation is shown in Figure 7.3. And Figure 7.4a illustrates the timing distribution of i-th arriving the SiPM surface, and the standard deviation of the time distribution is plotted in Figure 7.4b, which indicates that the earlier the photon arrive the SiPM the smaller timing jitter will be given.

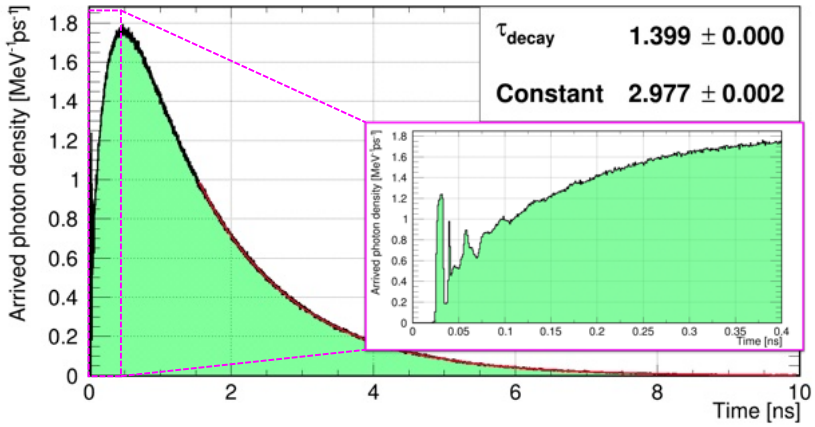

Figure 7.3: Photon density of the scintillator Tile used in the Mu3e Tile Detector from a GEANT4 simulation. The time zero is the time point when the particle hits the Tile. The peak at the beginning is the Cherenkov photon peak, which is produced immediately once the electron's speed in the Tile is greater than the phase velocity of light, resulting in a narrow distribution in time.

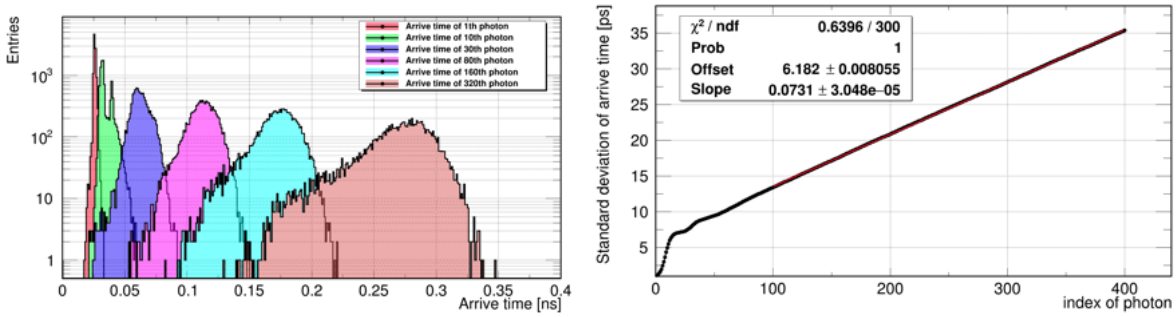

(a) Arrival time of i-th photon.

(b) Standard deviation of the i-th arrival time.

Figure 7.4: Time information of photons arriving at the SiPM surface. (b) The small deviation at the very beginning is due to the narrow time distribution of the Cherenkov photons.

Avalanche jitter

Avalanche jitter is another contributor to the timing uncertainty in SiPM-based detectors. It arises from the inherent variability in the time it takes for a photo-generated carrier to initiate an avalanche in the SiPM pixel. This variability can cause fluctuations in the measured arrival time of photons, affecting the overall timing resolution. The timing jitter due to avalanche jitter is Excess Noise Factor (ENF) dependent:

$$\sigma_{t_{\text{av}}} \propto \sqrt{\text{ENF}}. \tag{7.3}$$

Reducing avalanche jitter requires optimizing the SiPM's design, such as using advanced SiPM structures with faster response times and lower excess noise factors, to minimize the impact of this jitter on the detector's timing performance. However, the overall contribution of avalanche jitter is photon number dependent as well:

$$\sigma_{t_{\text{av}}}^{\text{all}} \propto \frac{\sigma_{t_{\text{av}}}}{\sqrt{N_{\text{photon}}}}. \tag{7.4}$$

Consequently, the $\sigma_{t_{\text{av}}}^{\text{all}}$ can be quite small with a large N_{photon}.

In the Tile Detector design, a threshold at around a few photon levels was chosen as the threshold where the best timing resolution was found [4]. An average single-channel timing resolution of $\bar{\sigma} \approx 47$ ps was achieved in the beam-test at DESY with the technical prototype read out by MuTRiG [91], which reached the target timing resolution for the Tile Detector of <100 ps.

7.1.3 Radiation impact

Radiation impact on the Tile primarily results in a reduction of the number of photons by a factor of less than 10 %. Due to the large number of photons produced by the Tile, the change in photon statistics is not expected to significantly degrade the timing resolution.

In contrast, the radiation impact on the SiPM may lead to substantial timing resolution degradation. Firstly, the increase in the DCR results in larger fluctuations in the baseline. Secondly, changes in electronic parameters (breakdown voltage, quenching resistor, etc.) may lead to smaller or slower signals. Moreover, the dramatic increase in dark current I_{d} also leads to a shift of the absolute threshold to a higher level, which may not directly impact the timing resolution but bring in new readout electronic

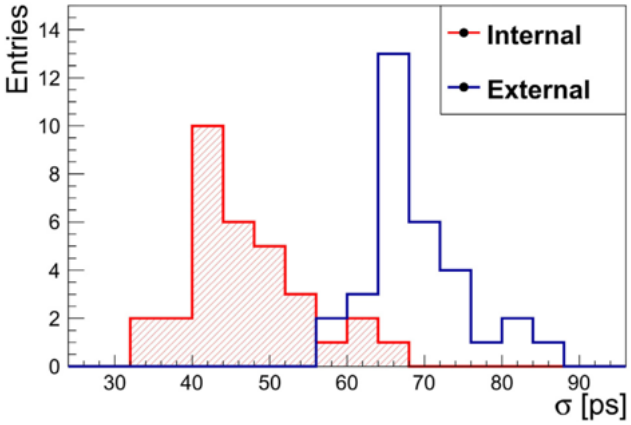

Figure 7.5: Timing resolution measured from the Tile Detector prototype with full Tile Detector readout electronics. The "Internal" timing resolution is the resolution measured using the channels in the same Matrix as the reference channels, and the "External" timing resolution is the resolution with channels from different Matrices as the reference channels. The difference is mainly from the extra jitter from the electronics of the system.

requirements. Characterization of the SiPMs after radiation exposure equivalent to the Mu3e dose level revealed no significant change in the SiPM basic parameters. In contrast, a significant increase in vertical noise was found, which dominates the time jitter at low threshold ranges where the signal slope $\mathrm{d}V/\mathrm{d}t$ is small, leading to a new optimal threshold at a higher level.

7.2 Timing Beam-test Campaign

To characterize the timing performance of the irradiated Tile Detector Matrices in a realistic environment, measurements at the DESY electron beam test facility were conducted with a 3 GeV electron beam.

7.2.1 Setup and measurements

Figure 7.6 illustrates the setup used for the beam-test campaign at DESY. Two Tile Detector Matrices connected to the same adapter board were mounted on an aluminum block cooled with water at around 10 °C to minimize temperature uncertainty from self-heating. The temperatures on both Matrices were monitored by a temperature sensor mounted at the center of the Matrices. "Port 1" on the adapter board was sequentially connected to the Matrices being tested, which consisted of six irradiated Matrices and one non-irradiated Matrix. The non-irradiated Matrix was employed for performance comparison. In contrast, the "Port 2" was connected to another non-irradiated Matrix as a timestamp reference, providing a reference timestamp for the Matrix being tested. Furthermore, Matrices connected to both ports were aligned to the beam direction with a laser alignment system to maximize the probability that one particle passed through all eight Tiles in the same row.

The reference Matrix connected to Port 2 was biased by a voltage of 55 V to provide reasonable timing resolution. To maintain a constant bias voltage on different Matrices connected to Port 1,

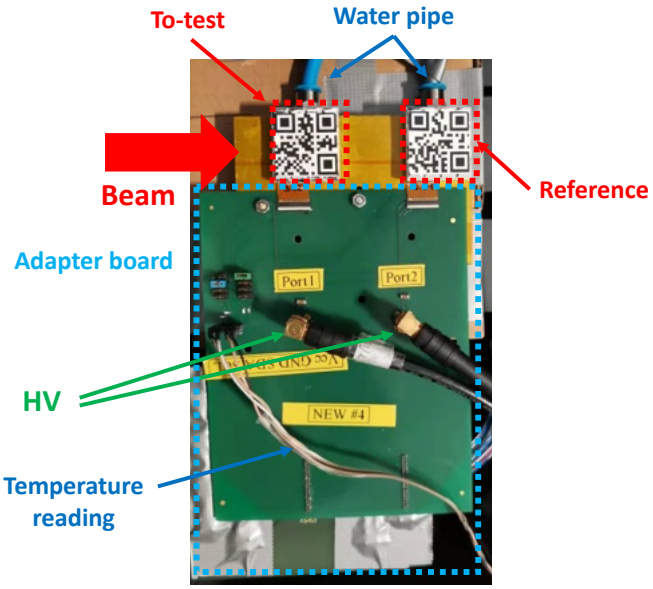

Figure 7.6: Timing performance test setup used in DESY beam-test campaign. Both Matrices are mounted on the Al block cooled with water at 10 °C to maintain a constant temperature used in the in-lab characterization.

various voltages were applied based on the dark current for each Matrix. The corrected voltage V_{SiPM} was set to 55 V, equivalent to $V_{\mathrm{ov}} = 3.7$ V. Figure 7.7 illustrates the V_{SiPM} for all Matrices connected to Port 1, with $V_{\mathrm{SiPM}} - 55\ \mathrm{V} < 100$ mV.

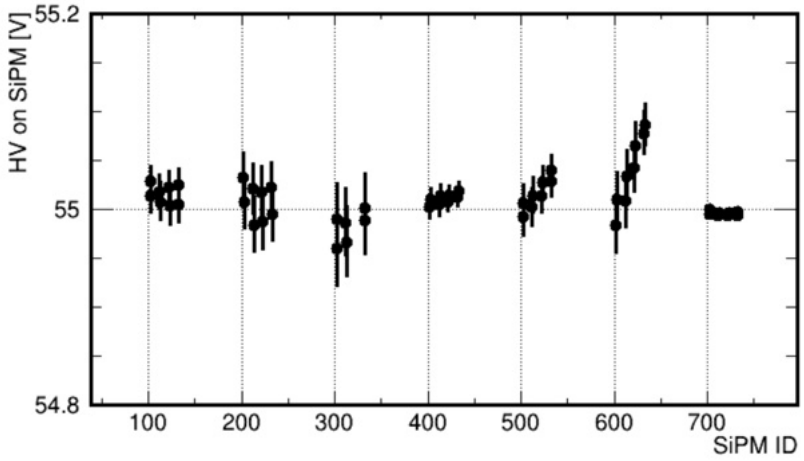

Figure 7.7: V_{SiPM} for all the measured SiPMs in the Matrices connected to Port 1. The SiPM ID $ID_{\mathrm{SiPM}} = ID_{\mathrm{Matrix}} \times 100 + ID_{\mathrm{local}}$. The Matrix ID ID_{Matrix} is the ID illustrated in Figure 5.5 and the non-irradiated Matrix connected to Port 1 was assigned to $ID_{\mathrm{Matrix}} = 7$. The local ID ID_{local} is identical for all the channels at the same local position in the Matrix. The difference in V_{SiPM} in the same Matrix mainly comes from the correction $I_{\mathrm{d}} \cdot R_0$, where the I_{d} is different due to different dose.

Additionally, the signals from the adapter board were fed into the oscilloscope LeCroy WaveRunner 610Zi, where the DC50 mode was employed to read out the SiPM's waveforms. MuTRiG was not used for signal reading due to its timing threshold being incapable of handling the signal after irradiation,

which will be discussed in detail in Chapter 8. Figure 7.8a illustrates the connection schematic for reading out the four channels in row 3. Channels in the first and last columns were chosen as reference channels ("R1" and "R2" marked in Figure 7.8a), serving not only for event selection but also as timestamp references.

To suppress fake event signals, such as optical cross-talk and noise, the threshold in both reference channels was set to 100 mV, increasing the probability that particles passed through all eight Tiles. The upper limit of signals from reference channels was set to 160 mV in the oscilloscope, representing a compromise between sampling precision and range. Two channels between R1 and R2 in the same row were selected as test channels ("T1" and "T2" marked in Figure 7.8a), with scales set to 40 mV to achieve better sampling resolution of the signal amplitude.

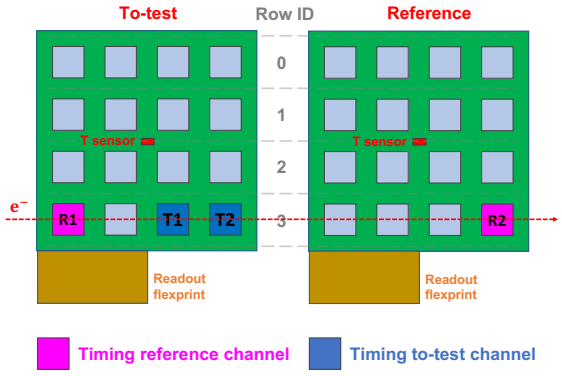

(a) Schematic of Matrix channels.

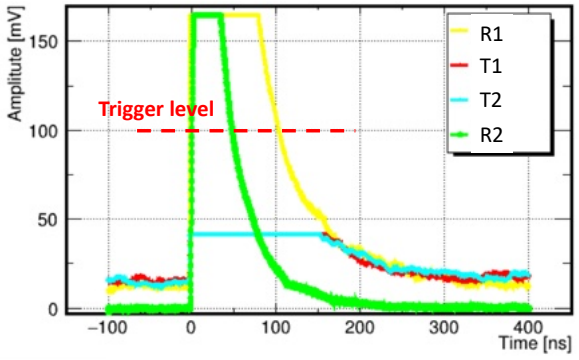

(b) Waveform examples of SiPM signals.

Figure 7.8: Matrix channels and signal examples in the beam-test. (a) The two Matrices in the electron beam was grouped into 4 rows and each row is aligned to the direction of the beam to increase the probability that a particle go through all eight Tiles in the same row. And the first and last channel in each row was employed as the reference channels, R1 and R2, and two channels in each row between R1 and R2 were chosen as the channels for performance studies, marking as T1 and T2. The waveform examples from all four channels with true events were given in (b).

Furthermore, waveforms from all four channels were read out only when signals in both R1 and R2 were above the trigger threshold. To ensure precise timing measurements, a time range of 500 ns, from −100 ns to 400 ns relative to the trigger time, was monitored at a sampling rate of 10 GS/s. Over 10,000 events were read for each run to obtain sufficient statistics.

7.2.2 Analysis and results

Timing resolution extraction

The *Coincidence Time Resolution* (CTR) $\sigma_{(i-j)}$ between channel i and j can be obtained from the distribution of time difference: $\Delta t_{(i-j)} = t_i - t_j$. Figure 7.9 presents an example of the $\Delta t_{(i-j)}$ distribution for two channels, where $\sigma_{(i-j)}$ is defined as the value of the parameter σ in the Gaussian function used for fitting. $\sigma_{(i-j)}$ encompasses the individual timing resolutions σ_i and σ_j:

$$\sigma^2_{(i-j)} = \sigma^2_i + \sigma^2_j. \tag{7.5}$$

Consequently, using R1 and R2 as reference channels, the timing resolution of channels T1 and T2 can be calculated based on

$$\sigma_{\mathrm{T}i} = \sqrt{\sigma^2_{(\mathrm{T}i-\mathrm{R1})} + \sigma^2_{(\mathrm{T}i-\mathrm{R2})} - \sigma^2_{(\mathrm{R1}-\mathrm{R2})}}, \tag{7.6}$$

where $i = 1, 2$ is the index T1 and T2.

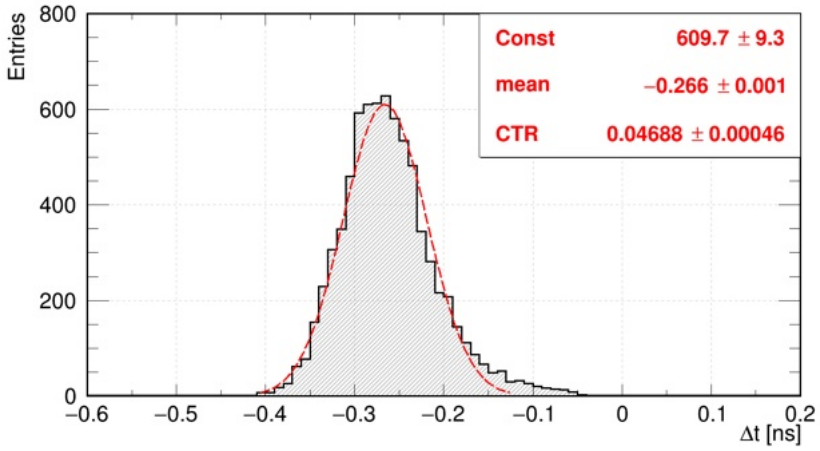

Figure 7.9: Time difference distribution example. The Gaussian function was employed to fit the distribution, and $\sigma_{(i-j)}$ was defined as the parameter σ in the Gaussian function.

ToT for noise filtering and time-walk correction

In the Tile Detector , ToT serves as energy information used for both time-walk correction and noise filtering. To minimize signal tail fluctuations, the ToT of measured waveforms from all channels was obtained with a threshold of 40 mV (see Figure 7.10a). Figure 7.10b illustrates the ToT distribution of R1, which was fitted with the Landau function to obtain the MPV μ_{ToT} and sigma σ_{ToT}.

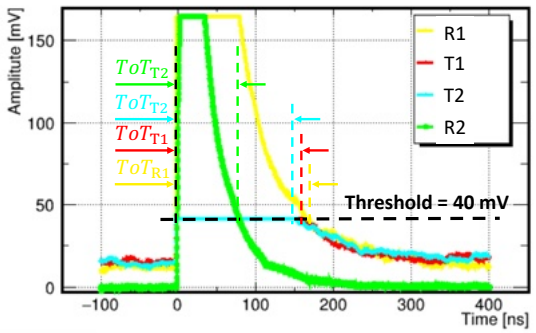

(a) ToT extraction.

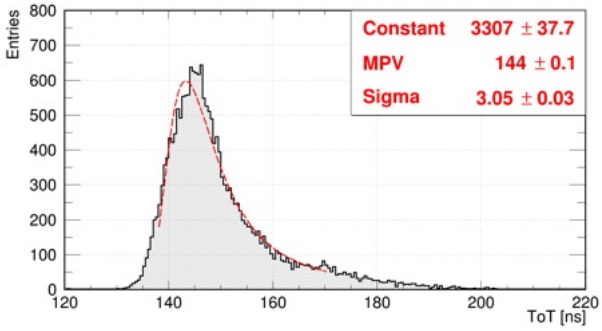

(b) ToT example fitted with Landau function.

Figure 7.10: Examples of ToT extraction and result with threshold of 40 mV.

A ToT filter, $\mu_{\mathrm{ToT}} - 1.5 \cdot \sigma_{\mathrm{ToT}} < ToT < \mu_{\mathrm{ToT}} + 3.5 \cdot \sigma_{\mathrm{ToT}}$, was applied to reference channels R1 and R2 to suppress fake events. A narrower ToT distribution in reference channels provides smaller σ_{R1} and σ_{R2} due to minimized time-walk effects. Therefore, the time-walk correction is only needed for T1 and T2. Figure 7.11 compares the ToT distribution of R1 and T1 before and after filtering.

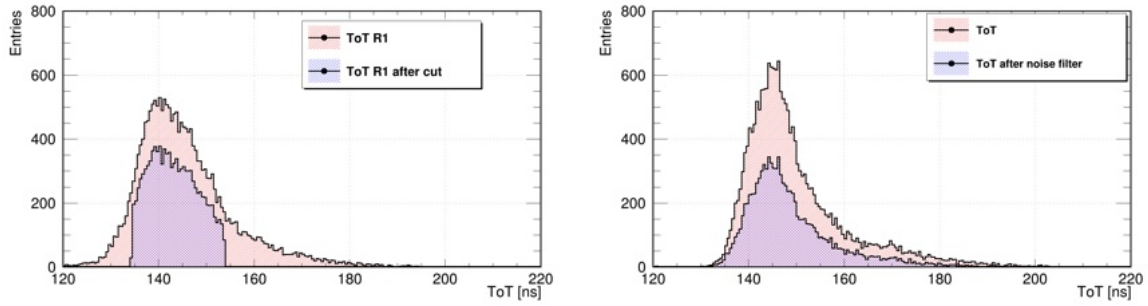

(a) ToT spectrum of R1.

(b) ToT spectrum of T1.

Figure 7.11: Comparison of ToT in channel (a) R1 and (b) T1 before and after the ToT filter implementation. (a) The sharp edge in the distribution after filter is due to the cut in R1 and the missing events within the range $[\mu_{\mathrm{ToT}} - 1.5 \cdot \sigma_{\mathrm{ToT}}, \mu_{\mathrm{ToT}} + 3.5 \cdot \sigma_{\mathrm{ToT}}]$ were filtered out by the ToT filter in channel R2. (b) No direct cut was implemented on T1 and T2 to preserve all the timing jitter contribution from different E_{dep}.

The time-walk correction for T1 and T2 was performed by correcting the Δt between them and the reference channels. The correction is determined from the energy dependence of the measured time difference $\Delta t(ToT_{\mathrm{T1/2}}) = t_{\mathrm{R1/2}} - t_{\mathrm{T1/2}}(ToT_{\mathrm{T1/2}})$, exemplified in Figure 7.12a. This distribution is fitted with a linear function

$$f_{\mathrm{tw}}(ToT_{\mathrm{T1/2}}) = a \cdot ToT_{\mathrm{T1/2}} + b, \tag{7.7}$$

with parameters a and b. The corresponding correction value for $\Delta t(ToT_{\mathrm{T1/2}})$ is

$$\delta t_{\mathrm{tw}}(ToT_{\mathrm{T1/2}}) = \Delta t(ToT_{\mathrm{T1/2}}) - f_{\mathrm{tw}}(ToT_{\mathrm{T1/2}}). \tag{7.8}$$

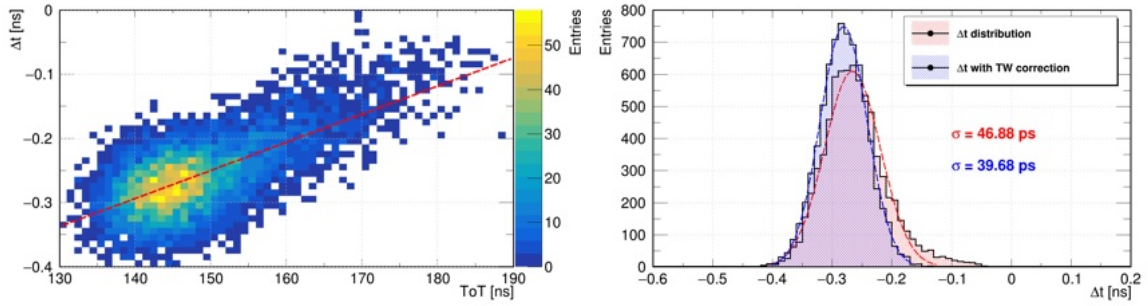

(a) Correlation between Δt and ToT.

(b) Δt before/after time-walk correction

Figure 7.12: Time-walk effect and correction. (a) Δt is ToT-dependent, resulting in a larger timing resolution, which is called the time-walk effect. The time-walk correction was performed with a linear function fitted to the distribution.

Figure 7.12b demonstrates the CTR before and after time-walk correction, where the time resolution improves from 46.88 ps to 39.68 ps with 24.96 ps of time-walk effects excluded. Figure 7.13 plots the timing resolution at various thresholds, agreeing with the expectation that the time-walk effect becomes more dominant at higher thresholds.

The threshold values mentioned above are absolute thresholds concerning the analog system's ground.

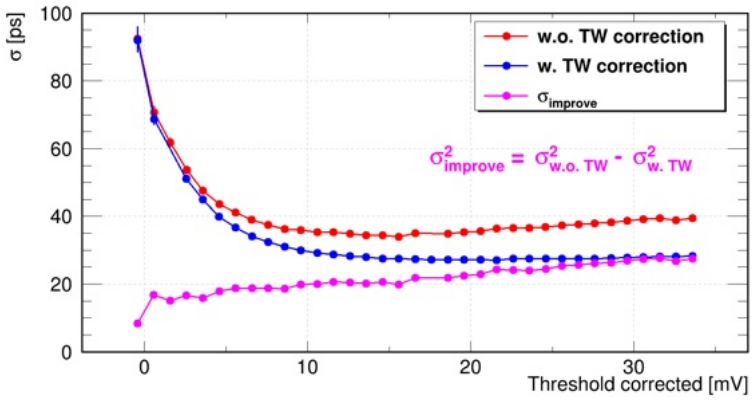

Figure 7.13: Timing resolution along the threshold before and after time-walk correction. The result aligns with the expectation that the time-walk effect is more dominated at higher timing thresholds.

However, the relative threshold with reference to the signal baseline is more meaningful when comparing timing performance at different doses, as the signal baseline of irradiated SiPMs significantly increases. Therefore, all timing thresholds discussed in the timing resolution characterization part are relative thresholds related to the corresponding signal baseline unless specifically stated. The baseline was extracted from the data in the time range [−100 ns, −20 ns], as an example is given in Figure 7.14.

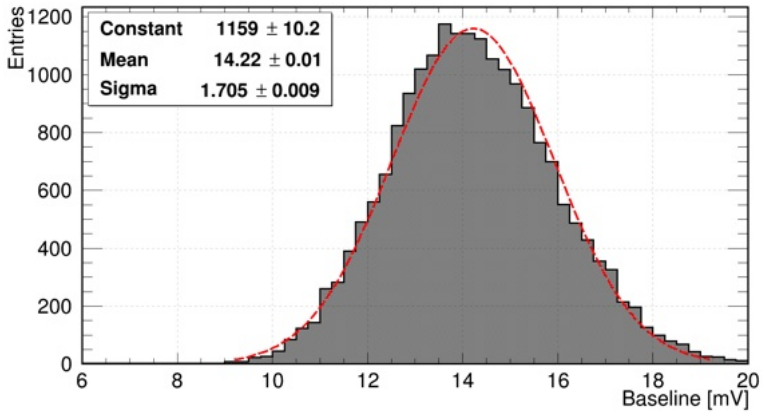

Figure 7.14: Signal baseline obtained in the range of [−100 ns, −20 ns]. The mean value was utilized to determine the relative threshold.

Results and discussion

To minimize interference from the measurement system's differences, all T1 channels in row 0 were selected as examples to discuss timing performance in this section. Figure 7.15a shows the positions of these channels in the irradiated Matrices: Matrix 1-6, and the same channel in the non-irradiated Matrix was used for comparison. The timing resolution of the seven channels with different timing thresholds is plotted in Figure 7.15b.

It is evident that the timing resolution degrades as the dose increases. Significant degradation is observed in the low threshold range, where the vertical noise σ_{noise} in SiPM dominates the timing

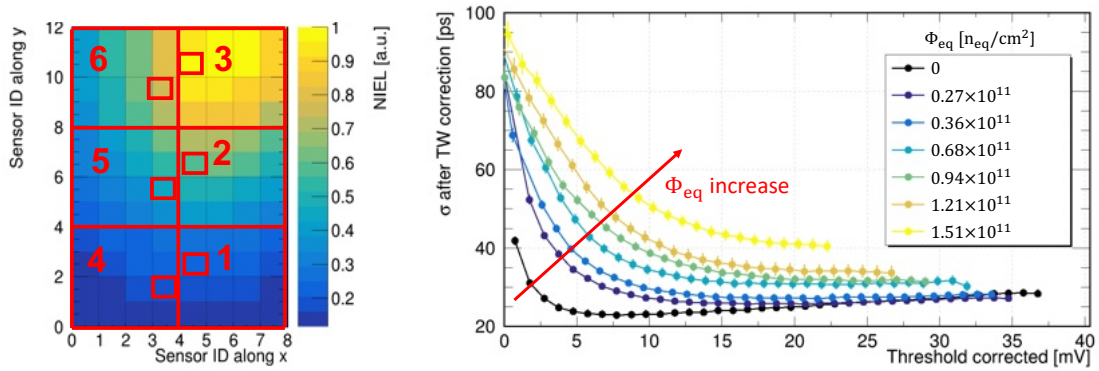

(a) Positions of the channels. **(b)** Timing resolution along threshold with different doses.

Figure 7.15: Positions and timing resolution of T1 in row 0. (a) The positions of the channels in Matrix 1-6 were marked in the dose distribution. All six channels, along with the same channel in Matrix 7, are read out by the same electronics and the same channel in the oscilloscope, excluding most of the extra jitter from the measurement system. (b) The timing resolution degrades significantly in the low threshold range, while the situation in the high threshold range is much better.

resolution because vertical noise dramatically increases with increasing radiation dose. In contrast, degradation in the high threshold range is smaller due to the higher signal slope dV/dt, as shown in Figure 7.16.

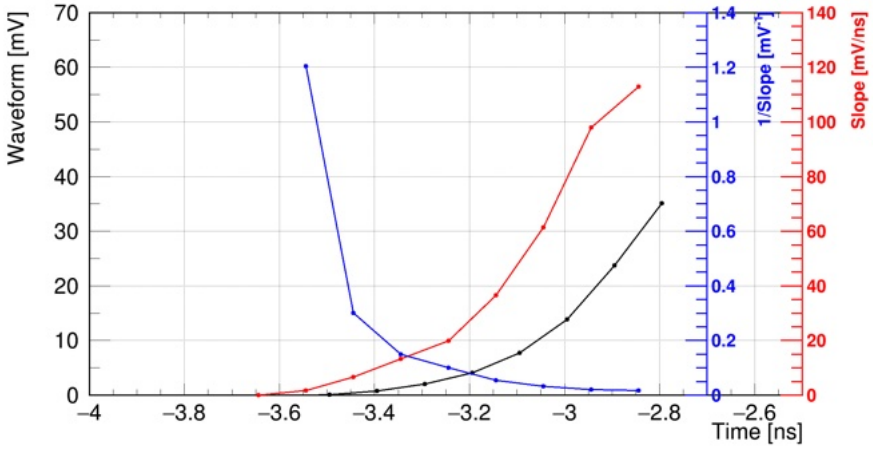

Figure 7.16: Leading edge of SiPM signal and its slope. The slope (red) of the waveform grows exponentially due to the exponential increase of the leading edge (black).

The original timing threshold designed for the Tile Detector is equivalent to around 5 mV, where the best timing resolution is found in the non-irradiated channel. Figure 7.17 displays the timing resolution of different doses with timing thresholds of 5 mV (σ_{5mV}) and 15 mV (σ_{15mV}). σ_{5mV} is smaller than σ_{15mV} for non-irradiated channels because σ_{15mV} involves more photon statistic-related jitter. However, σ_{5mV} is clearly larger than the σ_{15mV} when the radiation dose exceeds 0.2×10^{11} n_{eq}/cm^2, which is due to the timing jitter contribution from the vertical noise that starts dominating the timing resolution in the lower threshold.

Additionally, variations in timing resolution at the same dose were observed within both σ_{5mV} and

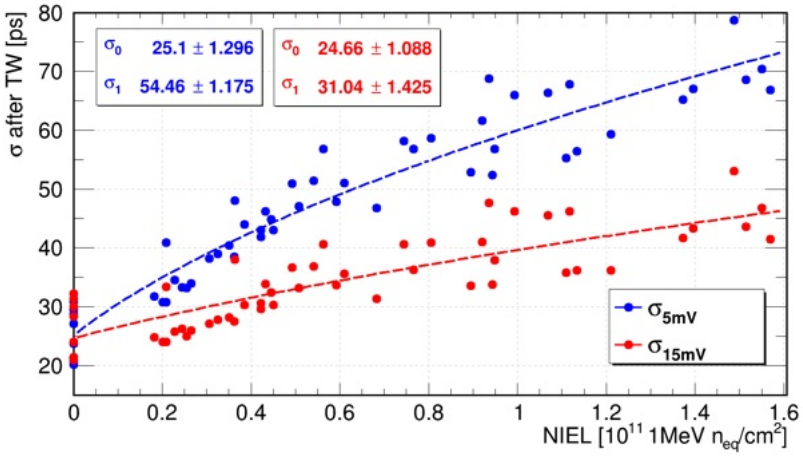

Figure 7.17: Timing resolution degradation of σ_{5mV} (blue) and σ_{15mV} (red) along radiation dose. Both σ_{5mV} and σ_{15mV} degrade with increasing dose due to the dramatic increase in vertical noise from the SiPM. However, σ_{15mV} is more robust to radiation damage due to a higher slope to suppress the timing jitter contributed by the vertical noise.

σ_{15mV}, stemming from the influence of other factors, such as readout electronics differences, channel performance disparities, temperature uncertainty, difference in time-walk effects, and dose estimation uncertainty. Nonetheless, the data is sufficient to conclude that σ_{15mV} is better than σ_{5mV} for a Tile Detector channel with an exposure dose higher than 0.2×10^{11} n_{eq}/cm^2.

The timing resolution degradation with increasing dose is dominated by the vertical noise caused by radiation damage, primarily due to the significant increase in DCR. Consequently, σ_{noise} should also adhere to the square-root law in Equation 6.30. Further quantitative analysis was conducted by fitting the timing resolution σ with

$$\sigma(\Phi_{eq}) = \sqrt{\sigma_0^2 + \Phi_{eq} \times \sigma_1^2}. \tag{7.9}$$

σ_0 represents the intrinsic timing resolution without radiation damage, while σ_1 is the additional timing resolution coefficient of the radiation dose. Figure 7.17 displays the fitting results for both σ_{5mV} and σ_{15mV}.

From the σ_{5mV} curve, σ_0 and σ_1 are 25.1 ps and 54.46 ps, respectively, indicating that σ_{5mV} is approximately 25.1 ps for non-irradiated channels, with an extra timing jitter of 54.46 ps added when the dose increases by 10^{11} n_{eq}/cm^2. The worst timing resolution at the end of the Mu3e experiment can be estimated as

$$\sigma_{5mV}(\Phi_{eq} = 2.23 \times 10^{11}\ n_{eq}/cm^2) = 85.11\ ps. \tag{7.10}$$

Although σ_{15mV} for non-irradiated channels is larger than the corresponding σ_{5mV}, a smaller $\sigma_0 = 24.66$ ps was acquired in the σ_{15mV} curve due to fitting uncertainty. Nevertheless, this minor difference does not affect the final outcome of the radiation damage study. In contrast, a much smaller $\sigma_1 = 31.04$ ps was obtained in the σ_{15mV}, indicating that σ_{15mV} is more robust to radiation damage, with an expected timing resolution of

$$\sigma_{15mV}(\Phi_{eq} = 2.23 \times 10^{11}\ n_{eq}/cm^2) = 52.50\ ps \tag{7.11}$$

at the end of the Mu3e experiment. Notably, $\sigma_{15\text{mV}}$ has a much larger margin for extra jitter not considered in this measurement to reach the limit of the timing resolution of 100 ps.

Figure 7.18 studies the best timing resolution σ_{min} at different doses and the corresponding threshold. Both σ_{min} and its threshold increase with dose, and the best threshold saturates to around 25 mV. Comparatively, $\sigma_{15\text{mV}}$ was also plotted, revealing only a small difference between $\sigma_{15\text{mV}}$ and σ_{min}, resulting in the same σ_0 and similar σ_1 with a relative error of

$$\frac{\Delta\sigma_1}{\sigma_1} = 9.07\,\%. \tag{7.12}$$

The σ_{min} at the end of the Mu3e experiment is expected to be

$$\sigma_{\text{min}}(\Phi_{\text{eq}} = 2.23 \times 10^{11}\ \text{n}_{\text{eq}}/\text{cm}^2) = 49.12\,\text{ps}. \tag{7.13}$$

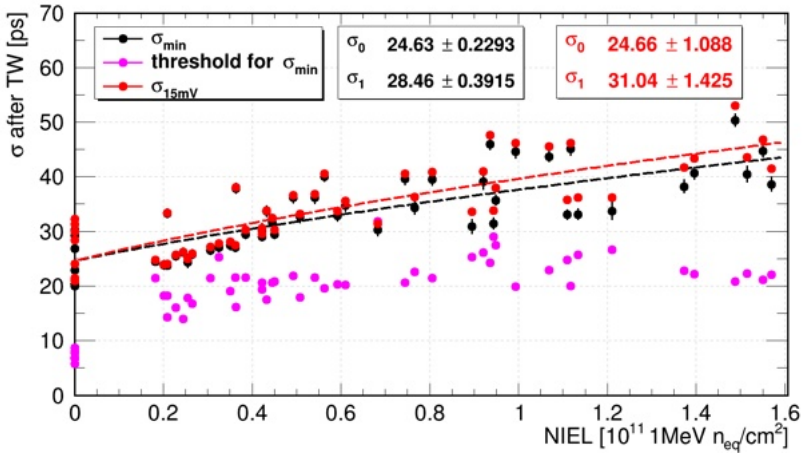

Figure 7.18: Best timing resolution and its corresponding threshold with different radiation doses. σ_{min} is slightly better than $\sigma_{15\text{mV}}$ with timing thresholds up to 30 mV, indicating that the timing resolution is not sensitive to the threshold within the high threshold range.

In summary, the Tile Detector's timing resolution degrades with increasing radiation dose, with the extent of degradation being threshold-dependent. The primary timing effect from radiation damage is the dramatic increase in vertical noise, leading to significant timing resolution degradation in the low threshold range where vertical noise dominates the timing jitter. The mean value of $\sigma_{5\text{mV}}$ with a dose of $\Phi_{\text{eq}} = 2.23 \times 10^{11}\ \text{n}_{\text{eq}}/\text{cm}^2$ is around 85.11 ps, providing little margin for extra jitter not included in this measurement. In contrast, timing degradation is much smaller at higher threshold levels, which is suggested for future experiment designs with considering radiation robustness. The mean value of $\sigma_{15\text{mV}}$ and σ_{min} at end of the Mu3e experiment are estimated to be better than 52.50 ps and 49.12 ps.

7.3 Efficiency and Radiation Impacts

7.3.1 Efficiency

The efficiency of the Tile Detector is determined by two main factors: the signal-to-noise ratio (SNR) of the analog signal and the dead time of the discriminator in MuTRiG. Detectable signals are those with amplitudes exceeding the energy threshold of MuTRiG and not in the dead time of either a previous event or noise.

The analog signal of the Tile Detector is influenced by three main parts:

- Tile parameters: light yield, decay time, and attenuation govern the quantity and speed of light emission;
- SiPM parameters: PDE, DCR, and cross-talk affect the detector's SNR;
- Detector design and production: Tile geometry, wrapping with foil, and the coupling efficiency between Tile and SiPM influence light collection.

With scintillator EJ228, SiPM S13360-3050VE, and an appropriate detector design and production, the MPV of detected photons is approximately 1000 in the Tile Detector, resulting in a high SNR.

MuTRiG employs two thresholds to extract timing and energy information separately, and event data is only accessible when the signal amplitude is adequate to trigger the higher threshold: the energy threshold. The probability of a signal being too small to reach the energy threshold in the Tile Detector is low due to the substantial number of photons collected by the SiPM and the fact that the energy threshold in MuTRiG is designed to be as low as a few photon levels. However, even when a big signal is detected, the timing information might still be wrong if the timing threshold is at the noise level. Therefore, the dead time of the timing threshold is another crucial parameter for the efficiency.

Beam test results from DESY demonstrated an efficiency between 93.8 % and 98.7 % for the non-irradiated prototype with Mu3e Tile Detector readout electronics, as illustrated in Figure 7.19. After correcting for screened events due to the dead time of previous events or noise, an efficiency higher than 99 % was achieved.

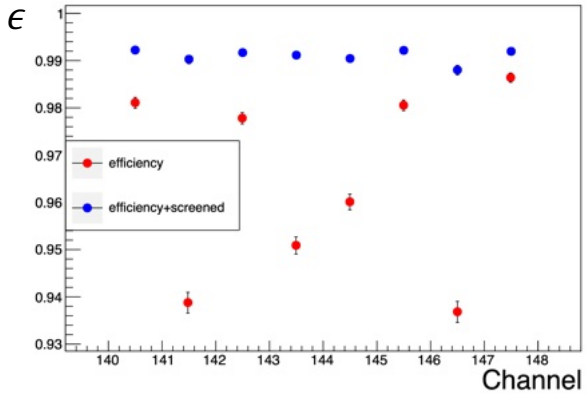

Figure 7.19: Efficiency of the non-irradiated Tile Detector prototype obtained from the beam-test in DESY. This is the result when reading by the Tile Detector's full-chain electronics. (red) Efficiency directly measured with nearby channels along the beam direction as a reference. (blue) Efficiency with screened-event correction. Figure from [83].

7.3.2 Radiation impacts

As previously discussed, the primary effects of irradiation damage on the Tile Detector are the increase in the SiPM's signal baseline and noise on the baseline. Due to the large number of photons collected by the SiPM in a short period, the SNR remains high even after radiation exposure, which does not significantly impact the efficiency on the sensor side. However, the increase in noise and baseline substantially increases the dead time occupied by the noise. The rise in signal baseline compresses the dynamic range of the timing threshold, making it more susceptible to triggering and leading to an incorrect timestamp for the true signal, as shown in Figure 7.20a. Additionally, the timing branch will always be occupied if the timing threshold is too low, as depicted in Figure 7.20b.

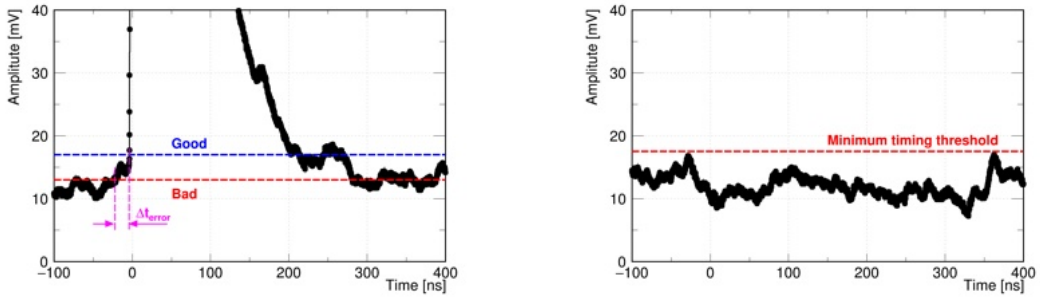

(a) Wrong timestamp.

(b) Minimal timing threshold requirement.

Figure 7.20: Example of noise impact on efficiency. (a) With significant noise and low timing threshold, the timestamp given is not the true time of the signal, but a random time triggered by the noise. (b) The minimal timing threshold should be larger than the noise level; otherwise, the case in (a) cannot be avoided and the efficiency will be limited by the analog signal.

7.4 Efficiency Characterization

The efficiency of the signal from SiPMs was measured using data from the beam-test campaign conducted for the timing performance test. The signal efficiency ϵ_{signal} was defined as the probability of observing the signal in the interested channel when significant signals are found in all other three channels in the same row (see Figure 7.8a):

$$\epsilon_{\text{signal}} = \frac{N_{\text{detect}}}{N_{\text{all}}}, \tag{7.14}$$

where N_{detect} is the number of signals detected in the interested channel and N_{all} is the total number of expected events.

Figure 7.21 displays efficiency-threshold curve examples with different radiation doses, which are fitted with:

$$\epsilon_{\text{signal}}(x) = \frac{1}{2} \cdot (1 + erf(x)), \tag{7.15}$$

where x represents the threshold. $erf(x)$ is the Gauss error function from which the thr_{50}, threshold when efficiency reaches 50 %, and σ_{thr} can be obtained. As expected, the efficiency can reach 100 % when directly reading the analog signal with the oscilloscope, even for the most irradiated SiPMs.

However, higher thresholds are required for channels with higher doses due to the increased noise level.

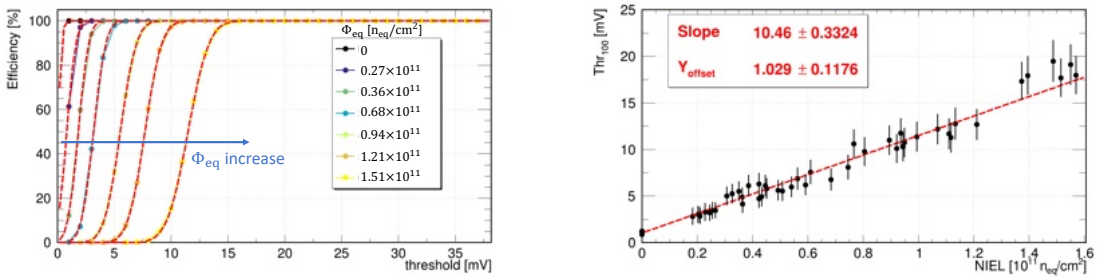

(a) Efficiency-threshold curves

(b) thr_{100} vs. radiation dose

Figure 7.21: Efficiency with different radiation doses.

Furthermore, a thr_{100}, defined as

$$thr_{100} = thr_{50} + 3 \cdot \sigma_{thr} \tag{7.16}$$

was employed to quantify the threshold when $\epsilon_{\text{signal}} = 100\,\%$. The thr_{100} plotted against radiation dose is provided in Figure 7.21b and is fitted with a linear function. Based on the fitting results, the dose coefficient of thr_{100} is approximately $10.46\,\text{mV}/(10^{11}\text{n}_{\text{eq}}/\text{cm}^2)$, which implies that the threshold must increase by around 10.46 mV to guarantee a 100 % efficiency on the analog signal side when the radiation dose increases by 10^{11} $\text{n}_{\text{eq}}/\text{cm}^2$.

A further investigation into the relationship between thr_{100} and the signal baseline V_{baseline} and its standard deviation σ_{baseline} was conducted. Figure 7.22 displays the ratio of the relative threshold $thr_{100} - V_{\text{baseline}}$ to σ_{baseline}, indicating that the efficiency should be 100 % when

$$thr_{100} > V_{\text{baseline}} + 2 \cdot \sigma_{\text{baseline}}. \tag{7.17}$$

The reason that the ratio is higher than 2 when the dose is smaller than 0.2×10^{11} $\text{n}_{\text{eq}}/\text{cm}^2$ is due to the poor fit result to determine the thr_{100}, which is primarily limited by the amplitude resolution of the signal from the scope.

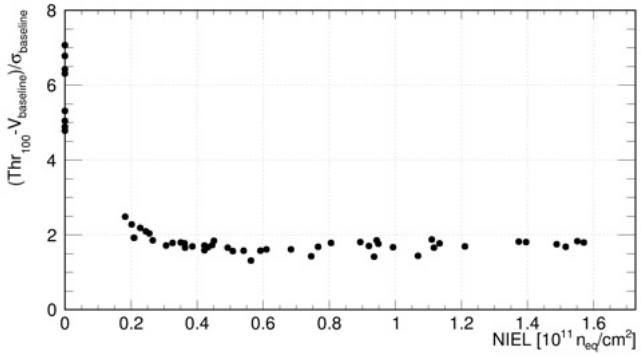

Figure 7.22: Relationship between the relative threshold ($thr_{100} - V_{\text{baseline}}$) and baseline fluctuation (σ_{baseline}). The large ratio at doses less than 0.2×10^{11} $\text{n}_{\text{eq}}/\text{cm}^2$ is attributable to the poor fit results used to determine thr_{100}.

Chapter 8

Proposed Improvement to the Experimental Design

Based on the radiation study results discussed in this work, some suggestions were proposed for the Mu3e Tile Detector design Improvement, which mainly related to the support system and readout electronics.

8.1 Support System Design

This section discusses the support system, mainly the HV and cooling system, used for the Tile Detector support in the Mu3e experiment.

In the original Mu3e design, an HV module with a maximum power of 1.5 W was utilized to bias the 416 Tile Detector SiPMs in the same Tile Detector Module, and a $V_{ov} > 5$ V of SiPM was typically employed for higher gain to achieve optimal timing. The maximum voltage of the HV module assigned to the Tile Detector Module is 60 V with a maximum current of approximately 25 mA.

Additionally, a water cooling system providing a temperature just above 0 °C was intended for SiPM cooling to minimize SiPM noise while avoiding concerns about ice formation on the detector system.

The previous design parameters are summarized in Table 8.1.

Table 8.1: Parameters of the Tile Detector support system planned in the Mu3e design.

System	Parameter	value	unit
HV (single cable):			
	Power	1.5	W
	Voltage	< 60	V
	Current	25	mA
	V_{ov} for SiPM	> 5	V
Cooling (water):			
	Temperature	> 0	°C

Due to the significant increase in I_d after radiation, a lower V_{ov} should be implemented to limit the dark current. Prior performance tests with prototypes demonstrated that the Tile Detector could provide better timing with $V_{ov} > 5$ V. However, the improvement in timing performance is quite small when

the $V_{ov} > 3$ V, which is the operation V_{ov} officially suggested in the datasheet. Furthermore, the timing performance measured in this work also indicates that the Tile Detector can achieve a good timing resolution and efficiency with $V_{ov} = 3.7$ V. Therefore, the V_{ov} greater than 3 V is preferred for the Tile Detector , considering the radiation damage, compared to 5 V.

Based on the SiPM characterization with different doses, the dose coefficient of I_d is $0.21\text{mA}/(10^{11}\ \text{n}_{eq}/\text{cm}^2)$ with $V_{ov} = 3.7$ V and $T = 11.38$ °C. Therefore, the I_d distribution of the Tile Detector SiPMs at the end of the Mu3e Phase I run can be estimated by the dose distribution obtained from GEANT4 simulation, as depicted in Figure 4.11. Figure 8.1 shows the corresponding I_d distribution, which yields a maximum I_d of 0.47 mA and 0.29 mA per sensor for the US and DS stations, respectively.

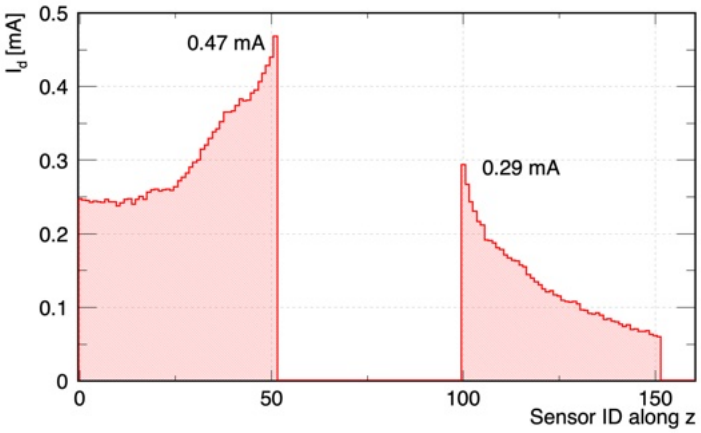

Figure 8.1: Dark current distribution expected in the Tile Detector SiPMs at the end of the Mu3e Phase I run. Each bin value represents the average in the ring with the same z position. Sensors 0-51 are in the US and 100-151 are in the DS.

Because the Tile Detector is a modularized detector with the Matrix as the base unit, the I_d distribution in different Tile Detector Matrices was calculated using

$$I_{d,Mat}(ID_{Mat}) = 4 \times \sum^{4} I_d(ID_{SiPM}), \tag{8.1}$$

where $I_{d,Mat}(ID_{Mat})$ represents the current in Matrix ID_{Mat} and $I_d(ID_{SiPM})$ is the dark current depicted in Figure 8.1, with four ID_{SiPM} selected based on the Matrix position. Figure 8.2 displays the $I_{d,Mat}$ for all 26 Tile Detector Matrices on the US and DS stations. Matrices with the same axial coordinate (z) have the same I_d, as the dose difference for sensors at the same z can be disregarded. Furthermore, the total dark current of one Tile Detector Module $I_{d,Mod}$ is approximately 126 mA and 54 mA for the US and DS, respectively, with the Matrices closest to the experiment's center (IDs 24 and 25) having the highest dark current at around 7 mA.

Additionally, event signals also contribute current to the HV lines. With an event hit rate of up to 50 kHz/channel [4] and an average of 1000 detected photons per event, the detected photon rate reaches 50 MHz/channel. As reported in the DCR characterization, the current contribution from $r_d \approx 1$ GHz is approximately 0.33 mA with $V_{ov} = 3.7$ V. Consequently, the current contribution from the event signal with a photon rate of 50 MHz/channel is around 16.5 μA/channel, resulting in an overall signal current

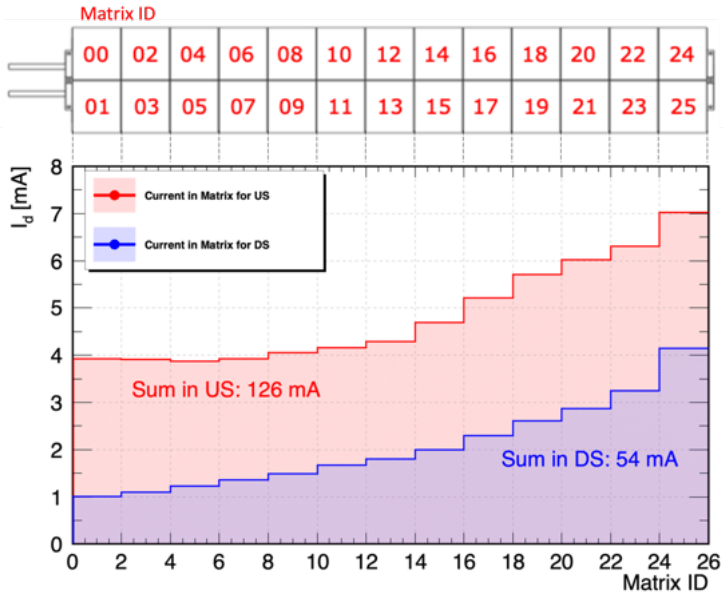

Figure 8.2: I_d in different Tile Detector Matrices. Matrices with larger IDs are closer to the center of the experiment, and the two pipes close to Matrices 0 and 1 are cooling pipes. Matrices mounted on the same z position, e.g. Matrix 0 and 1, have the same I_d, which is due to the symmetry of dose along ϕ.

of $I_{\mathrm{signal,Mod}} = 6.86\,\mathrm{mA}$ for a full Tile Detector Module. The signal current remains at 6.86 mA even at lower temperatures if V_ov remains constant, as the number of photons is not temperature-dependent and gain is predominantly governed by V_ov.

Following discussions with the Mu3e HV module designer, the HV modules designated for the Tile Detector can be improved by 50 %, leading to a maximum current of 37.5 mA. The temperature dependence of I_d leads to:

$$\frac{I_\mathrm{d}(T)}{I_\mathrm{d}(T = 11.38\,^\circ\mathrm{C})} = e^{\frac{T-11.38}{T_0}}, \tag{8.2}$$

with $T_0 = 15.7\,^\circ\mathrm{C}$ derived from the sensor characterization. Hence, the total current for a Tile Detector Module in the US operating at the originally designed temperature $T > 0\,^\circ\mathrm{C}$ is:

$$I_\mathrm{Mod} = I_{\mathrm{d,Mod}}(T > 0\,^\circ\mathrm{C}) + I_{\mathrm{signal,Mod}} > 67.89\,\mathrm{mA}, \tag{8.3}$$

which is still significantly higher than the current that can be provided to each Tile Detector Module. To meet $I_\mathrm{Mod} < 37.5\,\mathrm{mA}$, the working temperature must satisfy $T < -10.82\,^\circ\mathrm{C}$. The suggested nominal temperature for the Tile Detector is

$$T_\mathrm{nominal} = -10\,^\circ\mathrm{C}, \tag{8.4}$$

taking into account some margin for damage annealing. As a result, a liquid capable of going below $-20\,^\circ\mathrm{C}$, with considering the heat transfer between environment, should replace water as the heat transfer liquid.

Moreover, to reduce the voltage drop and heat production on the TMB, the HV was redesigned to bias all 26 matrices by dividing them into four groups with separate HV lines. Figure 8.3 illustrates the current integral along Matrix ID, indicating that 50 % of the current is reached in Matrix 15.

Consequently, Matrices 0-15 can be connected to the first two HV branches, and Matrices 16-25 can be connected to the other two branches, separating Matrices with odd and even IDs into different branches. Matrices in different HV branches are also marked in Figure 8.3.

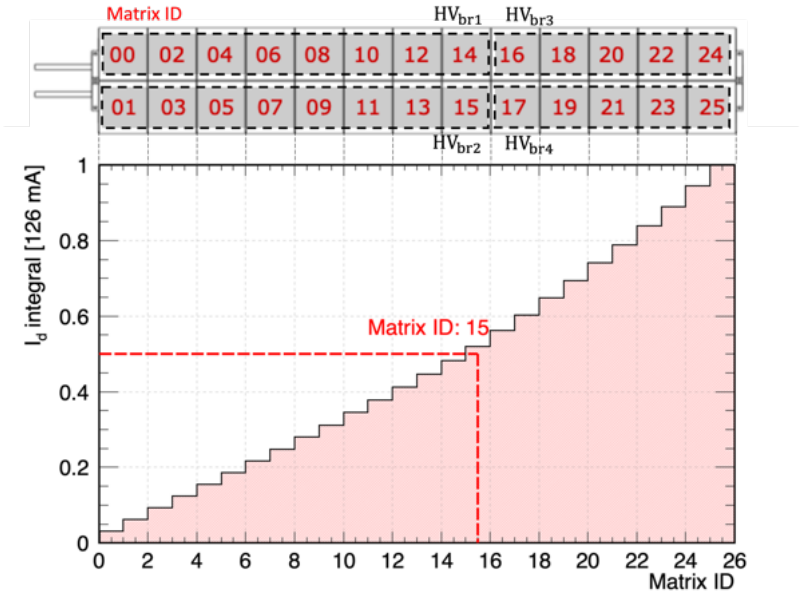

Figure 8.3: Integral of I_d along Matrices. The integral for each bin is the current sum of all the Matrices with IDs not larger than the bin value. Each Tile Detector Module is biased by four HV branches: branch 1 for Matrices 0 to 15 with even IDs, branch 2 for Matrices 0 to 15 with odd IDs, branch 3 for Matrices 16 to 25 with even IDs, and branch 4 for Matrices 16 to 25 with odd IDs.

In conclusion, the suggested modifications for the Mu3e Tile Detector support system, considering radiation damage, are primarily related to the HV power and cooling, which are summarized in Table 8.2.

Table 8.2: Comparison of design in the Mu3e Tile Detector support system before and after radiation damage considered.

System	Parameter	old	new
HV :			
	number of branches	1	4
	Power	1.5 W	2.25 W
	Voltage	up to 60 V	up to 60 V
	Current	25 mA	37.5 mA
	V_{ov} for SiPM	>5 V	>3 V
Cooling:			
	Liquid type	water	capable for −20 °C
	Liquid temperature	above 0 °C	below −20 °C
	Nominal temperature	-	−10 °C

8.2 Readout Electronics

The characterization results suggest that radiation damage effects on the FE sensor, SiPM and Tile, will not significantly degrade the timing resolution and efficiency if appropriate readout electronics are implemented.

With the best timing resolution $\sigma_{5\text{mV,min}} \approx 25$ ps for the non-irradiated SiPMs when read directly by the oscilloscope and $\bar{\sigma} \approx 47$ ps using the Mu3e Tile Detector full-chain electronics [91], an additional jitter that must be taken into account for the actual Mu3e Tile Detector is:

$$\sigma_{\text{extra}} = \sqrt{\bar{\sigma}^2 - \sigma^2_{5\text{mV,min}}} \approx 40\,\text{ps}. \tag{8.5}$$

The σ_{min} of the irradiated Tile Detector is expected to be better than 50 ps at the end of the Mu3e Phase I run, as obtained from the beam-test campaign with direct signal readings from the oscilloscope. Assuming σ_{extra} is dose independent, the estimated full-chain timing resolution for the Tile Detector should be better than 60 ps at the end of Phase I run, which still meets the required timing resolution of <100 ps.

Due to the significant increase in the signal baseline and fluctuations on the baseline, the original timing threshold designed in MuTRiG is unable to identify the correct timestamp with high efficiency. To address this issue, the idea of adding an additional bias to the original threshold to extend the dynamic range of the timing threshold was proposed by the ASIC designer in the collaboration. Figure 8.4 illustrates the schematic that explains the idea, where the new maximum value of the threshold is higher than the old design by the "bias" value, which can be tuned independently based on the requirement.

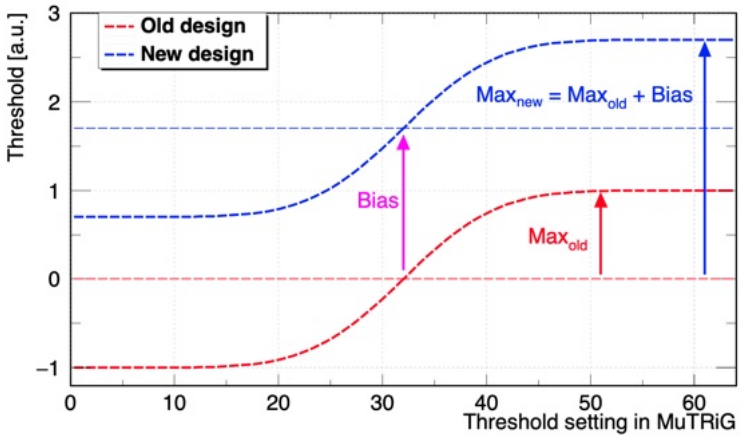

Figure 8.4: Schematic of threshold modification in the next version of MuTRiG. Only half of the dynamic range of the timing threshold implemented in the current version of MuTRiG is used because the Tile Detector only has signals above 0. The idea to extend the old dynamic range is to employ an additional bias to the old timing threshold. With an adjustable bias value, the dynamic range can be significantly extended to fulfill the requirements of the irradiated Tile Detector.

Chapter 9

Summary

The charged Lepton Flavor Violation (cLFV) decay process $\mu^+ \rightarrow e^+e^+e^-$ is suppressed in the Standard Model (SM) of particle physics, with a branching ratio $\mathcal{B}(\mu^+ \rightarrow e^+e^+e^-) < 10^{-54}$, which is undetectable by experiment. However, many new theories beyond the SM predict an experimentally accessible decay rate. The Mu3e experiment is designed to search for the decay process $\mu^+ \rightarrow e^+e^+e^-$ with a sensitivity of $O(10^{-16})$, which is four orders of magnitude better than the current exclusion limit. Any observation of this decay would be a clear signal for New Physics beyond the SM, and a non-observation would still strongly restrict the parameter space of new theories.

Background suppression is the most significant challenge to achieve the desired sensitivity, requiring excellent vertex, momentum, and timing resolution. Therefore, the Tile Detector, designed to provide the most accurate timing measurement with a timing resolution of <100 ps at an efficiency close to 100 %, is crucial to suppress the accidental background. To achieve the required timing resolution, the fast scintillator EJ228 and the SiPM S13360-3050VE are employed as the front-end sensor, with signal read out by a custom ASIC chip, MuTRiG. With the latest version of the technical prototype, an average timing resolution of $\bar{\sigma} = 47$ ps with an efficiency higher than 99 % was reached in a 3 GeV electron beam-test. However, this performance does not account for radiation damage from the Mu3e radiation environment, which primarily degrades the performance of the SiPMs. According to GEANT4 simulations, the maximum radiation dose in the Tile Detector SiPMs at the end of the Phase I run is approximately 2.23×10^{11} n_{eq}/cm^2.

To investigate the radiation impacts on the Tile Detector, a radiation damage test was conducted at PSI, followed by comprehensive characterizations of both fundamental parameters and performance.

The radiation damage campaign was performed with the muon beamline πE5, which will be used for the actual experiment. Consequently, a similar radiation field expected in the real Mu3e experiment was emulated, and the dose reached, according to the GEANT4 simulation, is up to 1.57×10^{11} n_{eq}/cm^2. This dose is approximately 70 % of the maximum dose expected in the Mu3e experiment and higher than 80 % of SiPMs' maximum doses, which is sufficient to predict performance for the full Phase I run.

A detailed SiPM characterization was performed after the radiation damage, as it is the most radiation-damage-sensitive component in the Tile Detector. The damage distribution in the SiPM was visualized by imaging the light from the avalanche process, where damage centers are uniformly distributed due to the low probability of creating cluster damage. No significant changes were found in the fundamental parameters (quenching resistor, breakdown voltage, temperature dependence) via the current-voltage

scan and temperature dependence measurements. The most significant impacts on the SiPM discovered during the characterization were the substantial increase in signal baseline and its fluctuation on the baseline.

The signal baseline impact was characterized by the dark current above the breakdown voltage, resulting in a dose coefficient of 0.21 $\mathrm{mA}/(10^{11}\,\mathrm{n_{eq}}/\mathrm{cm}^2)$ with an over-voltage $V_{\mathrm{ov}} = 3.7\,\mathrm{V}$ at a temperature $T = 11.38\,^{\circ}\mathrm{C}$. Estimated from the dark current, the DCR at the end of the experiment could reach up to 1.4 GHz at the same temperature. Furthermore, the dark current is reduced to $\frac{1}{e}$ when the temperature decreases by 15.7 °C due to the decrease in the DCR at lower temperatures, while 30 % of the dark current vanished with annealing temperature $T_{\mathrm{ann}} = 40\,^{\circ}\mathrm{C}$ in around 3 days as a result of damage defect recovery.

The noise of the radiated SiPMs was characterized by the noise Power Spectral Density (PSD) in the frequency domain. The noise in the low-frequency region was found to be dominated by the $1/f$-like noise, which might result from the charge carrier trap/release process in the defect centers. In the higher frequency region, the noise was dominated by the SiPM-specific noise, the pile-up of the decay tails of the SiPM dark event signals, which agrees with both theoretical calculations and SiPM response simulations. Consequently, a formula comprising two terms with only dark current as a variable was employed to model the noise PSD, which accurately matches the PSD at different doses. The good agreement between the RMS estimated from the PSD formula and that measured from the oscilloscope further verifies the formula. The RMS contribution from the SiPM-specific noise is greater than that from the $1/f$-like noise.

The timing and efficiency performance characterization of the irradiated Tile Detector was conducted in a beam-test at DESY with a 3 GeV electron beam, with the signal directly read out by the oscilloscope, since current MuTRiG ASIC is unable to handle the signal from the irradiated SiPMs. The significant increase in vertical noise in SiPM leads to a considerable degradation in timing resolution at the originally designed low timing threshold, while a much smaller degradation is observed at higher thresholds due to the increased signal slope. A timing resolution better than 60 ps was estimated at the end of the Mu3e phase I run with potential time jitter from readout electronic considered, which still meets the requirement of a timing resolution better than 100 ps. An efficiency of 100 % was observed by reading the signal directly from the oscilloscope, owing to the large number of photons detected. Furthermore, the lowest threshold at which the efficiency reached 100 % demonstrated a linear increase with the radiation dose, attributed to the increasing noise levels.

To address the significant increase in dark current and noise, several modifications for the Tile Detector support system have been proposed. These include lowering the temperature to below −10 °C and reducing the operation over-voltage to above 3 V. Furthermore, the nominal high-voltage power allocated to the Tile Detector has been increased by 50 % to ensure the provision of sufficient current. Additionally, to handle the signal from the irradiated detector, a timing threshold with a higher dynamic range is required in the new version of MuTRiG. With these adjustments, the Tile Detector, even when subjected to the exposure dose of a full phase I run, can still meet the performance requirements: a timing resolution of less than 100 ps with an efficiency close to 100 %.

Appendix

Appendix A

Supplementary Materials for Simulation

A.1 Ionization Dose Simulation Results

Ionization dose results for overall Mu3e experiment is shown in the plots, which are from the Mu3e internal communication contributed by Professor Niklaus Berger from Johannes Gutenberg-Universität Mainz.

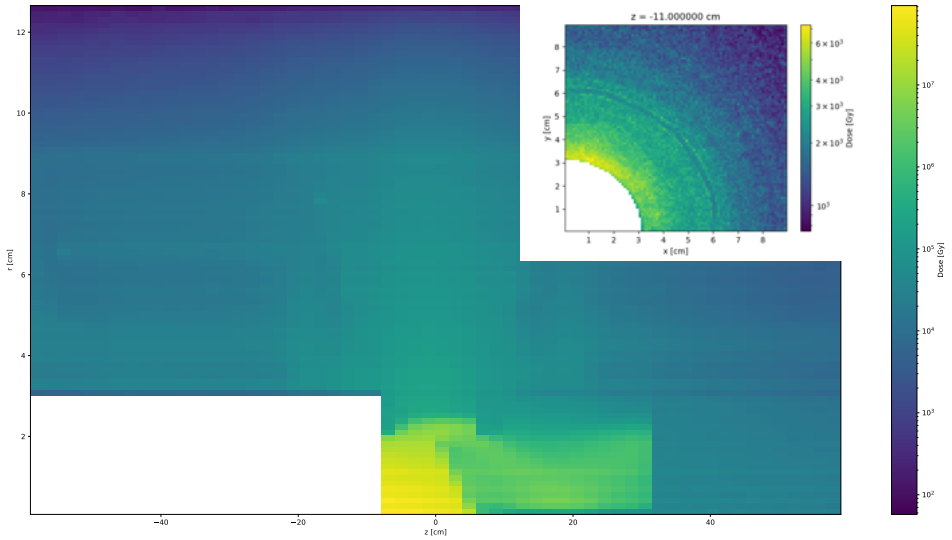

Figure A.1: Dose distribution of the full Mu3e detector. The highest dose observed on the target and pixel layers around it in the central station. The ionization dose of the tile detector is below 10^4 Gy.

A.2 Simulation Configuration for the Full Mu3e Simulation

Table A.1: Some simulation configurations from the version "v4.3" of the general Mu3e simulation software.

Simulation setting	Value
Muon beam	
Type	μ^+
polarization	1
Energy	27.86(±0.77) MeV
z position	−100 cm
Profile	$\sigma_x = 7.8$ mm; $\sigma_y = 9.1$ mm
Magnetic field	
Strength	1 T

A.3 Damage Function Data Used in Simulation

Table A.2: Electron-induced displacement damage in silicon with kinetic energies from 300 keV to 200 MeV, which is used in the Mu3e radiation damage simulation. Data from [108].

Kinetic Energy of Electron (E_e [MeV])	Damage Function ($D/D(E_n = 1\,\text{MeV})$)
3.000E-01	3.182E-03
5.000E-01	7.998E-03
7.000E-01	1.139E-02
1.000E+00	1.543E-02
2.000E+00	2.489E-02
3.000E+00	3.126E-02
5.000E+00	3.979E-02
7.000E+00	4.558E-02
1.000E+01	5.160E-02
2.000E+01	6.241E-02
3.000E+01	6.780E-02
5.000E+01	7.344E-02
7.000E+01	7.634E-02
1.000E+02	7.870E-02
2.000E+02	8.106E-02

Appendix B

Supplementary Materials for Irradiation Beam-test

B.1 πE5 Beamline Configurations

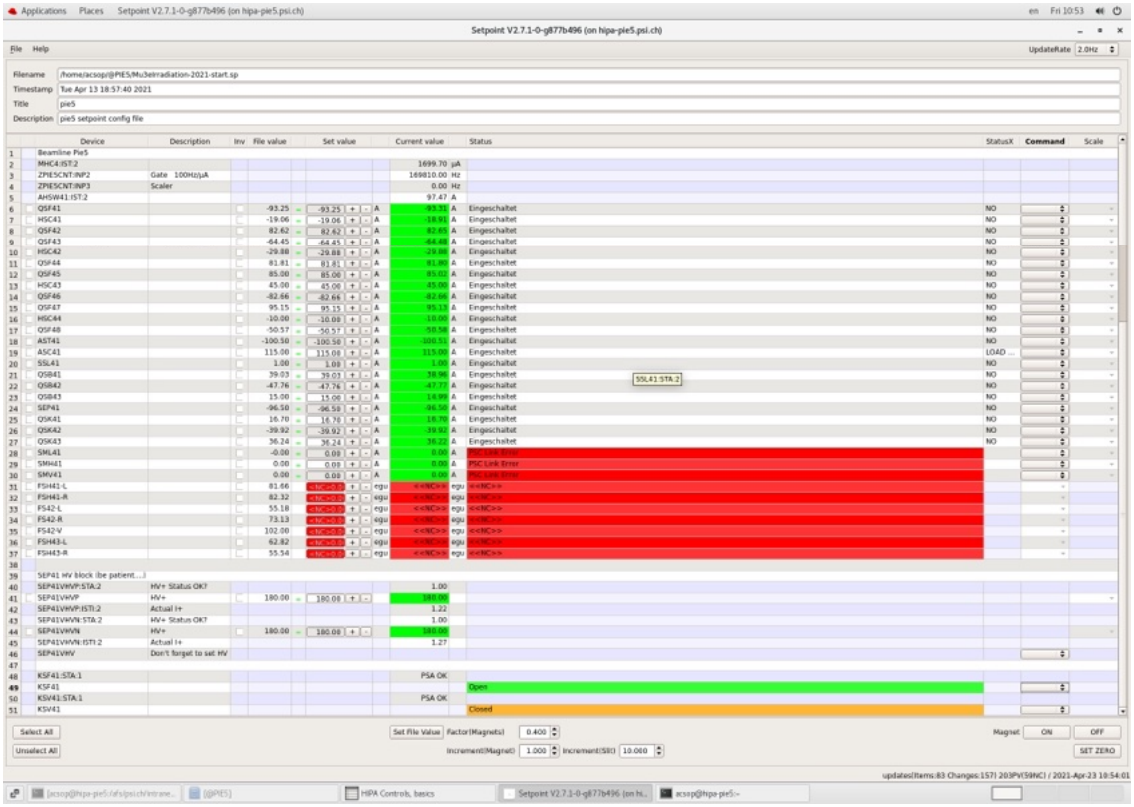

Figure B.1: Screenshot of πE5 beamline configuration for the Mu3e Tile Detector radiation beam-test campaign. The KSF41 is the shutter status, where the "open" means the muon produced on the target TgE can go to the beam line and reach the Tile Detector samples. All the other configuration remains the same during the whole beam-test period to keep the proton current to muon ratio constant.

B.2 Beam Information

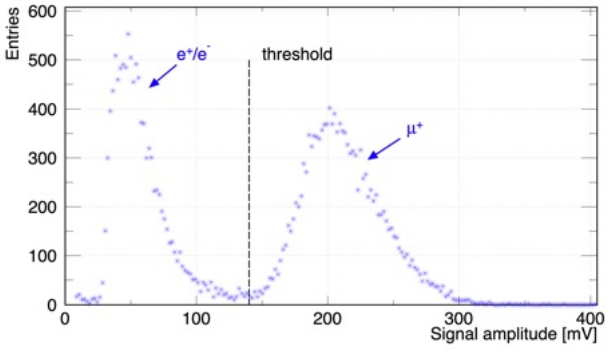

(a) Signal spectrum from scanner.

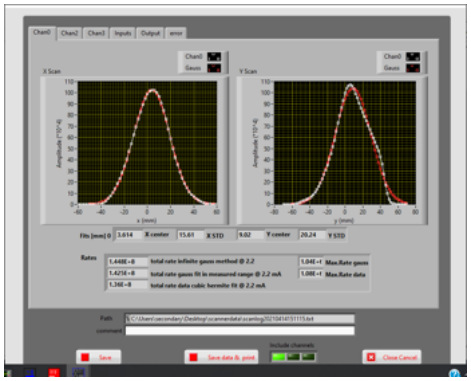

(b) Software for muon rate scan.

Figure B.2: Muon scan from the PSI πE5 beamline before the stopping plane.

Appendix C

Lists

C.1 List of Figures

C.2 List of Tables

Appendix D

Bibliography

[1] Andrew Plaks and Michael Nylan. *Zuo Tradition/Zuozhuan: Commentary on the "Spring and Autumn Annals"*. University of Washington Press, 2016.

[2] William Wallace. “Empedocles”. In: *Encyclopaedia britannica* (1911), pp. 344–345.

[3] Sea Agostinelli et al. “GEANT4—a simulation toolkit”. In: *Nuclear instruments and methods in physics research section A: Accelerators, Spectrometers, Detectors and Associated Equipment* 506.3 (2003), pp. 250–303.

[4] Hans Patrick Eckert. “The Mu3e tile detector”. PhD thesis. Heidelberg University, 2015.

[5] A Pais and SB Treiman. “How many charm quantum numbers are there?” In: *Physical Review Letters* 35.23 (1975), p. 1556.

[6] Glen Cowan. “Review of particle physics”. In: *Phys. Rev. D* 86.010001 (2012), p. 390.

[7] Particle Data Group et al. “Review of Particle Physics”. In: *Progress of Theoretical and Experimental Physics* 2022.8 (2022), p. 083C01.

[8] Frederik Van der Veken, Julia Woithe, and Jeff Wiener. *Lets have a coffee with the Standard Model of particle physics!* Tech. rep. 2022.

[9] Serguei Chatrchyan et al. “Observation of a new boson at a mass of 125 GeV with the CMS experiment at the LHC”. In: *Physics Letters B* 716.1 (2012), pp. 30–61.

[10] Georges Aad et al. “Observation of a new particle in the search for the Standard Model Higgs boson with the ATLAS detector at the LHC”. In: *Physics Letters B* 716.1 (2012), pp. 1–29.

[11] Lyndon Evans. “The large hadron collider”. In: *New Journal of Physics* 9.9 (2007), p. 335.

[12] Tsvi Piran. “The physics of gamma-ray bursts”. In: *Reviews of Modern Physics* 76.4 (2005), p. 1143.

[13] Sheldon L Glashow. “Partial-symmetries of weak interactions”. In: *Nuclear physics* 22.4 (1961), pp. 579–588.

[14] S Weinberg. “WEINBERG 1967”. In: *Phys. Rev. Lett* 19 (1967), p. 1264.

[15] A Salam and N Svartholm. “Proc. 8th Nobel Symp. on Elementary particle theory, relativistic groups and analyticity”. In: (1968).

[16] Mark Thomson. *Modern particle physics*. Cambridge University Press, 2013.

[17] Gianfranco Bertone and Dan Hooper. “History of dark matter”. In: *Reviews of Modern Physics* 90.4 (2018), p. 045002.

[18] Z Ahmed et al. “Search for Axions with the CDMS Experiment”. In: *Physical review letters* 103.14 (2009), p. 141802.

[19] AH Abdelhameed et al. “First results from the CRESST-III low-mass dark matter program”. In: *Physical Review D* 100.10 (2019), p. 102002.

[20] DS Akerib et al. “The lux-zeplin (lz) experiment”. In: *Nuclear Instruments and Methods in Physics Research Section A: Accelerators, Spectrometers, Detectors and Associated Equipment* 953 (2020), p. 163047.

[21] DS Akerib et al. “The large underground xenon (LUX) experiment”. In: *Nuclear Instruments and Methods in Physics Research Section A: Accelerators, Spectrometers, Detectors and Associated Equipment* 704 (2013), pp. 111–126.

[22] Thomas Gaisser and Francis Halzen. “IceCube”. In: *Annual Review of Nuclear and Particle Science* 64 (2014), pp. 101–123.

[23] Csaba Csaki. “The minimal supersymmetric standard model”. In: *Modern Physics Letters A* 11.08 (1996), pp. 599–613.

[24] Christian Autermann. “Experimental status of supersymmetry after the LHC Run-I”. In: *Progress in Particle and Nuclear Physics* 90 (2016), pp. 125–155.

[25] Anadi Canepa. “Searches for supersymmetry at the Large Hadron Collider”. In: *Reviews in Physics* 4 (2019), p. 100033.

[26] Wolfgang Adam and Iacopo Vivarelli. “Status of searches for electroweak-scale supersymmetry after LHC Run 2”. In: *International Journal of Modern Physics A* 37.02 (2022), p. 2130022.

[27] Riccardo Barbieri, Lawrence J Hall, Yasunori Nomura, and Vyacheslav S Rychkov. “Supersymmetry without a light Higgs boson”. In: *Physical Review D* 75.3 (2007), p. 035007.

[28] TOA HIGGS. “CERN Courier–digital edition”. In: *CERN COURIER* (2021).

[29] Philip Bambade et al. “The international linear collider: a global project”. In: *arXiv preprint arXiv:1903.01629* (2019).

[30] I Wilson. “The compact linear collider CLIC”. In: *Physics Reports* 403 (2004), pp. 365–378.

[31] Michael Benedikt et al. “Future Circular Collider”. In: *Annu. Rev. Nucl. Part. Sci* 69 (2019), p. 389.

[32] XinChou Lou. “The circular electron positron collider”. In: *Nature Reviews Physics* 1.4 (2019), pp. 232–234.

[33] Huaiyu Duan, George M Fuller, and Yong-Zhong Qian. “Collective neutrino oscillations”. In: *Annual Review of Nuclear and Particle Science* 60 (2010), pp. 569–594.

[34] T Araki et al. “Measurement of neutrino oscillation with KamLAND: Evidence of spectral distortion”. In: *Physical Review Letters* 94.8 (2005), p. 081801.

[35] MH Ahn et al. “Measurement of neutrino oscillation by the K2K experiment”. In: *Physical Review D* 74.7 (2006), p. 072003.

[36] Me Sanchez et al. *Observation of atmospheric neutrino oscillations in Soudan 2*. Tech. rep. Argonne National Lab., IL (US), 2003.

[37] A Aguilar et al. “Evidence for neutrino oscillations from the observation of ν_e appearance in a ν_μ beam”. In: *Physical Review D* 64.11 (2001), p. 112007.

[38] Yoshiyuki Fukuda et al. “Evidence for oscillation of atmospheric neutrinos”. In: *Physical review letters* 81.8 (1998), p. 1562.

[39] QR Ahmad, RC Allen, TC Andersen, et al. “Measurement of the rate of $\nu_e + d \rightarrow p + p + e^-$ interactions produced by $8B$ solar neutrinos at the Sudbury Neutrino Observatory”. In: *Phys. Rev. Lett* 87.7 (2001), p. 071301.

[40] KamLAND& Eguchi et al. “First results from KamLAND: evidence for reactor antineutrino disappearance”. In: *Physical Review Letters* 90.2 (2003), p. 021802.

[41] G Hernández-Tomé, G López Castro, and P Roig. “Flavor violating leptonic decays of τ and μ leptons in the Standard Model with massive neutrinos”. In: *The European Physical Journal C* 79.1 (2019), pp. 1–16.

[42] Jogesh C Pati and Abdus Salam. “Lepton number as the fourth "color"”. In: *Selected Papers Of Abdus Salam: (With Commentary)*. World Scientific, 1994, pp. 343–357.

[43] Howard Georgi and Sheldon L Glashow. “Unity of all elementary-particle forces”. In: *Physical Review Letters* 32.8 (1974), p. 438.

[44] Paul Langacker. “Grand unified theories and proton decay”. In: *Physics Reports* 72.4 (1981), pp. 185–385.

[45] Howard E Haber and Gordon L Kane. “The search for supersymmetry: probing physics beyond the standard model”. In: *Physics Reports* 117.2-4 (1985), pp. 75–263.

[46] Rabindra N Mohapatra and Jogesh C Pati. “Left-right gauge symmetry and an "isoconjugate" model of CP violation”. In: *Physical Review D* 11.3 (1975), p. 566.

[47] Manuel Drees. “Supersymmetric models with extended Higgs sector”. In: *International Journal of Modern Physics A* 4.14 (1989), pp. 3635–3651.

[48] C Dohmen et al. “Test of lepton-flavour conservation in $\mu \rightarrow e$ conversion on titanium”. In: *Physics Letters B* 317.4 (1993), pp. 631–636.

[49] Sindrum II Collaboration et al. “A search for muon to electron conversion in muonic gold”. In: *Eur. Phys. J. C* 47 (2006), p. 337.

[50] J Kaulard et al. “Improved limit on the branching ratio of $\mu^- \rightarrow e^+$ conversion on titanium”. In: *Physics Letters B* 422.1-4 (1998), pp. 334–338.

[51] U Bellgardt et al. “Search for the decay $\mu^+ \rightarrow e^+e^+e^-$”. In: *Nuclear Physics B* 299.1 (1988), pp. 1–6.

[52] AM Baldini et al. “Search for the lepton flavour violating decay $\mu^+ \to e^+\gamma$ with the full dataset of the MEG experiment”. In: *The European Physical Journal C* 76.8 (2016), p. 434.

[53] Bernard Aubert et al. “Searches for lepton flavor violation in the decays $\tau^\pm \to e^\pm\gamma$ and $\tau^\pm \to \mu^\pm\gamma$”. In: *Physical review letters* 104.2 (2010), p. 021802.

[54] K Hayasaka et al. “Search for lepton-flavor-violating τ decays into three leptons with 719 million produced $\tau^+\tau^-$ pairs”. In: *Physics Letters B* 687.2-3 (2010), pp. 139–143.

[55] Y Miyazaki et al. “Search for lepton flavor violating τ^- decays into $\ell^-\eta$, $\ell^-\eta'$ and $\ell^-\pi^0$”. In: *Physics Letters B* 648.5-6 (2007), pp. 341–350.

[56] Bernard Aubert et al. “Search for Lepton Flavor Violating Decays $\tau^\pm \to \ell^\pm\pi^0, \ell^\pm\eta^0, \ell^\pm\eta'$”. In: *Physical review letters* 98.6 (2007), p. 061803.

[57] Y Miyazaki et al. “Search for lepton-flavor-violating τ decays into a lepton and a vector meson”. In: *Physics Letters B* 699.4 (2011), pp. 251–257.

[58] E Abouzaid et al. “Search for lepton-flavor-violating decays of the neutral kaon”. In: *Physical review letters* 100.13 (2008), p. 131803.

[59] D Ambrose et al. “New Limit on Muon and Electron Lepton Number Violation from $K_L^0 \to \mu^\pm e^\mp$ Decay”. In: *Physical review letters* 81.26 (1998), p. 5734.

[60] Aleksey Sher et al. “Improved upper limit on the decay $K^+ \to \pi^+\mu^+e^-$”. In: *Physical Review D* 72.1 (2005), p. 012005.

[61] M Ablikim et al. “Search for the lepton flavor violation process $J/\psi \to e\mu$ at BESIII”. In: *Physical Review D* 87.11 (2013), p. 112007.

[62] M Ablikim et al. “Search for the charged lepton flavor violating decay $J/\psi \to e\tau$”. In: *Physical Review D* 103.11 (2021), p. 112007.

[63] M Ablikim et al. “Search for the lepton flavor violation processes $J/\psi \to \mu\tau$ and $e\tau$”. In: *Physics Letters B* 598.3-4 (2004), pp. 172–177.

[64] R Aaij et al. “Search for the Lepton-Flavor-Violating Decays $B_s^0 \to e^\pm\mu^\mp$ and $B^0 \to e^\pm\mu^\mp$”. In: *Physical review letters* 111.14 (2013), p. 141801.

[65] Bernard Aubert et al. “Searches for the decays $B^0 \to \ell^\pm\tau^\mp$ and $B^+ \to \ell^+\nu(\ell = e, \mu)$ using hadronic tag reconstruction”. In: *Physical Review D* 77.9 (2008), p. 091104.

[66] R Aaij et al. “Search for the Lepton-Flavor-Violating Decays $B_s^0 \to \tau^\pm\mu^\mp$ and $B^0 \to \tau^\pm\mu^\mp$”. In: *Physical Review Letters* 123.21 (2019), p. 211801.

[67] Bernard Aubert et al. “Measurements of branching fractions, rate asymmetries, and angular distributions in the rare decays $B \to K\ell^+\ell^-$ and $B \to K^*\ell^+\ell^-$”. In: *Physical Review D* 73.9 (2006), p. 092001.

[68] JP Lees et al. “Search for the decay modes $B^\pm \to h^\pm\tau\ell$”. In: *Physical Review D* 86.1 (2012), p. 012004.

[69] Atlas Collaboration et al. “Search for the Higgs boson decays H → ee and H → eμ in pp collisions at $\sqrt{s}$ = 13 TeV with the ATLAS detector”. In: *arXiv preprint arXiv:1909.10235* (2019).

[70] Albert M Sirunyan et al. “Search for lepton-flavor violating decays of the Higgs boson in the μτ and eτ final states in proton-proton collisions at $\sqrt{s}$= 13 TeV”. In: *Physical Review D* 104.3 (2021), p. 032013.

[71] Georges Aad et al. “Search for the lepton flavor violating decay Z → eμ in pp collisions at $\sqrt{s}$= 8 TeV with the ATLAS detector”. In: *Physical Review D* 90.7 (2014), p. 072010.

[72] R Akers et al. “A search for lepton flavour violating Z^0 decays”. In: *Zeitschrift für Physik C Particles and Fields* 67.4 (1995), pp. 555–563.

[73] DELPHI collaboration. “Search for lepton flavour number violating Z^0-decays”. In: *Zeitschrift für Physik C Particles and Fields* 73 (1997), pp. 243–251.

[74] Fabrizio Cei. “Status and perspectives of Lepton Flavour Violation experiments with muons.” In: *Journal of Physics: Conference Series*. Vol. 1526. 1. IOP Publishing. 2020, p. 012020.

[75] AM Baldini et al. “The design of the MEG II experiment”. In: *The European Physical Journal C* 78.5 (2018), pp. 1–60.

[76] Manuel Meucci. “MEG II experiment status and prospect”. In: *arXiv preprint arXiv:2201.08200* (2022).

[77] Frederik Wauters. “The Mu3e experiment”. In: *SciPost Physics Proceedings* 5 (2021), p. 020.

[78] WH Bertl et al. “SINDRUM II Collaboration”. In: *Eur. Phys. J. C* 47 (2006), p. 337.

[79] Vitaly Pronskikh et al. *Target Station design for the mu2e Experiment*. Tech. rep. Fermi National Accelerator Lab.(FNAL), Batavia, IL (United States), 2014.

[80] R Abramishvili et al. “COMET Phase-I technical design report, Prog. Theor”. In: *Exp. Phys* 2020 (2020).

[81] Niklaus Berger, Mu3e Collaboration, et al. “The mu3e experiment”. In: *Nuclear Physics B-Proceedings Supplements* 248 (2014), pp. 35–40.

[82] Yoshitaka Kuno and Yasuhiro Okada. “Muon decay and physics beyond the standard model”. In: *Reviews of Modern Physics* 73.1 (2001), p. 151.

[83] Kirk Arndt et al. “Technical design of the phase I Mu3e experiment”. In: *Nuclear Instruments and Methods in Physics Research Section A: Accelerators, Spectrometers, Detectors and Associated Equipment* 1014 (2021), p. 165679.

[84] Thomas Theodor Rudzki. “The Mu3e vertex detector-construction, cooling, and first prototype operation”. PhD thesis. Heidelberg University, 2022.

[85] Thomas J Roberts and Daniel M Kaplan. “G4beamline simulation program for matter-dominated beamlines”. In: *2007 IEEE Particle Accelerator Conference (PAC)*. IEEE. 2007, pp. 3468–3470.

[86] Ioannis Paraskevas. “Preparations for the Mu3e experiment: Magnet commissioning, beamline studies and a study of fake tracks”. PhD thesis. UCL (University College London), 2022.

[87] Cristina Martin Perez and Luigi Vigani. “Searching for the Muon Decay to Three Electrons with the Mu3e Experiment”. In: *Universe* 7.11 (2021), p. 420.

[88] Heiko Augustin, Ivan Perić, Andre Schöning, and Alena Weber. “The MuPix sensor for the Mu3e experiment”. In: *Nuclear Instruments and Methods in Physics Research Section A: Accelerators, Spectrometers, Detectors and Associated Equipment* 979 (2020), p. 164441.

[89] Heiko Augustin. “Development of a novel slow control interface and suppression of signal line crosstalk enabling HV-MAPS as sensor technology for Mu3e”. PhD thesis. Heidelberg University, 2021.

[90] Huangshan Chen et al. “MuTRiG: a mixed signal Silicon Photomultiplier readout ASIC with high timing resolution and gigabit data link”. In: *Journal of Instrumentation* 12.01 (2017), p. C01043.

[91] Hannah Klingenmeyer et al. “Measurements with the technical prototype for the Mu3e tile detector”. In: *Nuclear Instruments and Methods in Physics Research Section A: Accelerators, Spectrometers, Detectors and Associated Equipment* 958 (2020), p. 162852.

[92] *Fast timing plastic scintillator EJ228, EJ230*. Eljen Technology. URL: https://eljentechnology.com/products/plastic-scintillators/ej-228-ej-230.

[93] *3M™ Enhanced Specular Reflector (ESR)*. 3M™. URL: https://www.3m.com/3M/en_US/p/d/b5005047091/.

[94] *MPPC (Multi-Pixel Photon Counter): S13360-2050VE/-3050VE/-6050VE*. Hamamatsu. URL: https://www.hamamatsu.com/eu/en/product/optical-sensors/mppc/mppc_mppc-array.html.

[95] Heiko Augustin et al. “The Mu3e Data Acquisition”. In: *IEEE Transactions on Nuclear Science* 68.8 (2021), pp. 1833–1840.

[96] Mara Bruzzi. “Radiation damage in silicon detectors for high-energy physics experiments”. In: *IEEE Transactions on nuclear science* 48.4 (2001), pp. 960–971.

[97] Gunnar Lindström. “Radiation damage in silicon detectors”. In: *Nuclear Instruments and Methods in Physics Research Section A: Accelerators, Spectrometers, Detectors and Associated Equipment* 512.1-2 (2003), pp. 30–43.

[98] M Usami et al. “Radiation damage effect on time resolution of 6 series-connected SiPMs for MEG II positron timing counter”. In: *Nuclear Instruments and Methods in Physics Research Section A: Accelerators, Spectrometers, Detectors and Associated Equipment* 936 (2019), pp. 572–573.

[99] Timothy R Oldham and FB McLean. “Total ionizing dose effects in MOS oxides and devices”. In: *IEEE transactions on nuclear science* 50.3 (2003), pp. 483–499.

[100] Gerhard Lutz et al. *Semiconductor radiation detectors*. Springer, 2007.

[101] Mika Huhtinen. “Simulation of non-ionising energy loss and defect formation in silicon”. In: *Nuclear Instruments and Methods in Physics Research Section A: Accelerators, Spectrometers, Detectors and Associated Equipment* 491.1-2 (2002), pp. 194–215.

[102] Michael Moll. “Radiation damage in silicon particle detectors. Microscopic defects and macroscopic properties”. In: (1999).

[103] E Garutti and Yu Musienko. “Radiation damage of SiPMs”. In: *Nuclear Instruments and Methods in Physics Research Section A: Accelerators, Spectrometers, Detectors and Associated Equipment* 926 (2019), pp. 69–84.

[104] Roel Aaij et al. “Performance of the LHCb vertex locator”. In: *Journal of Instrumentation* 9.09 (2014), P09007.

[105] Victor AJ van Lint, Gunter Gigas, and Jack Barengoltz. “Correlation of displacement effects produced by electrons protons and neutrons in silicon”. In: *IEEE Transactions on Nuclear Science* 22.6 (1975), pp. 2663–2668.

[106] A Van Ginneken. *Nonionizing energy deposition in silicon for radiation damage studies*. Tech. rep. Fermi National Accelerator Laboratory, 1989.

[107] Maximo S Lazo, David M Woodall, and Patrick J McDaniel. “Silicon and silicon dioxide neutron damage functions”. In: *Proc. Fast Burt React. Workshop*. Vol. 1. 1986.

[108] Angela Vasilescu and Gunnar Lindstroem. *Displacement Damage in Silicon*. 2000. URL: https://rd50.web.cern.ch/niel/ (visited on 11/22/2022).

[109] Geoffrey P Summers et al. “Damage correlations in semiconductors exposed to gamma, electron and proton radiations”. In: *IEEE Transactions on Nuclear Science* 40.6 (1993), pp. 1372–1379.

[110] M Huhtinen and PA Aarnio. “Pion induced displacement damage in silicon devices”. In: *Nuclear Instruments and Methods in Physics Research Section A: Accelerators, Spectrometers, Detectors and Associated Equipment* 335.3 (1993), pp. 580–582.

[111] Patrick J Griffin, John G Kelly, Theodore F Luera, and Jason VanDenburg. *SNL RML recommended dosimetry cross section compendium*. Tech. rep. Sandia National Labs., Albuquerque, NM (United States), 1993.

[112] A Yu Konobeyev, Yu A Korovin, and VN Sosnin. “Neutron displacement cross-sections for structural materials below 800 MeV”. In: *Journal of nuclear materials* 186.2 (1992), pp. 117–130.

[113] J Barlow et al. “The momentum spectrum of electrons from muon decay”. In: *Proceedings of the Physical Society (1958-1967)* 84.2 (1964), p. 239.

[114] Christian Graf. “A Calibration Scheme for the Mu3e Tile Detector”. Masterarbeit. Heidelberg University, 2015.

[115] H Jivan et al. “Radiation damage effects on the optical properties of plastic scintillators”. In: *Nuclear Instruments and Methods in Physics Research Section B: Beam Interactions with Materials and Atoms* 409 (2017), pp. 224–228.

[116] Vladimir Baranov et al. “Effects of neutron radiation on the optical and structural properties of blue and green emitting plastic scintillators”. In: *Nuclear Instruments and Methods in Physics Research Section B: Beam Interactions with Materials and Atoms* 436 (2018), pp. 236–243.

[117] VN Salimgareeva and SV Kolesov. “Plastic scintillators based on polymethyl methacrylate: A review”. In: *Instruments and Experimental Techniques* 48.3 (2005), pp. 273–282.

[118] Zhao Li et al. “Properties of plastic scintillators after irradiation”. In: *Nuclear Instruments and Methods in Physics Research Section A: Accelerators, Spectrometers, Detectors and Associated Equipment* 552.3 (2005), pp. 449–455.

[119] Isabel García-Cortés et al. “In-situ evaluation of radiation induced optical degradation of candidate scintillator materials for ITER’s gamma and neutron detectors”. In: *Fusion Engineering and Design* 136 (2018), pp. 493–497.

[120] Alexei Ulyanov et al. “Radiation damage study of SensL J-series silicon photomultipliers using 101.4 MeV protons”. In: *Nuclear Instruments and Methods in Physics Research Section A: Accelerators, Spectrometers, Detectors and Associated Equipment* 976 (2020), p. 164203.

[121] O Bychkova et al. “Radiation damage uniformity in a SiPM”. In: *Nuclear Instruments and Methods in Physics Research Section A: Accelerators, Spectrometers, Detectors and Associated Equipment* 1039 (2022), p. 167042.

[122] S Sanchez Majos, P Achenbach, and J Pochodzalla. “Characterisation of radiation damage in silicon photomultipliers with a Monte Carlo model”. In: *Nuclear Instruments and Methods in Physics Research Section A: Accelerators, Spectrometers, Detectors and Associated Equipment* 594.3 (2008), pp. 351–357.

[123] A Stoykov et al. “A scintillating fiber detector for muon beam profile measurements in high magnetic fields”. In: *Nuclear Instruments and Methods in Physics Research Section A: Accelerators, Spectrometers, Detectors and Associated Equipment* 550.1-2 (2005), pp. 212–216.

[124] *Model 6487 Picoammeter/Voltage Source Reference Manual*. Keithley. URL: https://download.tek.com/manual/6487-901-01(B-Mar2011)(Ref).pdf.

[125] Roger Newman. “Visible light from a silicon p-n junction”. In: *Physical review* 100.2 (1955), p. 700.

[126] Andrea L Lacaita, Franco Zappa, Stefano Bigliardi, and Manfredo Manfredi. “On the bremsstrahlung origin of hot-carrier-induced photons in silicon devices”. In: *IEEE Transactions on electron devices* 40.3 (1993), pp. 577–582.

[127] *Kryo 30 datasheet*. LAUDA. URL: https://www.lauda.de/fileadmin/assets/downloads/pdf/Kryo_30_en-GB_2020.pdf.

[128] Ferenc Nagy, Gyula Hegyesi, Gábor Kalinka, and József Molnár. “A model based DC analysis of SiPM breakdown voltages”. In: *Nuclear Instruments and Methods in Physics Research Section A: Accelerators, Spectrometers, Detectors and Associated Equipment* 849 (2017), pp. 55–59.

[129] Anna Rita Altamura et al. “Characterization of Silicon Photomultipliers after proton irradiation up to 10^{12} n_{eq}/cm^2”. In: *Nuclear Instruments and Methods in Physics Research Section A: Accelerators, Spectrometers, Detectors and Associated Equipment* 1040 (2022), p. 167284.

[130] G Bondarenko et al. “Limited Geiger-mode silicon photodiode with very high gain”. In: *Nuclear Physics B-Proceedings Supplements* 61.3 (1998), pp. 347–352.

[131] Marius Grundmann. *Physics of semiconductors*. Vol. 11. Springer, 2010.

[132] Peter Welch. "The use of fast Fourier transform for the estimation of power spectra: a method based on time averaging over short, modified periodograms". In: *IEEE Transactions on audio and electroacoustics* 15.2 (1967), pp. 70–73.

[133] Arthur Schuster. "On the investigation of hidden periodicities with application to a supposed 26 day period of meteorological phenomena". In: *Terrestrial Magnetism* 3.1 (1898), pp. 13–41.

[134] V Vaseghi Saeed. *Advanced signal processing and digital Noise Reduction*. VIEWEG+ TEUBNER VERLAG, 2013, pp. 242–260.

[135] Eddy Simoen and Cor Claeys. "On the flicker noise in submicron silicon MOSFETs". In: *Solid-State Electronics* 43.5 (1999), pp. 865–882.

[136] DM Fleetwood. "1/f noise and defects in microelectronic materials and devices". In: *IEEE Transactions on Nuclear Science* 62.4 (2015), pp. 1462–1486.

[137] DM Fleetwood. "Origins of 1/f noise in electronic materials and devices: A historical perspective". In: *Noise in nanoscale semiconductor devices* (2020), pp. 1–31.

[138] Hei Wong. "Low-frequency noise study in electron devices: review and update". In: *Microelectronics Reliability* 43.4 (2003), pp. 585–599.

[139] M Jamal Deen and O Marinov. "Noise in advanced electronic devices and circuits". In: *AIP Conference Proceedings*. Vol. 780. 1. American Institute of Physics. 2005, pp. 3–12.

[140] Dimitri Boudier et al. "Discussion on the 1/f noise behavior in Si gate-all-around nanowire MOSFETs at liquid helium temperatures". In: *2018 Joint International EUROSOI Workshop and International Conference on Ultimate Integration on Silicon (EUROSOI-ULIS)*. IEEE. 2018, pp. 1–4.

[141] Yeal Nemirovsky, Igor Brouk, and Claudio G Jakobson. "1/f noise in CMOS transistors for analog applications". In: *IEEE transactions on Electron Devices* 48.5 (2001), pp. 921–927.

[142] Daniel M Fleetwood, Timothy L Meisenheimer, and John H Scofield. "1/f noise and radiation effects in MOS devices". In: *IEEE Transactions on Electron Devices* 41.11 (1994), pp. 1953–1964.

[143] Enhai Zhao et al. "The effects of radiation on 1/f noise in complementary (npn+ pnp) SiGe HBTs". In: *IEEE transactions on nuclear science* 51.6 (2004), pp. 3243–3249.

[144] Patrick Eckert, Rainer Stamen, and H-C Schultz-Coulon. "Study of the response and photon-counting resolution of silicon photomultipliers using a generic simulation framework". In: *Journal of Instrumentation* 7.08 (2012), P08011.

[145] Lindamulage Malinda Shiram De Silva. "Latest Tests of the CMS HGCAL Tileboard Prototypes". In: *Virtual Spring Meeting of the German Physical Society*. PUBDB-2022-01792. LHC/CMS Experiment. 2022.

[146] K Gill et al. "Radiation damage by neutrons and protons to silicon detectors". In: *Nuclear Instruments and Methods in Physics Research Section A: Accelerators, Spectrometers, Detectors and Associated Equipment* 322.2 (1992), pp. 177–188.

[147] A Chilingarov et al. “Radiation studies and operational projections for silicon in the ATLAS inner detector”. In: *Nuclear Instruments and Methods in Physics Research Section A: Accelerators, Spectrometers, Detectors and Associated Equipment* 360.1-2 (1995), pp. 432–437.

[148] Henning Feick. “Radiation tolerance of silicon particle detectors for high-energy physics experiments”. PhD thesis. DESY, 1997.

[149] Torsten Schulz. “Investigation on the long term behaviour of damage effects and corresponding defects in detector grade silicon after neutron irradiation”. In: (1996).

[150] Anatoly Ronzhin, Marcel Demarteau, Sergey Los, and Erik Ramberg. “Study of timing properties of silicon photomultipliers”. In: *2008 IEEE Nuclear Science Symposium Conference Record*. IEEE. 2008, pp. 2395–2399.

[151] Wei Shen. “Development of high performance readout ASICs for silicon photomultipliers (SiPMs)”. PhD thesis. 2012.

[152] Paola Avella et al. “A study of timing properties of silicon photomultipliers”. In: *Nuclear Instruments and Methods in Physics Research Section A: Accelerators, Spectrometers, Detectors and Associated Equipment* 695 (2012), pp. 257–260.

[153] Stefan Seifert et al. “A comprehensive model to predict the timing resolution of SiPM-based scintillation detectors: theory and experimental validation”. In: *IEEE Transactions on nuclear science* 59.1 (2012), pp. 190–204.

[154] Ruud Vinke et al. “Optimizing the timing resolution of SiPM sensors for use in TOF-PET detectors”. In: *Nuclear Instruments and Methods in Physics Research Section A: Accelerators, Spectrometers, Detectors and Associated Equipment* 610.1 (2009), pp. 188–191.

[155] Paolo W Cattaneo et al. “Development of high precision timing counter based on plastic scintillator with SiPM readout”. In: *IEEE Transactions on Nuclear Science* 61.5 (2014), pp. 2657–2666.

[156] M De Gerone et al. “A high resolution Timing Counter for the MEG II experiment”. In: *Nuclear Instruments and Methods in Physics Research Section A: Accelerators, Spectrometers, Detectors and Associated Equipment* 824 (2016), pp. 92–95.

[157] F Carnesecchi et al. “Experimental study of the time resolution of SiPM coupled to scintillator”. In: *Nuclear Instruments and Methods in Physics Research Section A: Accelerators, Spectrometers, Detectors and Associated Equipment* 982 (2020), p. 164484.

Acknowledgements

First and foremost, I would like to express my profound gratitude to my supervisor, Prof. Dr. Hans-Christian Schultz-Coulon, for providing me with the opportunity to work under his tutelage throughout my thesis. His unwavering support and patience have been invaluable.

I would like to express my sincere gratitude to the Heinz Götze Memorial Fellowship for providing me with financial support during the first three years of my study.

I extend my heartfelt thanks to Prof. Dr. Peter Fischer for graciously agreeing to be my thesis referee.

I am also grateful to Dr. Wei Shen and Dr. Yonathan Munwes for not only guiding me academically, but also for fostering my growth as a team player.

My appreciation goes out to Dr. Rainer Stamen, Dr. Vera Koleva Stankova, Dr. Konrad Briggl, Dr. Yonathan Munwes, Dr. Huangshan Chen, and my wife for their thorough review of my thesis. Their insightful comments and corrections have enhanced the readability of this work.

I would like to express my gratitude to the members of the Mu3e Tile Detector group, as the knowledge I have gained through our collaborations and discussions has been truly enriching.

My sincere thanks also go to all the individuals in the Mu3e collaboration for their invaluable assistance. Special mention goes to Mrs. Hannah Klingenmeyer and Mr. Giovanni Dal Maso for their unwavering support during the PSI radiation beam-test. Additionally, I am grateful to Prof. Dr. Gavin Hesketh and Prof. Niklaus Berger for their invaluable software support for the simulations in this work.

I would like to extend my appreciation to all members of the F8 and F11 group for fostering a pleasant working environment. I am particularly grateful for Dr. Huangshan Chen's support in both professional and personal matters. Also, I would like to express my gratitude to Mrs. Hannah Klingenmeyer for her kindness as a colleague and a friend.

我也要把我最真挚的感谢献给我的家人。

我要感谢我的外公。你在我很小的时候就在我的心灵里种下了自强的种子，给我点亮了求知的星火。真希望你在天堂也能看到这种子发芽，长成参天大树；这星星之火，成燎原之势。

我还要感谢父母。谢谢你们的青春和汗水，为我搭建的避风港让我成年前从未因为经济压力操心；谢谢你们的宽容与理解，让我做出即使你们不理解的决定的时你们也能站在身后支持我；谢谢你们最无条件的支持，让我即使在最黑暗的时候也坚信前方会有光。 儿子定以寸草心，报你们的春晖之恩。

最后，我还要感谢我的爱人。感谢你的温暖陪我走过了最寒冷的日子，感谢你的阳光照亮我跋涉最黑暗的路程。

我也要感谢我自己，没有轻言放弃。路长且艰，你终将成为自己的英雄。